ANNUAL REPORT OF THE DIVISION OF HIGH

TEMPERATURE ENGINEERING

(April 1, 1981-March 31, 1982)

October 1982

Division of High Temperature Engineering

日 本 原 子 力 研 究 所
Japan Atomic Energy Research Institute

Annual Report of the Division of High Temperature Engineering

(April 1, 1981 - March 31, 1982)

Division of High Temperature Engineering,
Tokai Research Establishment, JAERI

Research activities conducted in the Division of High Temperature
Engineering during fiscal 1981 are descrived.

R & D works of our division are mainly related to a multi-purpose
very high-temperature gas-cooled reactor (VHTR) and a fusion reactor.
This report deals with the main results obtained on material test,
development of computer codes, heat transfer, fluid-dynamics, structural
mechanics and the construction of an M + A (Mother and Adapter) section
of a HENDEL (Helium Engineering Demonstration Loop) as well.

高温工学部年報

（ 昭和 56 年 4 月 1 日 ～ 昭和 57 年 3 月 31 日 ）

日本原子力研究所東海研究所高温工学部

　昭和 56 年度における高温工学部における研究活動を述べたものである。

　我が部の研究開発は，主として，多目的高温ガス炉および核融合炉に関係している。本報告書は，主な成果として，材料試験，計算コードの開発，伝熱流動，構造機器等の研究およびヘンデルのマザー・アダプター（M＋A）試験部の建設に関し記載している。

CONTENTS

1. HELIUM ENGINEERING DEMONSTRATION LOOP (HENDEL)

Y. Okamoto, H. Shimomura, T. Tanaka, N. Izawa, S. Nekoya,

Y. Hoshi, H. Hayashi, T. Kunitama, S. Kawaji, T. Kobayashi,

K. Takase, K. Kunitomi, S. Maruyama and Y. Inagaki

1.1 General Description of VHTR and HENDEL

1.1.1 VHTR and its High-Temperature Components

A helium engineering demonstration loop (HENDEL) at JAERI for a very high-temperature reactor (VHTR) is so designed as a large-scale model testing facility for demonstrative operation of high-temperature components, such as an intermediate heat exchanger (IHX), a high-temperature piping, an emergency isolation valve and a core support structure of VHTR, which are supposed to be exposed to extremely severe conditions. Its operation was started in April, 1982, specifically to demonstrate performances and integrities of these components of VHTR from a standpoint of licensing.

Over the past years, the design studies of VHTR have been conducted at JAERI. The conceptual design was completed in 1976, and the more detailed design works and the safety analyses of VHTR are continued. The VHTR is a helium-cooled graphite-moderated reactor supplying a thermal output of 50 MW, and the coolant temperature at the outlet of the reactor is specified as 1000°C. The VHTR must be provided with the features as follows.

(1) Demonstration test for nuclear process heat applications

(2) Irradiation test for development of fuel and material for high-temperature use

(3) Confirmation test for VHTR plant safety

The design parameters of VHTR are determined, considering these functions. The reactor is provided with two primary cooling circuits. Each of them is connected to the secondary cooling circuit through an intermediate heat exchanger. The components for process heat applications, such as a steam reformer, will be placed in one of the two secondary circuits.

Emphasis is placed on providing the outlet coolant temperature as high as possible. The type of fuel block chosen is a prismatic graphite block with a hexagonal cross-section, accommodating a hollow fuel pin sheathed with a graphite sleeve. The core is composed of a regular array of these graphite blocks, piled up vertically.

The reactor and the components for process heat applications may have different characteristics, and therefore analyses must be carried out from a safety standpoint. In this context confirmation tests for the reactor and high-temperature components using HENDEL are planned.

A VHTR core concept is based on TRISO-coated fuel particles, graphite being used for the moderators and reflectors. Fuel assemblies, as shown in Fig. 1.1, are designed as a pin-in-block type fuel using a hollow fuel rod. In this type of fuel, shrinkage and thermal strains in the fuel tubes are relieved at the interface gaps, and stresses in the blocks are relaxed as far as strength is concerned. In the fuel pins itself, high stress arised by interaction between the components as well as by restraint of bowing.

So as to meet the required outlet temperature, the size and core structure are chosen. A 73-column core with 12 fuel pins per block is designed with consideration of the advance of technology in the near future. The maximum fuel temperature is lower than 1350°C. The core power density is 2.2 W/cm^3, and the system pressure and the core pressure drop are 4.0 and 0.06 Mpa respectively. Lower flow rate and higher heat flux might give rise to heat transfer problem which is called flow laminarization.

Figure 1.2 shows an arrangement of a primary system within the steel reactor pressure vessel (RPV). The reactor core is supported by posts and a core support plate is attached to the lower part of RPV. Coolant enters through the outer tube of high-temperature concentric ducts at the bottom of RPV. It flows upward through the space between fixed side-reflector and side-shielding element as well as between a core barrel and RPV to keep the temperature of steel structures, such as the core support structure, the core barrel, RPV and so on, lower than the allowable one. Then it enters a refueling region from the upper plenum through an ajustable orifice valve. An orifice regulates the amount of flow allowed in each refueling region by adjusting the flow area wetted by the coolant in the upper plenum. An orifice device comprises concentric cylinders with rectangular slots.

The orifice is closed when the outer cylinder is moved up and the inner
cylinder remains as it is. After entering the annular spaces between
the fuel pins and blocks within a refueling region, coolant flows down-
ward through the core. Near the bottom of the core the coolant flows
into 7 larger channels. After passing through these 7 channels, coolant
flows into a single channel within a core support block, then ejects to
a lower plenum. In the lower plenum, coolant from 19 refueling regions
and replaceable side-reflector blocks, mixes and enters the inner tube
of the high-temperature concentric ducts.

In the regular refueling region, a central column with two control-
rod channels and two reserved shutdown-holes is surrounded by fuel-
columns; in a peripheral refueling region, a control-column is surrounded
by only 1 or 3 fuel-columns with remaining reflector-columns. The top-
and bottom-reflectors are each 114 mm thick, and the side-reflector
110 mm. The whole core is held together by a series of lateral restraint
mechanisms tightened from the periphery to the core, and it stands on
a diagrid over which a multi-layered steel plate is placed.

The core structure is required to keep the coolant channel and
whole core sound as well as to maintain the core shutdown mechanism
to be operated in any circumstances. Thus seal and thermal insulation
characteristics of the core structure become of prime importance.
In addition, the design of the core is made in such a way that the amount
of shrinkage in an active core is as small as possible and the side-
reflector plays like an unmovalble solid blocks due to its "arch" con-
figuration and to the elastic lateral restraints as well.
If this shrinkage is beyond a certain limit, the blocks become loose
and lateral displacements could occur. The block columns exposed to
irradiation are less stable, because they permit bowing caused by
transverse flux gradients. If the columns stand free, the bowing would
be the maximum, when all the gaps which are formed at the block ends
completely closed. The inter-column clearances, however, are too small
to allow all the columns to have the maximum displacements, and this
may cause the unstableness. This would also give rise to the occurrence
of induced bypass- and cross-flows.

The coolant leaves the core at an average temperature of 1000°C
and then enters an intermediate heat exchanger. In the concentric hot
gas ducts between the core and IHX, high-temperature helium gas flows
inside of the inner tube. To avoid large heat loss from the inner tube

to the cold gas of the outer tube and at the same time to reduce the temperature of the inner pressure tube, this pressure tube carries thermal insulation on the inner surface. The thermal insulation consists of multi-layered fibre mats with metal foils in-between.

The IHX consists of a pressure vessel with two concentric outlets for primary and secondary helium gas. In the pressure vessel an inner container is placed. This inner container houses a helical tube bundle with a center pipe with inner thermal insulation. One end of the tubes is welded to a plate, and the other side to the conical end of the center pipe. The inner container and the pressure vessel form an annular space. The primary helium gas enters the pressure vessel at the bottom and flows upward inside of the center pipe. The secondary helium gas flows in the vessel through the annular space of the concentric duct at the top of IHX. It flows downwards through the annular space between the inner container and the pressure vessel. At the bottom of the inner container the helium gas enters the inner container and flows upward around the tube bundle. At the top of inner container the secondary helium gas is discharged into the inner pipe of the concentric duct.

After passing through IHX, the coolant enters the suction of circulators. Then circulators force the coolant to flow between the outer and the inner tubes of the hot gas ducts until it again mixes in RPV.

1.1.2 HENDEL and its Objectives

Figure 1.3 shows a schematic flow diagram of VHTR and HENDEL test sections. High-temperature key components are: (1) fuel stack and control rods, (2) support structure exposed to the direct impingement of core outlet flow, (3) reactor internal components and structure necessary to establish structural, thermal and fluid flow parameters, and (4) high-temperature components of heat removal system.

The HENDEL test sections are expected to be parts of VHTR R & D program, which include the design and analysis of the reactor core and plant components, as well as tests using component test facilities, such as a large scale high-temperature helium gas loop (HTGL) for flow and heat transfer studies.

Test conditions of HENDEL test sections should be determined so as to permit the evalustion in actual VHTR conditions. Final selection of test conditions is made as shown in Tables 1.1 and 1.2.

The loop consists of Mother section, Adapter section and Test sections. A schematic flow diagram of HENDEL is shown in Fig. 1.4. Mother loop section circulates helium gas of the specified flow rate (0.4 and 4.0 kg/s), pressure (40 kg/cm² G) and purity. It consists of helium circulators, heaters, coolers, mixing tanks and filters, connected with helium purification, helium storage and cooling water systems which are designed for the respective purposes of purification, storage and cooling of primary helium gas. Adapter section heats helium gas up to 1000°C, and consists of high temperature heaters and coolers. Test sections consist of 4 sections, the test items of which are:

(1) Fuel stack test section (T_1)

    1. Heat transfer and fluid-dynamics at power transient condition

    2. Heat transfer and fluid-dynamics at partial load

    3. Effects of lateral power distribution

    4. Integrity of graphite fuel block

    5. Operation test of control rod

(2) In-core structural test section (T_2)

    1. Seal performance at high-temperature area of core

    2. Performance at high integrity of the thermal insulation structure

    3. Mixing behavior at high-temperature plenum

    4. Integrity of core support structure (Graphite post, diagrid and so on)

    5. Integrity of high-temperature outlet tube

(3) In-core flow test section (T_3)

    1. Core flow distribution

    2. Integrity of core lateral restraint structure

    3. Building of in-reactor structural assemblies

    4. In-service inspection technology of reactor vessel

    5. Functional test of stop valve

(4) Heat removal test section (T_4)

    1. Intermediate heat exchanger

    2. Steam generator

    3. Integrity of emergency isolation valve

    4. Piping

    5. Preformance of the heat transfer system at partial load and power transient condition

    6. ISI technology

1.1.2.1 Mother-Adapter Section (M+A)

Helium gas in the loop is circulated by a combination of hermetically sealed, vertical single stage, centrifugal, gas-bearing blowers driven by two-pole synchronous motors. The blower for No.1 mother loop (M_1) is called B_1, and that for No.2 mother loop (M_2) B_2. The blower output is varied by regulating the rotor speed from 3000 to 12000 rpm. Speed of the blower rotor is controlled through the solid-state, high-frequency power supply unit (12 steps inverters) which varies the frequency from 50 to 200 Hz. Water cooling of the blower prevents overheating at the inlet temperature up to 400°C maximum. The blower characteristics are illustrated in Fig. 1.5. These curves can be used to predict the amount of pressure drop available at any flow and blower speed.

The test section requires heaters capable of operating at 4.0 MPa, providing 0.16 MW, 2.0 MW and 9.1 MW heat to helium gas with respective outlet temperatures of 400, 400 and 1000°C. The heater for M_1 loop is called H_1, for M_2 loop H_2, and for Adapter section H_3. Adapter section provides two heaters (H_{31} and H_{32}) in which helium gas passes through tubular heating elements. Main specifications of heaters are given in Table 1.3, and an arrangement of H_{32} is shown in Fig. 1.6.

The loop requires four heat exchangers (coolers: C_1, C_2, C_{31} and C_{32}) so as to lower the helium gas temperature to an acceptable level for the blower. The heat discharged by the coolers should be held to be the minimum, using the cooler bypass valve. Heat transfer and flow studies relating to coolers have been made along with structural analysis taking into consideration the ASME Code Sec. VIII Div. 2 and Case 1592. Main specifications of coolers are compared in Table 1.4. An arrangement of C_{31} is given in Fig. 1.7.

1.1.2.2 Thermal and Hydraulic Performance of HENDEL

Operation modes of HENDEL are shown in Fig. 1.8. A layout of HENDEL is depicted in Fig. 1.9, which shows the capability of testing large components at actual operational conditions before being used in VHTR. In the course of tests using HENDEL a large amount of thecnical problems which are bound to the design of a prototype reactor, especially for high-temperature use, are expected to be solved.

1.2 Present Status of HENDEL

Present status of a schedule for design, construction and test of HENDEL is shown in Fig. 1.10. The operation of M+A section was already started in April, 1982, and that of test section will be started in 1982-83 for the licensing of VHTR and improvement of design itself.

1.2.1 Mather-Adapter Section (M+A)

As mentioned in the previous section 1.1.2.1, Mather-Adapter section consists of 8 parts such as M_1 loop, M_2 loop, adapter section, make-up system (Mu), purification system (Mp), instrumentation and control system (In), utility cooling system (Uc) and electrical system (El). The design work of this section was completed in early 1980, and the construction work in August, 1981.

Since the completion of installment of M+A section, preliminary tests have been performed. Technical problems encountered during the test will be described later.

The M+A section is provided with gas circulators, electric heaters, water coolers, pipes and valves, to supply helium gas of the specified temperature, pressure and flow rate to each test section. During the course of design and fabrication, bilateral test has clarified a couple of problems as described below.

(1) As for the material of heater element in helium gas, tantalum was often chosen, but it was easily attacked to change into Ta_2O_5, etc. in an oxygenated atomosphere, and Ta_2C, etc. in a carbonated atomosphere, becoming brittle. Therefore, impurity concentration in helium gas must be kept below 0.1 ppm in O_2 and below 10 ppm in H_2O and CO, and it was not recommended for a long-time use. Various heat-resisting alloies were tested, but no better material except trantalum could be found. Comparisons of the specifications of heater elements are shown in Table 1.5, a configuration of the heater element H_{32} in Fig. 1.11.

As for the graphite heater elements, welding test was made for 30 hours in 1000°C helium gas environment, and was obtained the following results.

1) As for temperature measurement, it might be better that boron-nitride mount is screwed into graphite and temperature is measured with Inconel-600 sheath P-R thermocouples at the inlet

and W—Re or Pr—Pr thermocouples at the outlet.

    2) If the amount of binder in boron-nitride exceeds, green glass
       is deposited and adhesion of tube sheet will occur at the screw.

    3) Lead-bar connection by molybdenum screw was found to be safe
       for protection from local melting by abnormal heating.

    4) In some parts of the surface of graphite heater elements and of
       the lead-bar oxidation and burning-off were recoginized, and in
       some other parts fine graphite particles were deposited.

(2) In order to absorb thermal expansion of the connecting pipes between
the test section and the cooler C_{31}, bellows of Incolloy 800H are
fixed in the horizontal and vertical parts. Inner pipes are set
inside the bellows and insulator is placed in-between.

(3) With the advance of design and fabrication, some modifications
have been made. Table 1.6 indicates modified items of main spec-
ifications.

(4) As the test section T_1 was determined to be installed in the buil-
ding of M+A section, the place of settling M_1 loop was changed to
the east side of the building.

(5) Tests of a helium supplying system was supposed to be carried out
according to the rules and standards of the high pressure gas
regulatory laws, and those of water supplying system according to
the boiler and pressure vessel safety rule. But, as HENDEL is
such an high temperature and high pressure facility never made
before (gas inventory is about 2000 NM^3), some inspection items
are added as shown in Table 1.7.

    The components of M+A loop have been fabricated since April, 1980.
The inspections of helium and nitrogen gas vessels, compressors, pipes
and valves have been made satisfactorily. As for the inspection of the
equipments of electricity and instrumentation, the standards of JEC and
JEM were applied to each simple unit excluding instrumentation. The
instrumentation and control system consists of dispersive instrumentation
system, centralized observation control system, backup system, safety
defense system and others. Detailed examination of the function of each
system was already finished, and various improvements of software and
hardware, as listed in Table 1.8, have been made.

    A type of gas circulator adopted in HENDEL loop is a vertical
centrifugal gas-bearing type made by the Alsthom-Atlantique D.M.E.
(Rateau, France). The revolution speed is controled by frequency change

of three-phase alternating current, and by flow rate, making use of bypass valves. A cross-sectional view of the gas circulator is shown in Fig. 1.12, and items of test and inspection are shown in Table 1.9. During a dynamic balance test, a shaft was deformed by heat and defects of a conductor rod as well. This inevitably caused a several months delay in schedule.

1.2.2 Fuel Stack Test Section (T_1)

The aim of the experiments using T_1 test section is to evaluate heat transfer and flow characteristics of the fuel element under the same condition of VHTR. T_1 test section consists of a single-channel test rig (T_{1-S}), and a multi-channel (12 channels, one column) test rig (T_{1-M}). Figures 1.13 and 1.14 show general views of T_{1-S} and T_{1-M} respectively.

JAERI already made a contract of T_1 test section with the Fuji Electric Co., and the design of the test rig and of the components are now in progress. The research items and test conditions of T_1 test section are:

(1) T_1 test items

Table 1.10 shows T_1 research items, and Table 1.11 T_1 test conditions. These conditions are the same as those of VHTR, but there are many difficulties such as;

a) Measuring techniques under high temperature and pressure

b) Fabrication of high-temperature fuel pin simulator

Heat transfer and flow tests under two different conditions are planned. One is a high-temperature test and the other is a middle-temperature test.

(2) T_1 test conditions

1) High-temperature test

Flow rate range is 20-200% of the average flow rate of VHTR. The minimum flow rate is chosen so as to study heat transfer and flow characteristics in the range of large heat flux parameter (q^+), and the maximum flow rate is neccessarily determined by the limitation of the capacity of the gas circulator. The average flow rate of VHTR is 17.2 g/s per channel.

2) Middle-temperature test

The conditions of middle-temperature test and VHTR are:

a) Heat flux parameter (q^+) is the same as that of VHTR.

b) Inlet Reynolds number is the same as that of VHTR.

Helium gas temperature at the outlet should be lower than the temperature limitation of a probe. Therefore, temperatures of 270°C at the inlet and 750°C at the outlet were chosen for the middle-temperature test.

3) Other tests

Fuel pin vibration test and control rod flow test will be carried out with the single-channle test rig under the same pressure and flow rate of VHTR. Coolant temperature should be determinded with consideration of the temperature limit of sensors.

(3) T_1 test components

T_1 test components include a mock-up fuel pin, a control rod, upper and lower replaceable blocks, fuel blocks, compensation heaters and sensors. As the instrumentation in high-temperature is unreliable, a middle-temperature test of single-channel on heat transfer and flow is planned in order to accumulate more reliable data. The main objective of this research is to evaluate the effect of heat transfer distribution on the heat transfer and flow characteristics, and three types of heat flux distribution are now considered as the test conditions.

(4) Data processing system

Data processing system includes an on-line calculator (YHP-1000), a data sensors, a fast Fourier-analizer and hot-wire anemometer, and these are all connected with GP-IB. The data obtained from the sensors are recorded on magnetic tapes, ready to be transmitted to an on-line calculator whenever it will be suited.

(5) Specification of mock-up fuel pin

The mock-up fuel pin is so planned to be fabricated as follows.

a) Maximum power per channel is larger than heat generation rate

of VHTR fuel pin (59.3 kW average)

b) Variable axial heat flux distribution

c) Same material as is used in VHTR

d) Maximum surface temperature is larger than 1200°C

(6) Temperature measurement

Thermocouples for measuring the temperature of helium gas and fuel pin surface are required high accuracy and reliability even in a carburizing environment. From this viewpoint, R & D on thermocouples has been carried out, and the results are shown in Table 1.12.

1.2.3 In-Core Structure Test Section (T_2) and In-Core Flow Test Section (T_3)

1.2.3.1 T_2 Test Section

The performance and soundness of sealing, insulator and gas flow in the core are to be examined. Figure 1.13 shows T_2 test section that simulates a part of the lower plenum structure, consisting of plenum blocks, core support posts, insulator layer, core support plate, high-temperature outlet ducts, etc. In the test section 400°C helium gas supplied from M_2 loop flows through the outer tube of lower duct to cool diagrids, core support plates, core barrels, and core-binding mechanism and finally flows out through the outer tube of the upper duct to M_2 loop. On the other hand, helium gas heated up to 900°C in M_2+A loop, and flows through the inner tube of the upper duct to a flow-rate adjuster, a heater and the lower plenum structure which forms seven regions of the core, returns to Adapter section through a lower duct. Figure 1.14 shows a flow-sheet of T_2 section. T_2 section has two main paths, one is to cool steel structure and the other is to supply helium gas to T_2 test section. The flowpath from blowers are M_2+A loop, and the pressure difference between the two paths are controlled from 0.1 kg/cm^2 to 0.3 kg/cm^2. Flow and temperature distribution are chosen the same as those of VHTR by adjusting the flow rate and heat input. The total flow rate in T_2 test section is about one-fourth as much as that of VHTR.

1.2.3.2 T_3 Test Section

T_3 test section simulates complicated flow conditions such as bypass and cross-flows established between graphite blocks in VHTR core. With this test section, the followings are to be examined;

   1) Flow distribution in the core

   2) Characteristics of the orifice

   3) Soundness of the core-binding mechanism

   4) Assembling and disassembling of in-core structure.

1.2.3.3 Simulation of VHTR Condition

Complete simulation of the temperature distribution in the fixed side-reflector is hardly to be acomplished. An in-core cooling condition

which has a close relation to sealing efficiency is not the same as that of VHTR. Namely, the outer diameter of the test section is almost 70%, the total flow rate is 25% and sealing length is 50%, as compared with those of actual VHTR. And if the sealing characterisitcs of the test section and VHTR are equal, leak rate is mostly affected by the lower temperature in the structure and is nearly 17%. Therefore, when the pressure difference in the test section is 0.1 kg/cm^2 which is a half of VHTR, both test section and VHTR are almost equal in leak rate. In order to control the pressure difference in the test section, it is required that the pressure fluctuation in M$_2$+A loop should be lowered enough.

1.2.4 T$_4$ Test Section

The objective of this test is to demonstrate the performance of the primary and secondary heat removal systems, such as an intermediate heat exchanger, a steam generator, a high temperature shut-off valve, a hot gas duct, etc. A flow diagram of T$_4$ test section is shown in Fig. 1.15. Helium gas (1000°C, 2.8 kg/s) is supplied to T$_4$ test section from M$_2$+A loop. Operating conditions are shown in Table 1.13.

The test section is a 1/3-scale model of VHTR, flow rate and temperature being the same as those of VHTR.

The main components of T$_4$ test section, such as a heat exchanger and a steam generator, etc. are also designed as 1/3-scale models.

1.2.5 Core-Restraint Mechanism

A core-restraint mechanism of VHTR is installed between the core barrel and the fixed side-reflectors.

Particularly because the data of relaxation properties are less available, much effort has been concentrated on the study of relaxation, using a 1/2-scale core model and a test specimen of the same material.

The experimental apparatus includes a loading machine, a heater and a displacement meter.

The test on tension, compression, creep, and relaxation are conducted with a loading machine. The maximum load available is 10 ton and tension speed is varied from 0.05 mm/min to 500 mm/min.

The experiment was performed in air, and the temperature was controled within a range of 0°C-600°C.

Displacement can be measured with a displacement meter in a range of 5μm to 5 mm.

The experiment on the relaxation of 2-1/4 Cr-Mo specimens has been performed at 500°C and 450°C for 150 hours.

The results are shown in Fig. 1.16. The stress decreases from the initial stress 22.0 kg/mm^2 to 10 kg/mm^2 at 500°C for about 150 hours, and from the initial stress 23 kg/mm^2 to 17 kg/mm^2 at 450°C for about 150 hours. This stress relaxation is seemingly caused by the primary creep.

1.2.6 High-Temperature Piping

The M+A loop has two high temperature piping. One is located between H_{31} and H_{32}, the other is located between H_{32} and C_{31}, the operating temperature being 1000°C. The main test items are devided into three as follows.

(1) Insulation performance

Confirmation items

  a) Surface temperature of the pressure tube is lower than 350°C in normal operating condition.

  b) Insulation performance will be disturbed by natural convection and deterioration of thermal conductivity of insulation.

(2) Integrity of the insulation support structure

Confirmation items

  a) Temperature of the end pieces and surface temperature of the pressure tube with studs.

  b) Thermal reaction force to the liner

(3) Integrity of the pressure tube

Confirmation items

  a) Hot spot caused by resiliency defect

In parallel with the experiment, thermal analysis of the high-temperature piping in normal operating condition has been carried out. Insulation support structure including pressure tube is chosen as an analytical model. A computer code used deals a two-dimensional F.E.M. calculation. The boundary conditions are:

at the inner surface of the liner;

  Temperature   : 1000°C

  Pressure   : 40 kg/cm^{2}G

Flow rate   :   2.8 kg/s

Heat transfer coefficient :   466 kcal/m^{2}hr°C

at the outer surface of the pressure tube;

Temperature   :   30°C

Pressure   :   atomosphere

Heat transfer coefficient :   13 kcal/m^{2}hr°C

(considering natural convection and thermal radiation

coefficient)

Temperature distributions in the horizontal and vertical cross-section of the high pressure piping are shown in Figs. 1.11 and 1.12.

Hot spot temperature is 14°C higher than the average axial temperature 290°C, and 49°C higher than the average circumferencial temperature 347°C.

1.2.7 The Other Related Items

The construction of the building of M+A loop was started in September, 1979, and was completed at the end of December, 1980. Then the settling of M+A components was begun in January, 1981.

The additional building for the test sections has been constructed since April 1981, and was completed at the end of July, 1982. And the setting of the T_1 test section was begun in August.

①	Standard graphite block
②	Standard fuel rod
③	Dowei
④	Fuel handling
⑤	Sleeve
⑥	Compact
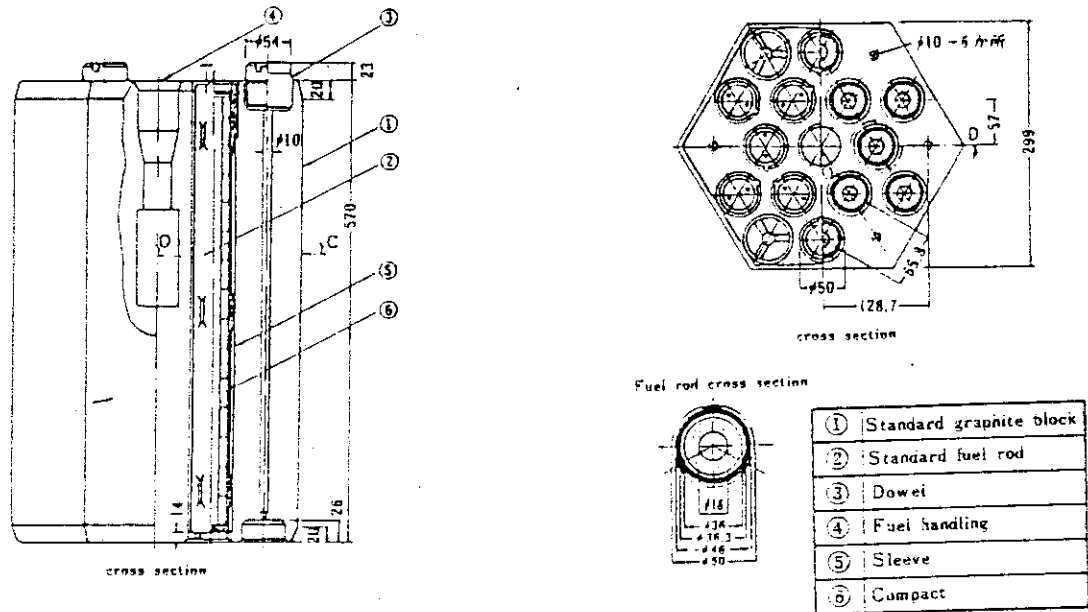
Fig. 1.1   Standard Fuel Element of VHTR

Fig. 1.2   Reactor Arrangement of VHTR

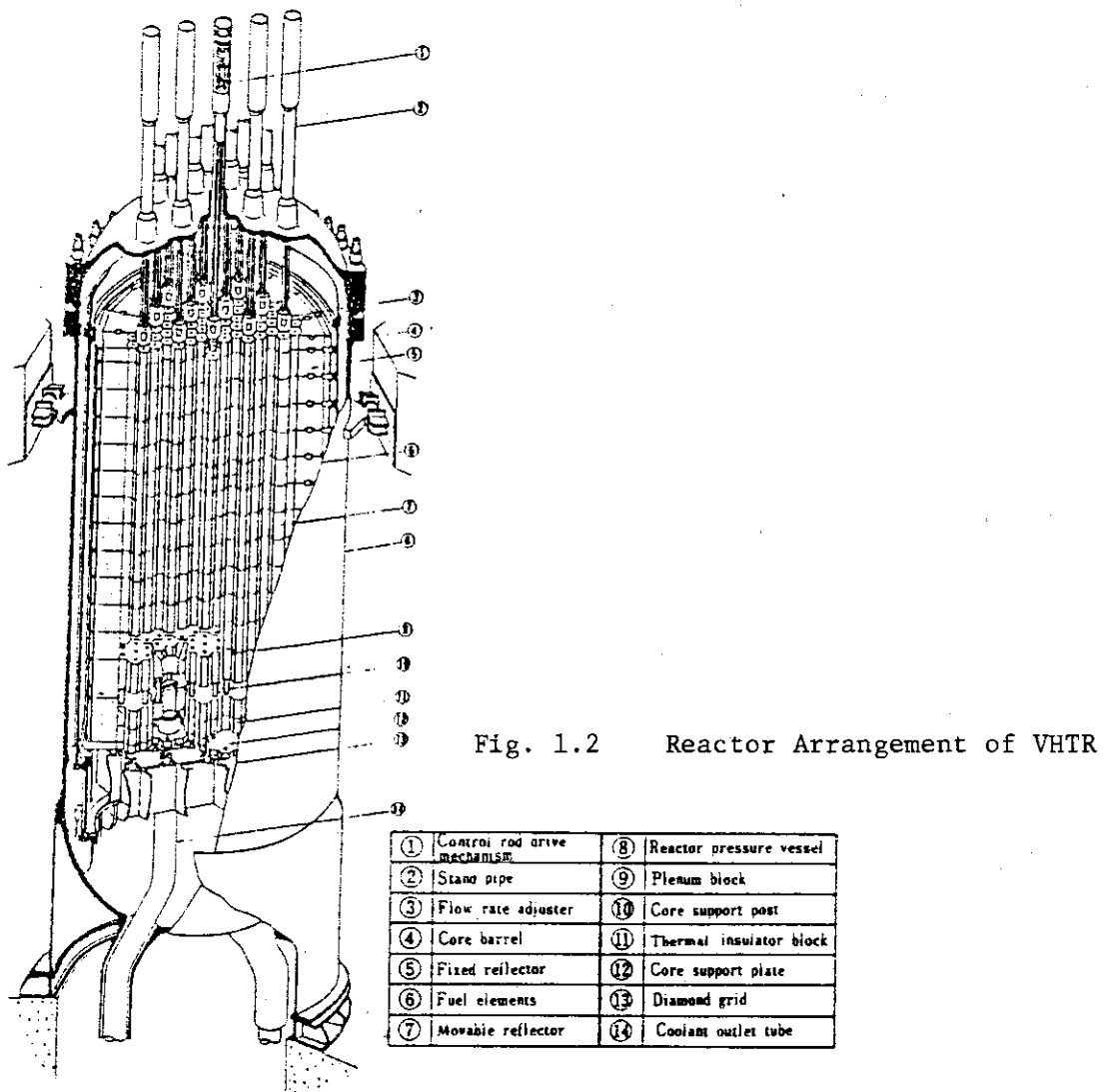|			
①	Control rod drive mechanism	⑧	Reactor pressure vessel
②	Stand pipe	⑨	Plenum block
③	Flow rate adjuster	⑩	Core support post
④	Core barrel	⑪	Thermal insulator block
⑤	Fixed reflector	⑫	Core support plate
⑥	Fuel elements	⑬	Diamond grid
⑦	Movable reflector	⑭	Coolant outlet tube
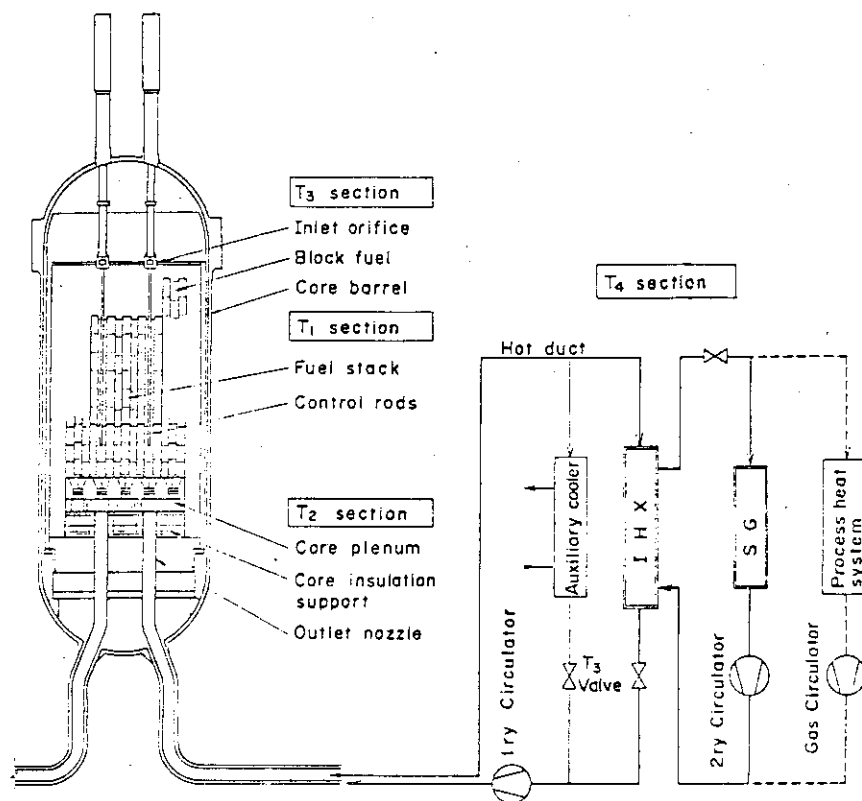
Fig. 1.3   Schematic Flow Diagram of VHTR and HENDEL Test Sections

Table 1.1   Test Conditions of HENDEL Test Sections

Items	Fuel stack test section (T_1)	In-core structure test section (T_2)	Core flow test section (T_3)	Heat removal test section (T_4)
Temperature (°C)	400 — 1000 (max 1200)	1000 (max 1200)	~ 400	~ 1000
Flow rate (kg/sec)	0.4	2.8 (4.0)	4	2.8 (4.0)
Pressure (kg/cm²)	40	40	40	40
Testing components	Fuel stack Control rods	Core bottom plenum Insulator support Outlet duct nozzle	Inlet orifice Fuel block Core barrel Main valve	Hot duct H.T shut off valve I H X S G

Table 1.2   Test Capability of HENDEL in Comparison with VHTR
Basic Parameters

		VHTRex	HENDEL
Temperature		400°C／1000°C	400°C／1000°C
Pressure		40 Kg/cm^{2}G	40 Kg/cm^{2}G
Flow rate	Total flow rate : 16 Kg/sec		M_2: 4+4 Kg/sec
	Loop flow rate : 8 Kg/sec		
	Column flow rate : 210 g/sec (avg.)		M_1: 400 g/sec
	Channel flow rate : 18 g/sec (avg.)		
Thermal power Heat removal capacity	Total power : 50 MW		M_2 ·A : ~11 MW
	Loop power : 25 MW		
Purification system	Flow rate : ~160 g/sec		Flow rate : 100g/sec
Hot duct	Liner tube diam. : ~36 cm		Liner tube diam. : 36cm

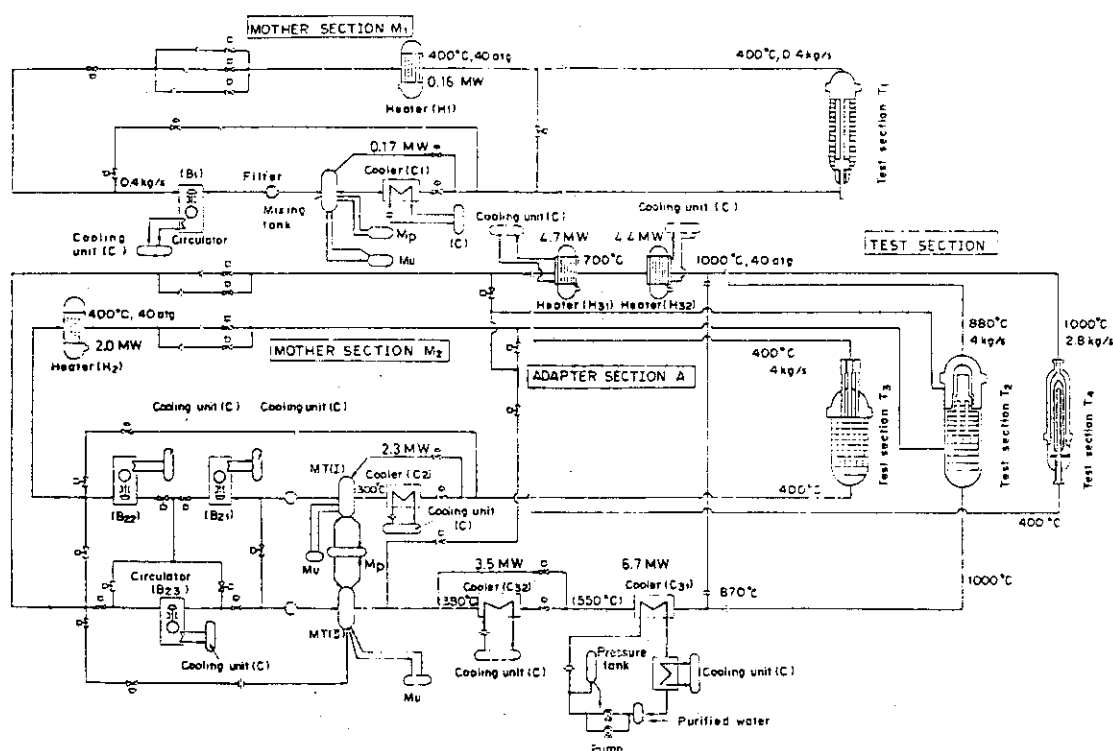
Fig. 1.4   Schematic Flow Diagram of HENDEL
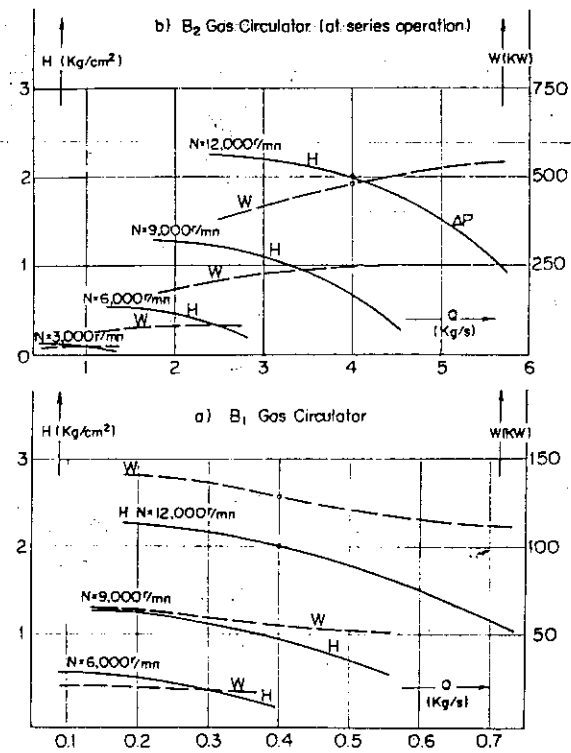
Fig. 1.5   Characteristics of Gas Circulator

$$\begin{bmatrix} 700°C \longrightarrow 1000°C \\ 4.1\,MPa \\ 250\,Kw \sim 4360\,Kw \end{bmatrix}$$

Insulator

⇨ He Outlet (1000 °C)

Heater Element (Gr)

Tie rod

Water Jacket

Insulator

Cylinder

Terminal Element

⇦ He Inlet (700 °C)
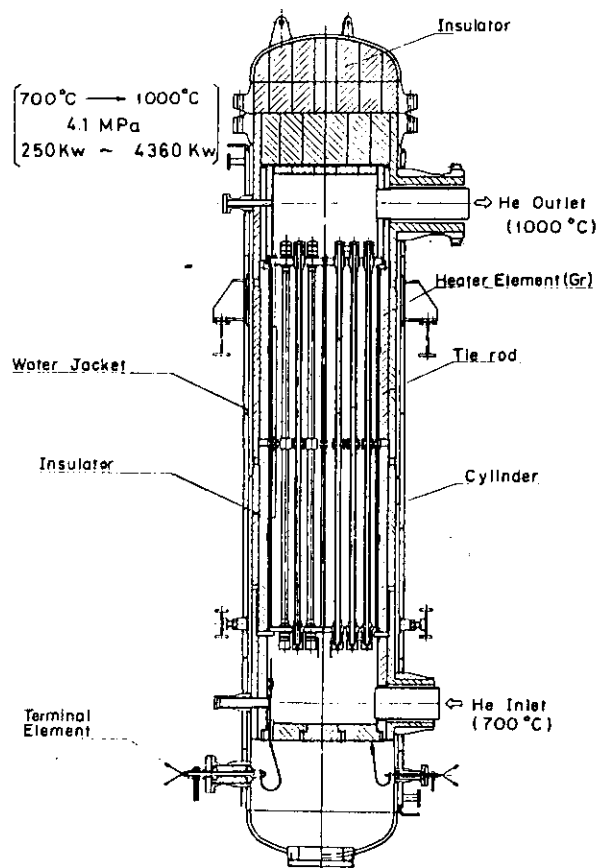
Fig. 1.6 H_{32} Arrangement

Table 1.3 Comparison of Heater Specifications

	H_1	H_2	H_{31}	H_{32}
Heater Type	Resistively heated tubular elements			
Flow Rate (kg/s)	0.4	4.0	2.8	2.8
Power to Gas (MW)	0.160	2.0	4.7	4.4
Inlet Temp. (°C)	323	304	397	700
Outlet Temp. (°C)	400	400	720	1000
Heater Tubes				
Materials	Incoloy 800H	Incoloy 800H	Incoloy 800H	Tantalum
Dimensions (mm)	$2.54^{OD} \times 3.5^{t}$ -2000^{l}	$28.1^{OD} \times 2^{t}$ -3000^{l}	$60.3^{OD} \times 8^{t}$ -5200^{l}	$30^{OD} \times 1t$ -3200^{l}
Total Numbers	18	72	54	72
Numbers in Series or Parallel	6	12	9	4
Electrical Input				
Nominal Current (A)	1022	1500	4630	7560
Nominal Voltage (V)	113	480	366	55.4

Table 1.4 Comparison of Cooler Specifications

	C_1	C_2	C_{31}	C_{32}
Cooler Type	Counterflow-Tube-In-Shell	Counterflow-Tube-In-Shell	Crossflow-Tube-In-Shell (Step-up — Baffled)	Counterflow-Tube-In-Shell
Fluid Stream	Helium/Water	Helium/Water	Helium/Pressur-ized Water	Helium/Water
Flow Rate (kg/s)	0.4/40.69	4.0/55.55	4.0/26.67	4.0/82.86
Inlet Temperature (°C)	395/32	400/32	873/50	550/32
Outlet Temperature (°C)	313/42	288/42	550/110	383/42
Inlet Pressure (MPa)	4.0/0.4	4.0/0.4	4.0/3.6	4.0/0.4
Pressure Loss (kg/cm^2)	0.025/0.085	0.15/0.029	0.0533/0.0218	0.006/0.219
Heat Transfer Rate (Kcal/hr)	1.465×10^5	2.0×10^6	5.77×10^6	2.983×10^6
Counterflow LMTD (°C)	315.6	304.1	622.3	424.7
Thermal Conductance UA (Kcal/m^2·hr·°C)	386.3	308.8	502.2	418.1

$$\left[\begin{array}{c} 1000°C \rightarrow 550°C \\ 4 MPa \\ 6300 Kw \end{array}\right]$$

Fig. 1.7 C_{31} Arrangement

a) M_1 Loop

b) M_2 Loop

c) M_2 + A Loop

d) M_2 + A Loop
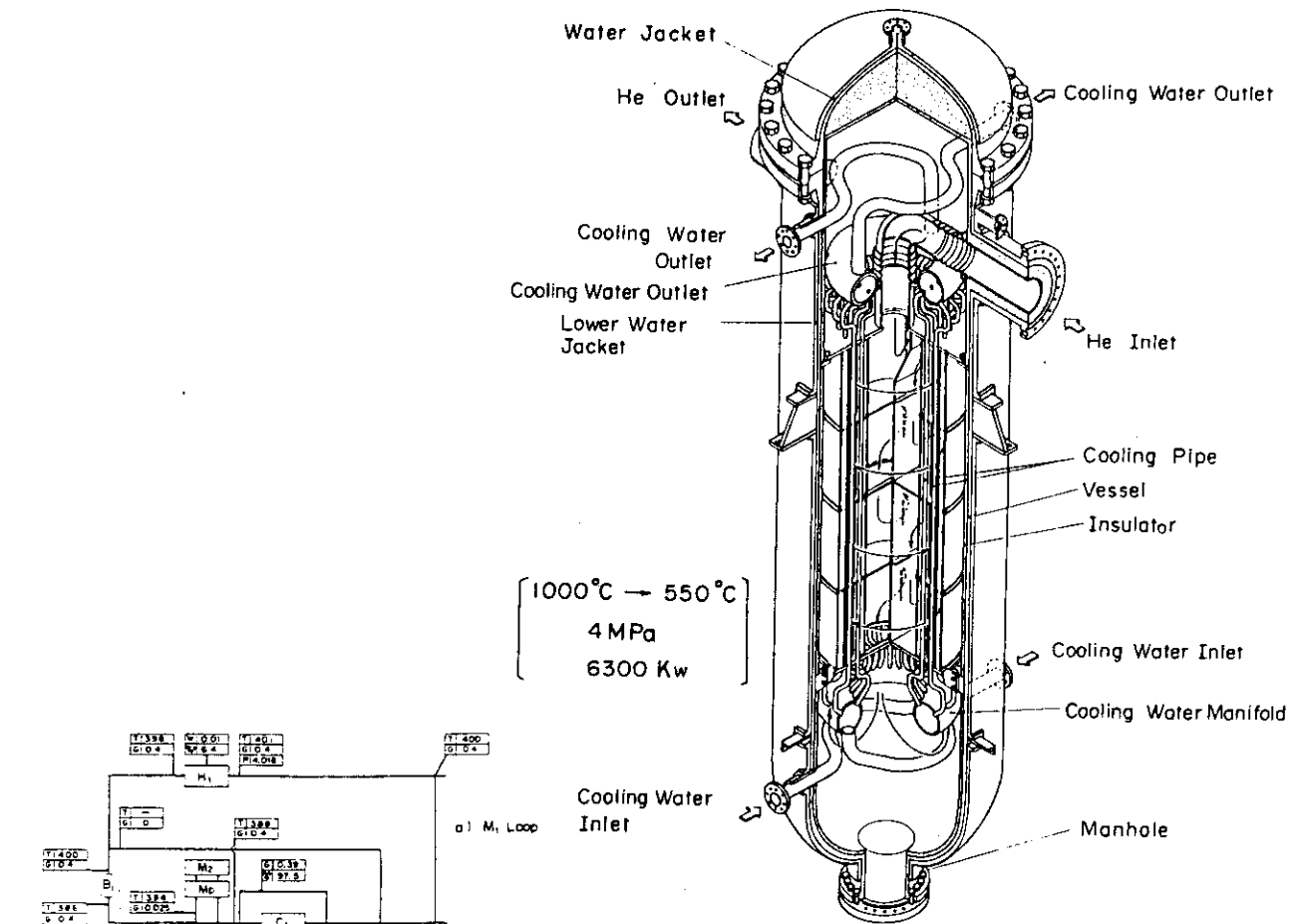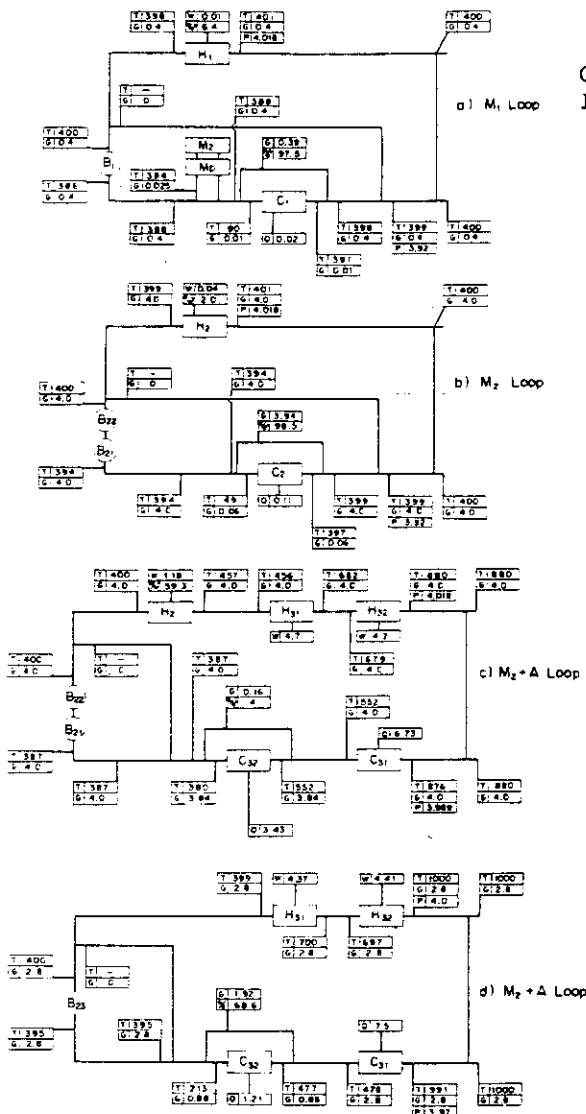
T   helium temperature(C)

G   helium flow rate(Kg/s)

W   heater power(MW)

Q   cooler heat transfer rate(MW)

G/G^*, W/W^* ratio to nominal value

Fig. 1.8   Operating Mode for HENDEL

Fig. 1.9   Layout of HENDEL

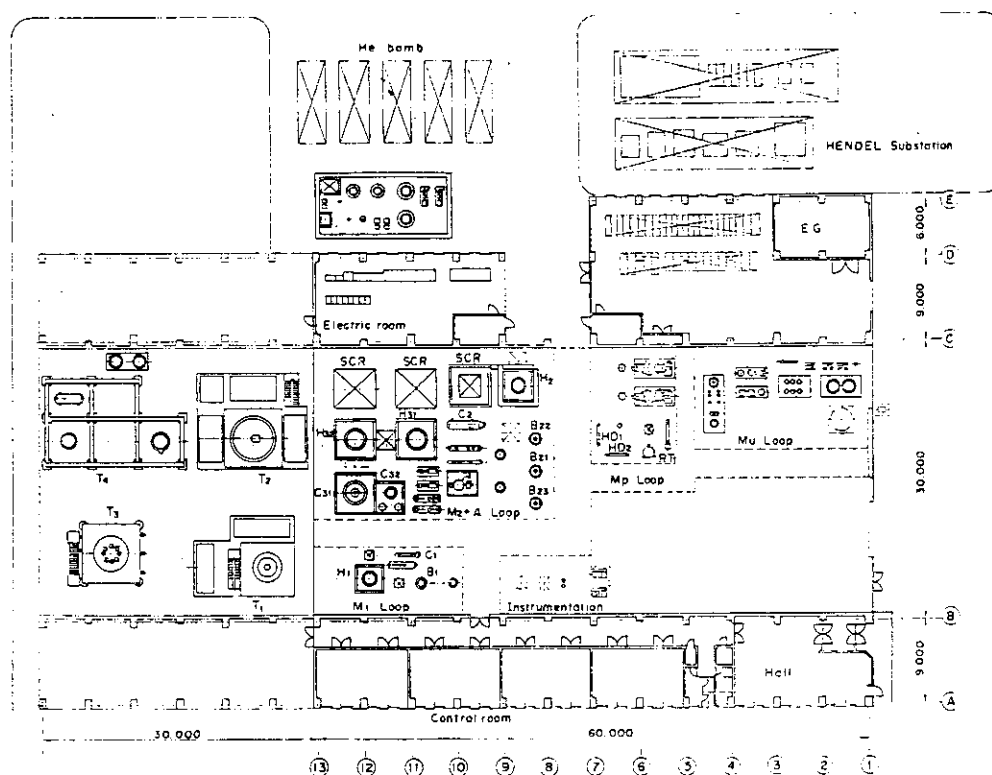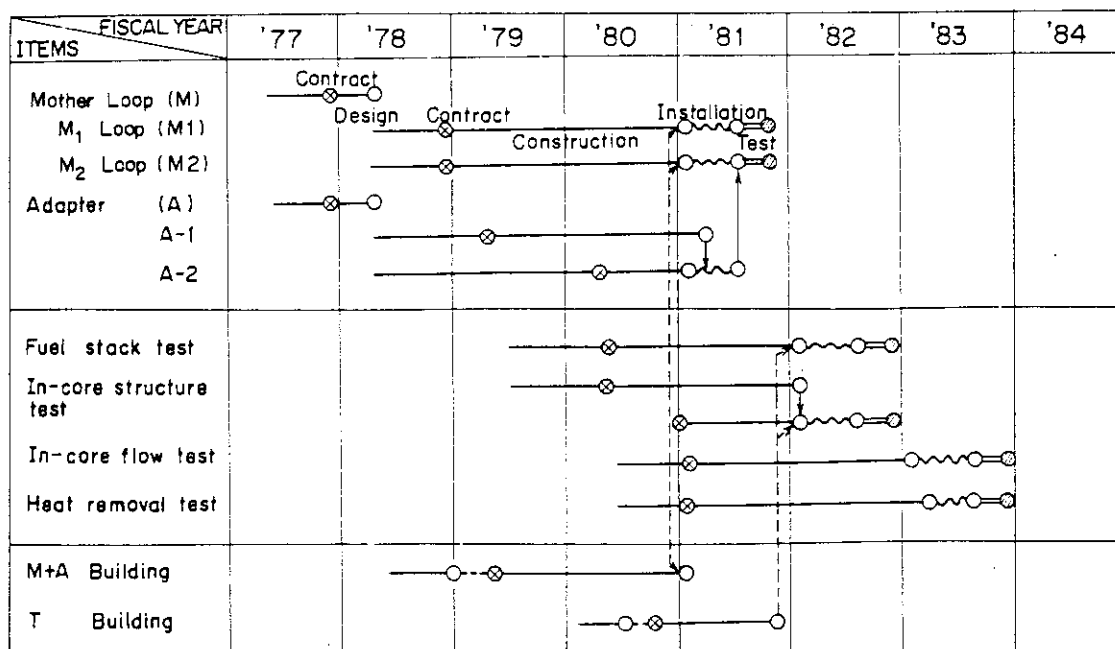| FISCAL YEAR ITEMS	'77	'78	'79	'80	'81	'82	'83	'84
Mother Loop (M)	Contract							
M₁ Loop (M1)		Design	Contract	Construction	Installation			
M₂ Loop (M2)					Test			
Adapter (A)								
A-1								
A-2								
Fuel stack test								
In-core structure test								
In-core flow test								
Heat removal test								
M+A Building								
T Building								

Fig. 1.10   Schedule for Design, Construction and Test of HENDEL

Table 1.5 Main Specifications of Different Heater Elements

| Item	HTGL (Tantalum heater elements)	H_{32} (Tantalum heater elements)	H_{32} (Graphite heater elements)
Type	Directly welding pipe heater	Directly welding pipe heater	Directly welding pipe heater
Fluid	Helium gas	Helium gas	Helium gas
Flow rate	100 g/sec	2.8 kg/sec	2.8 kg/sec
Design pressure	43 kg/cm^{2}G	45 kg/cm^{2}G	45 kg/cm^{2}G
Design Temperature	Inlet/outlet 715°C/1000°C	Inlet/outlet 715°C/1000°C	Inlet/outlet 715°C/1000°C
Material pressure vessel	SUS 27	SB 42	SB 42
Nozzle	Hastelloy X	SF 45+Hastelloy X SF 45+Incoloy 800	SF 45+Hastelloy X SF 45+Incoloy 800
Element	Ta seamless	Ta or Nb-1%Zr seamless	Graphite
Input power	70 270 kW	7000 KVA (heat transfer 250 4360 kW)	7000 KVA (heat transfer 250 4360 KW)
Element dimension	U-tube	Straight tube	Straigth tube
Disign Temperature	1300°C	1250°C	1240°C (1290°C)
Stress deadweight	0.12 kg/mm^2	0.24 kg/mm^2	0.24 kg/mm^2
Electromagnet	0.09 "	0.34 "	0.43 "
Impurity concentration	O_2, N_2 1 ppm	O_2, N_2, CO_2, CO, H_2O 0.1 ppm	H_2, N_2, CO_2, CO, H_2O 0.1 ppm
(outlet of M_p)		H_e, CH_4, C_mH_m 0.2ppm	H_2, CH_4, C_mH_m 0.2ppm
Purification flow rate	40 Nm^3/hr	100 y/sec	100 g/sec
Design longevity	1000 hr	2×10^4 hr	2×10^4 hr
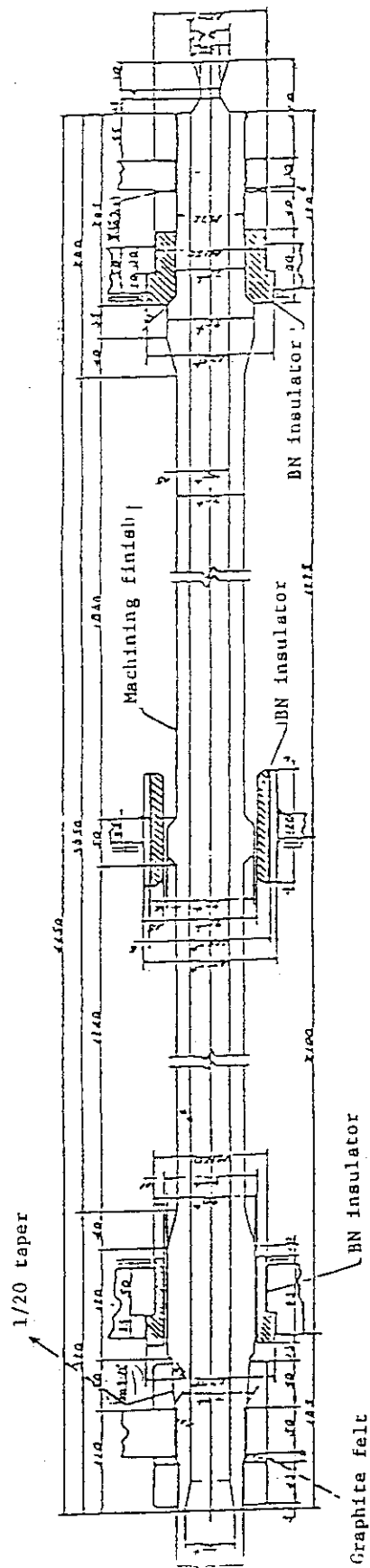
Fig. 1.11 H$_{32}$ Heater Element

Table 1.6   Modified Items of Main Specifications

system	modified items
conmon items	(1) Setting of a self-operated vaccum relief valve (2) Exchange of neutral point amperemeters of unbalance amperemeters (3) Partial modification of dimensions of apparatuses and pipas, kinds of valves and measurement equipments and numbers of operators
M_1 loop	(1) Modification of construction of flow rate arround oriffices and a bore diameter of a motor operated valve (2) Addition of a drain valve to MT_1
M_2+A loop	(1) Modification of construction of flow rate arround oriffices (2) Modification of a bore diameter of safety valve of H_{31}
Pressurised water system	(1) Change of methods of flow rate control (constant) and level control (on/off control for a makeup pump and a pressurised flow valve, deletion of a pressurised water recovery line) (2) Modification of assignments of the function of a pressuriser and a water seperator (3) Demeneralized water is supplied directly to the hydrazine tank and automatically to the demeneralized water tank (4) Inlet-outld valves of apparatus for maintenance are deleted
U_c system	(1) Modification of the place of a outlet electrically operated valve of the elevated tank and outlet hand valves of apparatuses (2) Setting of a flowmeter in the supplying line
M_u system	(1) Modification of valves and piping roots by modification of the operation methed (2) Addition of check valves, setting of supplying header flowmeters at the upperstream side of check valves (3) Five compressors were in series and an expansion tank was settled
M_p system	(1) Two loops of MB column and CB column were in paralle and parts of valves of the reproduction line- and vaccum line were deleted. (2) Two temperature controllers were in parallel so as to simultaneously purify and reproduction helium gas with copper oxide beds. (3) The change of sampling line.

Table 1.7   Confirmation Items of Fabrication and Testing

Large item	Item	Confirmation item
Material	1) High tmeperature material more than 1000°C	Graphite (1000-1300°C), Super thermo, Molybdenum (1050°C), Hastelloy X and Incoloy 800 H (700-1000°C) are used and the delivery inspection is carried out in regard to metals.
	2) Packing material	A vortex gasket (Grafoil+SUS) or a metal O - ring is used.
	3) Nondestructive inspection	In regard to a valve box made of cast steel and a compressor, Radiographie inspection is carried out.
Welding	1) Extent of butt welding	Pipes of design temperature more than 400°C and of helium loop more than 2^B are but welded.
	2) Nondestructive inspection	In regard to the but welding of pipes and heat exchanger tubes, radiographic inspection is carried out.
	3) Pressure test	In regard to test pressure, temperature corre-ction is made by allowable stress.
Helium tech-nology	1) Frange section	A lip which is possible for seal welding is settled. A frange section of pipe seal welded
	2) Transmitter	The lead piping is connected with welding or swage rock, and in regard to a drain valve is connected with tip blanking screw.
	3) Type of valve	A bellow seal valve with backup grand
	4) Pressure passing through part of thermocouple	Byton and Teflon is used as sealant and cap is screwed. The temperature of heater element is insulated by boron nitride etc.
	1) Thermal insulator	The convection is prevented by a line, a scr-

		een foil, a laminated thermal insulator, compressed packing of thermal insulator and a seal plate.
High temperature structure	2) Structure analysis	Structure analysis of a seal plate, a nozzle part , bellows and so.
	3) Trial examination	Trial examination is carried out in regard to H_{32} heater elements and high temperature piping.
		Helium leak test of passing through part of thermocouple is carried out.

Table 1.8　CRT Response Time with Modified Design

Date	1981.6	1981.7	1981.8	1981.9	1981.10
Display response time	S_t : 3~5 sec G_p : about 10 sec	S_t : 0.8~3.4 sec G_p : less than 2.8 sec	S_t : o.2~1.5 sec	S_t : less than 1 sec G_p : less than 2.5 sec	S_t : less than 2 sec (in various condi-tion)
Abnormal detective display time	less than 2sec	————	less than 1 sec	————	
Modified items		•E link of nonstanding program •Move nonstanding program to bulk core memory •Standing of E B table •Standing of key-in acceptance program •Priority of key-in acceptance in refleshing pictures •Endlessness of reflesh task •Coding of apparatus deal-ed by graphic display •Decrease of number call-ing file access	•A transmission cir-cuit was devided into two •Firm ware of condi-tion detection •Move a part of non-standing data file to to bulk core memory	•Improvement of soft ware package	•Summarization of access of date file •Standing of data file •Modification of print interval •Firm ware of alarm summary •Modification of dis-play control appara-tus

S_t : Pictures of TAG No. LIST, ALARM LIST, SUMMARY GROUP, Chorie of record points, mechanical operation
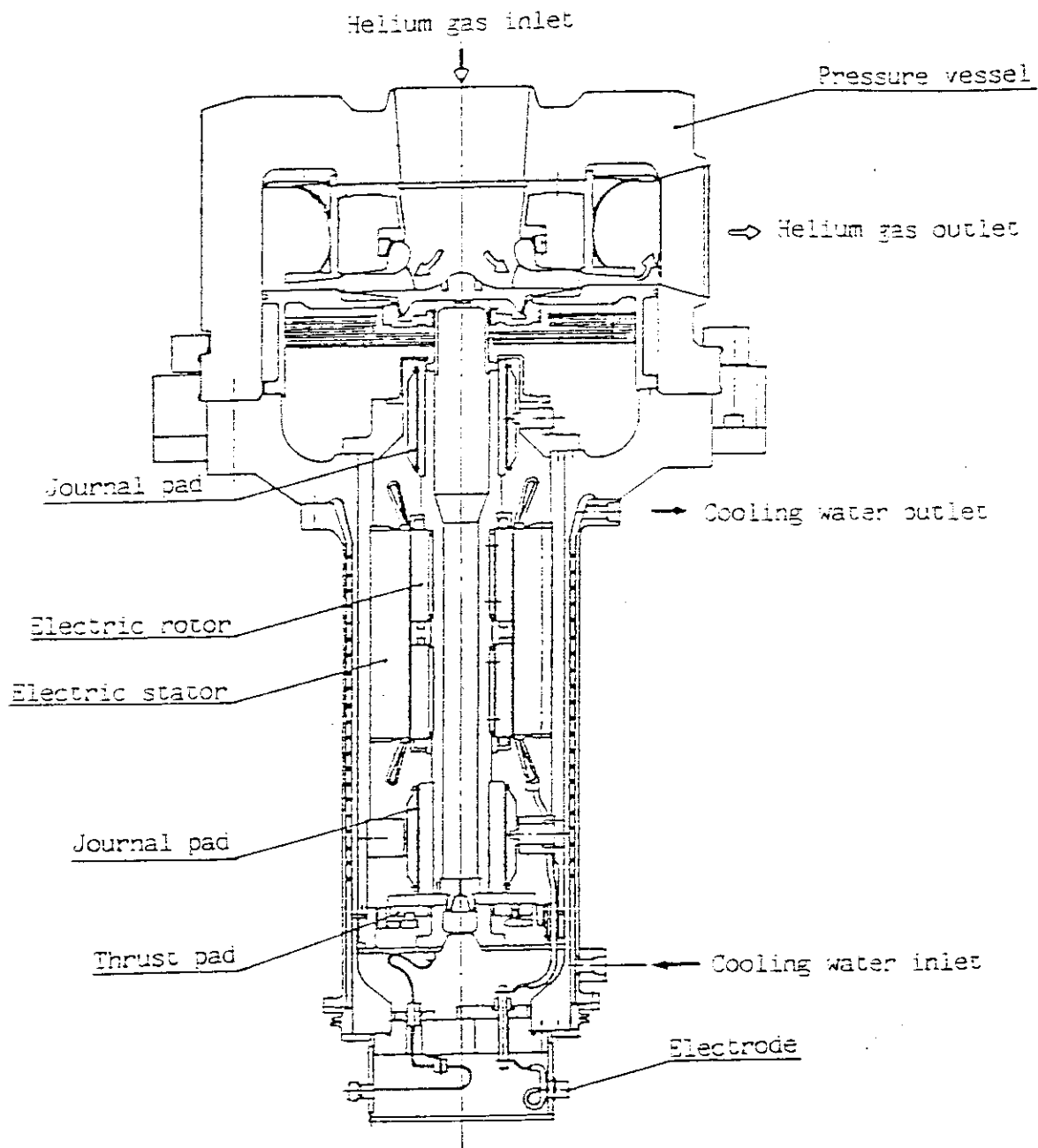G_p : Graphic pictures

Helium gas inlet

Pressure vessel

Helium gas outlet

Journal pad

Cooling water outlet

Electric rotor

Electric stator

Journal pad

Thrust pad

Cooling water inlet

Electrode

Fig. 1.12   Gas Circulator

Table 1.9 Test and Inspection Items of Gas Circulator

○ Witness

Items		Test and inspection	Casing lower frange	Cooling water jacket	Main impeller	Shaft
1	Material test	(1) Chemical composition analysis	○	○	○	○
		(2) Mechanical test	○	○	○	○
		(3) Nondestructive test	○			○
2	Material confirmation	(1) Millseat	○	○	○	○
		(2) Appearance measure inspection	○		○	○
		(3) Markshift	○			
3	Welding inspection	(1) Radiographic test			○	
		(2) Liquid penetrant test			○	
4	Pressure and pneumatic test	(1) Pressure test	○	○		
		(2) Pneumatic test	○			
		(3) Helium leak test	○			
5	Completion test	(1) Appearance inspection	○	○	○	○
		(2) Flushing inspection	○	○	○	○
		(3) Measure inspection	○	○	○	○
6	Motor test	(1) Winding resistance measurment		○		
		(2) Insulator resistance measurement		○		
		(3) Insulator proof test		○		
		(4) No-load test		○		
		(5) Binding test		○		
7	Instrumentation test	(1) Thermocouple electromotive voltage test		○		
		(2) Speed indicator electromotive voltage test				
8	Dynamic balance	(1) Low speed test		○		
		(2) High speed test (with impeller)		○		
		(3) High speed test (without impeller)		○		
		(4) The highest speed steady test		○		
9	Performance test	(1) Performance test (in air)		○		
		(2) Performance test (in helium) start and stop test 10 times continuous running 24 hr		○		

Table 1.10   Test Items and Their Remarks of T_1-section

Test item	Remask
Heat transfer and fluid dynamics test in single channel	The evaluation of heat transfer and fluid dynamics with a coolant channel and a fuel pin. Test components are the same size and shope as those in VHTR core.
Fuel pin vibration test	The investigation of vibration of fuel pin iduced by coolant flow.
Flow characteristics test with controll rod simulator	The investigation of flow characteristics when a controll rod sumulator is inserted into normal temperature and high pressure gas.
Heat transfer and fluid dynamics test in multi-channel	The evaluation of heat transfer and fluid dynamics in the case that each channel has an equal or inclined thermal oupput. The investigation of the influence of leak flow through contact surface between graphite blocks The investigation of heat transfer characteristics when one or some channels out of twelve are choked.
Heat transfer characteristics when blowers stop	(1) Reverse flow test in the pressure vessel (2) Natural circulation test through the vessel and coolant piping

Table 1.11　Item and Specification of T_1

	Test item	Coolant condition			Measuring position				Special Instrumentation
		Temperature Inlet/Outlet (°C)	Pressure (kg/cm²g)	Flow rate (g/s)	Temperature	Pressure	Flow rate	Power Supply	
Single channel test rig	Heat transfer and fluid dynamics test — middle temp. / high temp.	270/750 400/1000	~40		Ⓐ, Ⓑ, Ⓒ	Press. at B ΔP between B in each graphite block	Inlet pipe bypass pipe line	Simulated fuel rod	Turbulent flow
	Fuel vibration	~100		3~50	Ⓑ	Do.	Do.	—	Vibration
	Simulated control rod insert	~400			Ⓑ, Ⓒ	Do.	Do.	—	Turbulent flow
Multi channel test rig	Heat transfer and fluid dynamics test — middle temp. / high temp.	270/750 400/1000	~40	40~400	Ⓐ, Ⓑ, Ⓒ, Ⓓ, Ⓔ	Press. at B ΔP between B	Inlet pipe	Inlet Pipe	Flow distribution to each channel
	Natural circulation	270/750			Ⓐ, Ⓑ, Ⓒ, Ⓓ, Ⓔ, Ⓕ	Do.	Do.	Do.	Flow rate at natural circulation loop

Note

Ⓐ　: 　Surface of fuel pin simulator

Ⓑ　: 　Inlet and outlet of test element

Ⓒ　: 　Compensation heater blocks

Ⓓ　: 　Inlet and outlet of channel

Ⓔ　: 　Inner parts of fuel block simulator

Ⓕ　: 　Gas in natural circulation loop

Table 1.12   R & D Tests of Thermo-couples

materials of Thermo-couple	Temp.	300~1000°C			1200°C			Remark
Element	Sheath	A[1]	B[1]	C[1]	A[1]	B[1]	C[1]	
K	Inconel 600	◎	◎	○	◎	◎	△	Inconel sheath is easy to permeate the MgO insulator and cause short circuit
PR	Inconel 600	○	×	○	◎	×	△	
PR	PR	○	○	○	◎	◎	◎	high price
PR	Ta	○	△	△	○	×	×	Tantalum is carburized at high temperature
W－Re	Ta	○	○	△	○	◎	×	

Note 1)   A: Compatibility with graphite

   B: Stability of electromotive force

   C: Anticorrosion characteristic

   2)   Insulator is MgO in energy case

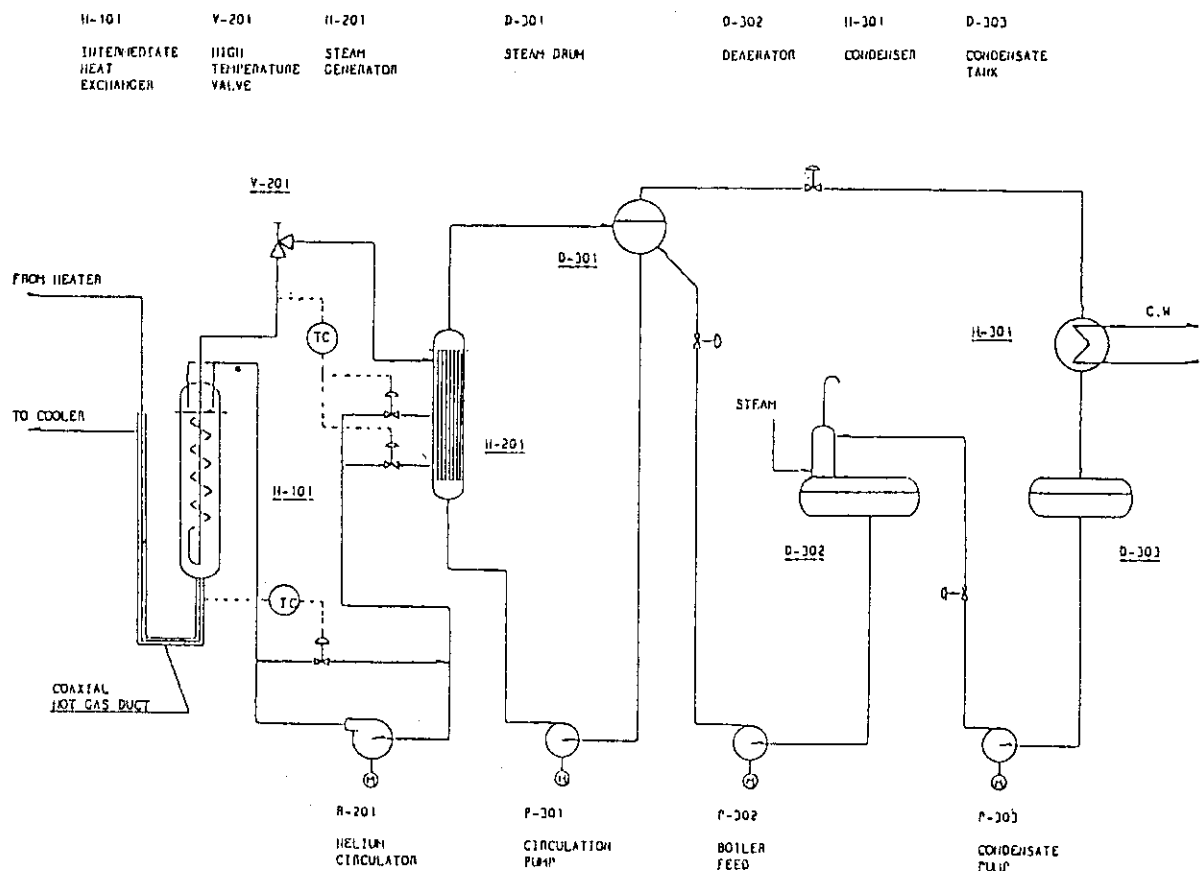A-A CROSS SECTION
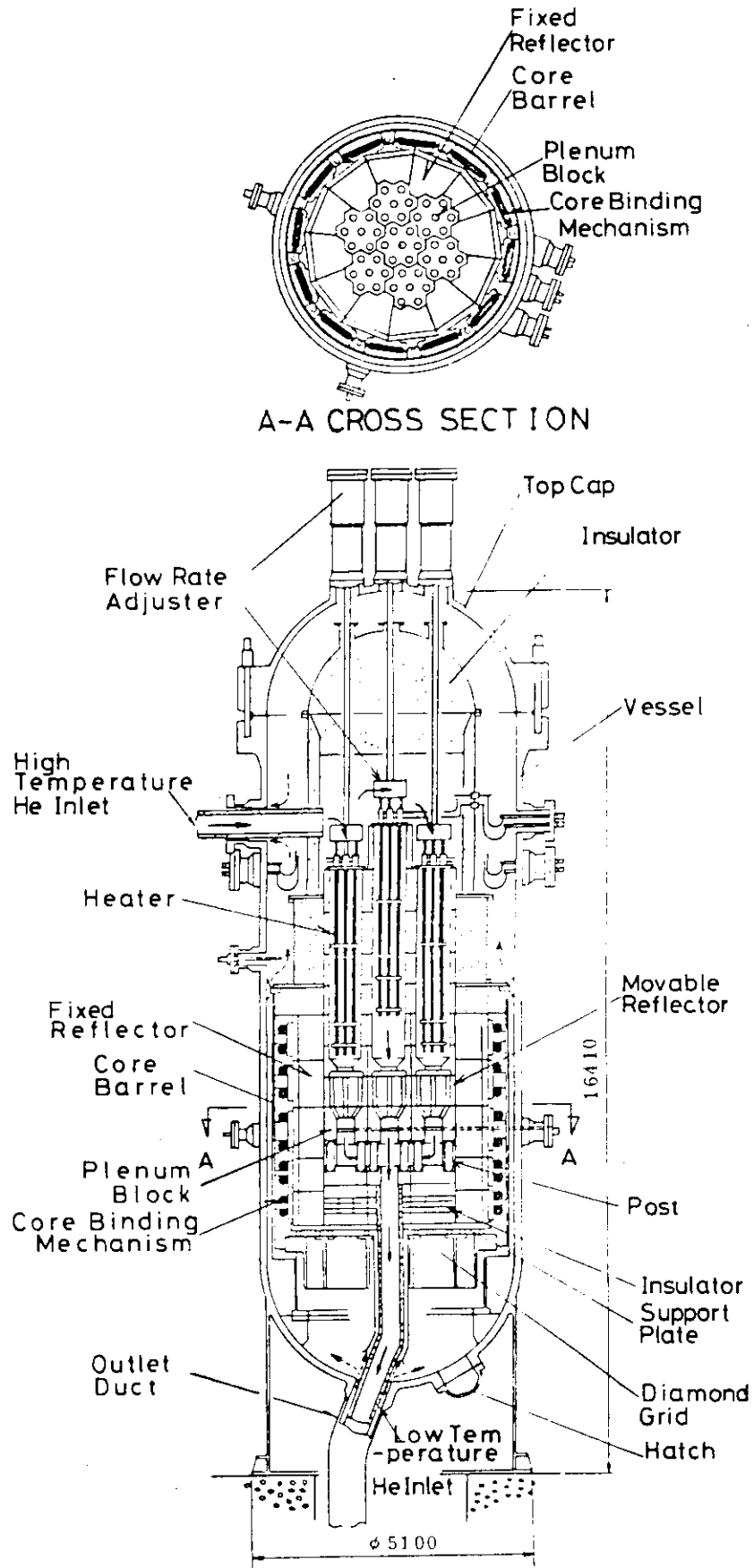
Fig. 1.13 T$_2$ Test Section
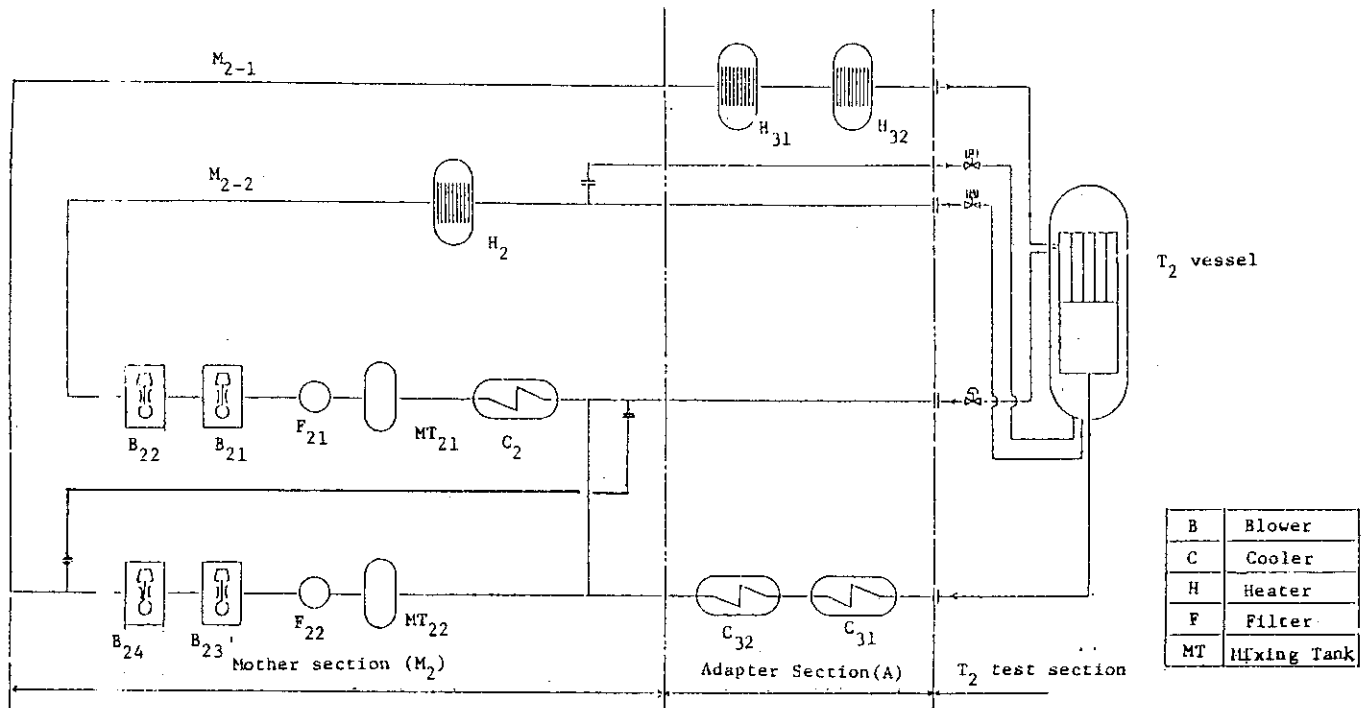
Fig. 1.14   Flow Sheet of T₂ Test Section

H-101	Y-201	H-201	D-301	D-302	H-301	D-303
INTERMEDIATE HEAT EXCHANGER	HIGH TEMPERATURE VALVE	STEAM GENERATOR	STEAM DRUM	DEAERATOR	CONDENSER	CONDENSATE TANK

Fig. 1.15   Flow Diagram of Test Section No.4

Table 1.13 T_4 Specifications

Items	Unit	
1. Primary Helium Circuit		
1) Flow Rate	kg/s	2.8
2) Operating Temperature		
M+A Heater Outlet	°C	1000
IHX Inlet	°C	986
IHX Outlet	°C	377
3) Operating Pressure	kg/cm²G	40
2. Secondary Helium Circuit		
1) Flow Rate	kg/s	2.73
2) Operating Temperature		
IHX Outlet	°C	930
SG Inlet	°C	910
SG Outlet	°C	279
IHX Inlet	°C	310
3) Operating Pressure	kg/cm²G	43
3. Steam/Water Circuit		
1) Flow Rate of SG	kg/s	36.7
2) Temperature of Steam	°C	233
3) Pressure of Steam	kg/cm²G	30
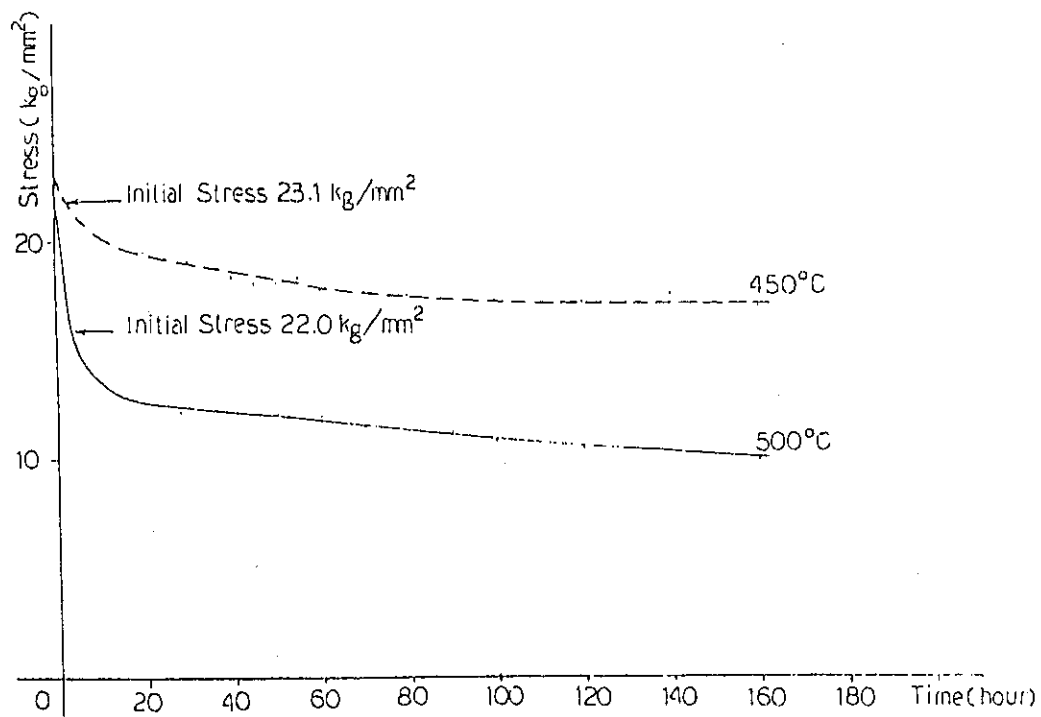
Fig.1.16 Stress Relaxation of 2-1/4Cr-Mo

2. RESEARCH ON THERMAL STRUCTURE

2.1 Flow Leakage into Plenum

K. Kikuchi, M. Futakawa, T. Takizuka, H. Kaburaki and K. Sanokawa

In order to get the outlet gas temperature of 1000°C of VHTR the estimation of the leak flow inside core is considered to be important. Because the reactor core consists of stacking hexagonal fuel blocks, reflector blocks, thermal barrier blocks and other components, the leak flow of coolant gas occurs between the block elements of in-core struc- ture.   This leak flow might have an adverse effect to the sufficient cooling of fuels.

The purpose of this study is to estimate the leak flow rate, particularly flowing into a plenum directly through the gaps of plenum blocks, fixed reflector blocks and thermal barrier blocks.

Figure 2.1 illustrates an over-all view of about 1/2.75-scale bottom core, weight blocks, core restrainers and differential pressure apparatus.   Working fluid is air at atmospheric pressure and room tem- perature.   Changing the restraining force and the differential pressure between inside and outside the plenum, the leak flow rate is measured by laminar flow meters and the block gaps by non-contacting displacement transducers of eddy-current type.   The differential pressure and suction flow rate of a blower are max. 0.25 kg/cm^2 and 8 Nm^3/min. respectively.

The effects of seal elements placed between the gaps of upper plenum blocks and lower fixed reflector blocks are evaluated to reduce the leak flow rate.   Seal elements are graphite sheet and SUS foil. To simulate the block gaps due to the thermal expansion shims are in- serted.

Figure 2.2 shows that the leak flow rate is related nonlinearly to the differential pressure and in inverse proportion to the restrain- ing force.   Seal elements on the top of the upper plenum blocks are very effective to prevent leak flow.

Current study is intended to estimate local leak flow rate, because leak flow path consists of many kinds of partial flow chennels, for instance, through seal elements, plenum blocks, chamfered corner of blocks and so on.

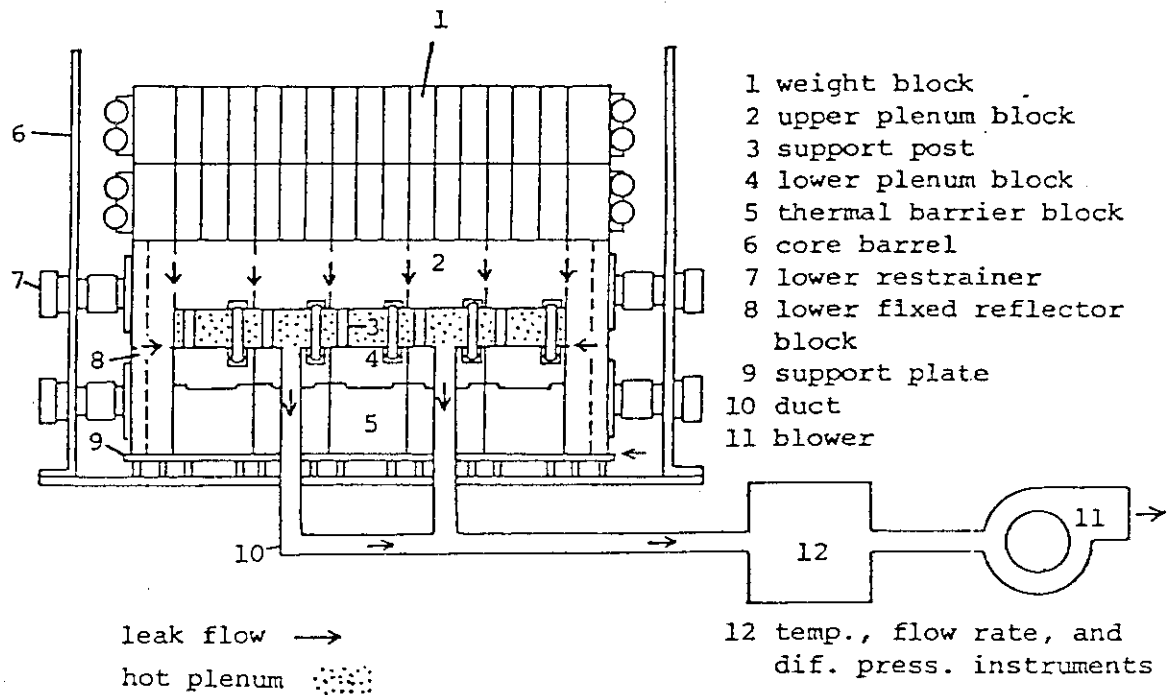Detailed analysis to evaluate the practical leak flow rate in VHTR core is now in progress.

1 weight block
2 upper plenum block
3 support post
4 lower plenum block
5 thermal barrier block
6 core barrel
7 lower restrainer
8 lower fixed reflector
  block
9 support plate
10 duct
11 blower

leak flow ⟶
hot plenum ⠰⠶⠶

12 temp., flow rate, and
   dif. press. instruments

Fig.2.1 Test rig of in-core structure. This model mainly
         simulates the bottom-core structure of about
         1/2.75—scale VHTR core. Working fluid is air.
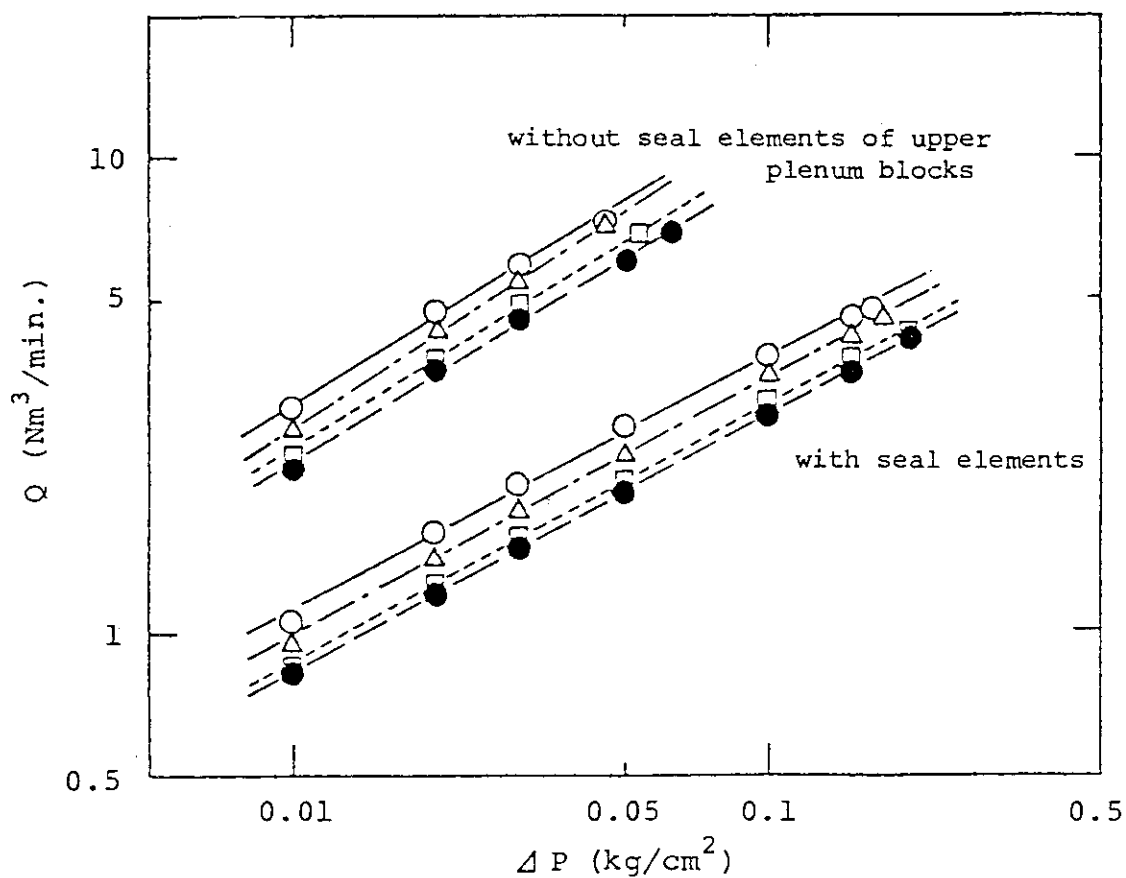
$$\log(Q) = A \log(\varDelta P) + B$$

restraining force (kg)	without seal elements of upper plenum blocks		with seal elements	
	A	B	A	B
◯ 0	0.583	3.80	0.528	2.53
△ 100	0.637	3.93	0.542	2.47
□ 325	0.607	3.69	0.538	2.33
● 650	0.611	3.63	0.534	2.27

Fig.2.2 The relation between differential pressure ($\varDelta$P) and leak flow rate (Q). In both cases keys and seal elements (Gr.+SUS) are inserted between the gaps of fixed reflector blocks. Restraining force is added per one fixed reflector block. Lines are fitted by the least square method

2.2 In-Core Flow Test

T. Takizuka, H. Kaburaki, T. Kunugi, K. Hashimoto and K. Sanokawa

The core of VHTR is constructed with graphite blocks. Most of the primary coolant flows downwards through annular cooling channels of fuel blocks. The coolant partly bypasses through clearance gaps between the interfaces of fuel blocks on account of a nonuniform graphite dimensional change csused by thermal expansion or irradiation. This flow is called crossflow. In order to minimize the crossflow seals are placed between hot plenum blocks and fixed reflector blocks. The coolant may leak across the seals and enters directly into hot plenum. Since bypass and leakage flows have an adverse effect on the normal core flow distribution to keep adequate core temperature, it is required to prevent these short-passed flows.

Therefore. a two-block test. a one-column test and a sealing test are conducted.

Two-Block Test

The main objective of the two-block test is to study the magnitude and the path of the crossflow at the interfaces of graphite fuel blocks and control rod blocks. Figure 2.3 shows an overall view of a test rig. Two stacked full-scale graphite test blocks are placed in the rig and are surrounded by a shroud which serves to control bypass pressure and to measure crossflow rate. Air at atmospheric pressure and room temperature is used as fluid. The test rig is equipped with a load adjusting apparatus to produce pressure at the block interface. The simulation of the interface gap due to non-uniform graphite deformation is established by lifting the upper block or placing shims between blocks.

One-Column Test

The objective of the one-column test is to determine the flow distribution in the fuel column. The test model comprised of 9 full-scale graphite blocks stacked in an acrylic sheath pipe with hexagonal cross section. The gap between the test column and the sheath pipe wall simulates the vertical bypass gap between columns.
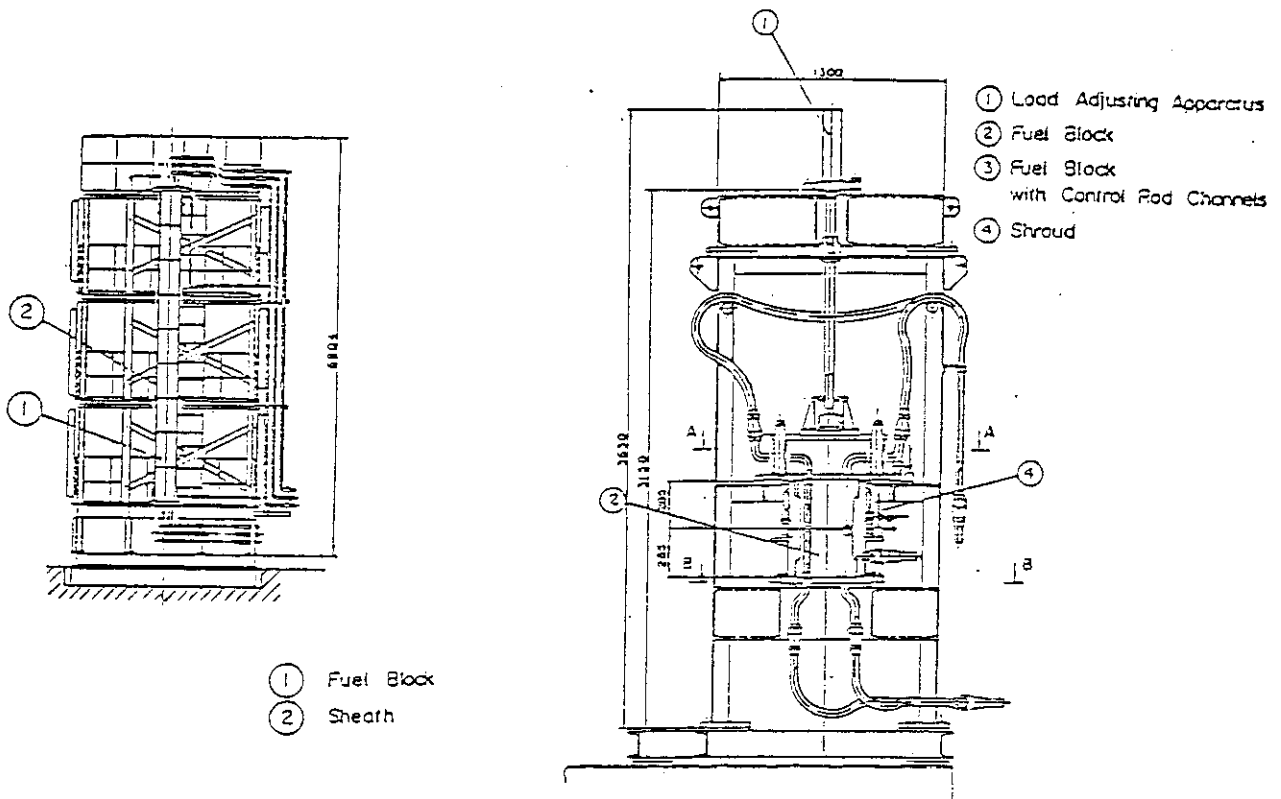
An overall view of a test rig is also shown in Fig. 2.3.

Sealing Test

Current design approach for preventing the direct bypassing of coolant into plenum is to place the sealing elements in the leakage

flow paths at the interface gaps between the hot plenum blocks and the fixed reflector bolcks. Sealing elements of various materials (graphite, flexible graphite and metal) are tested to evaluate the leakage flow rate as a function of pressure difference.

Figure. 2.4 shows a sealing element test rig.

① Load Adjusting Apparatus
② Fuel Block
③ Fuel Block
   with Control Rod Channels
④ Shroud

① Fuel Block
② Sheath

1 - Column Test Rig

2 - Block Test Rig

Fig.2.3　Crossflow Test Rig

① Load Adjusting Apparatus
② Fixed Reflector Block
③ Bottom Insulator Block
④ Plenum Block (Ⅱ)
⑤ Plenum Block (Ⅰ)
⑥ Sealing elements
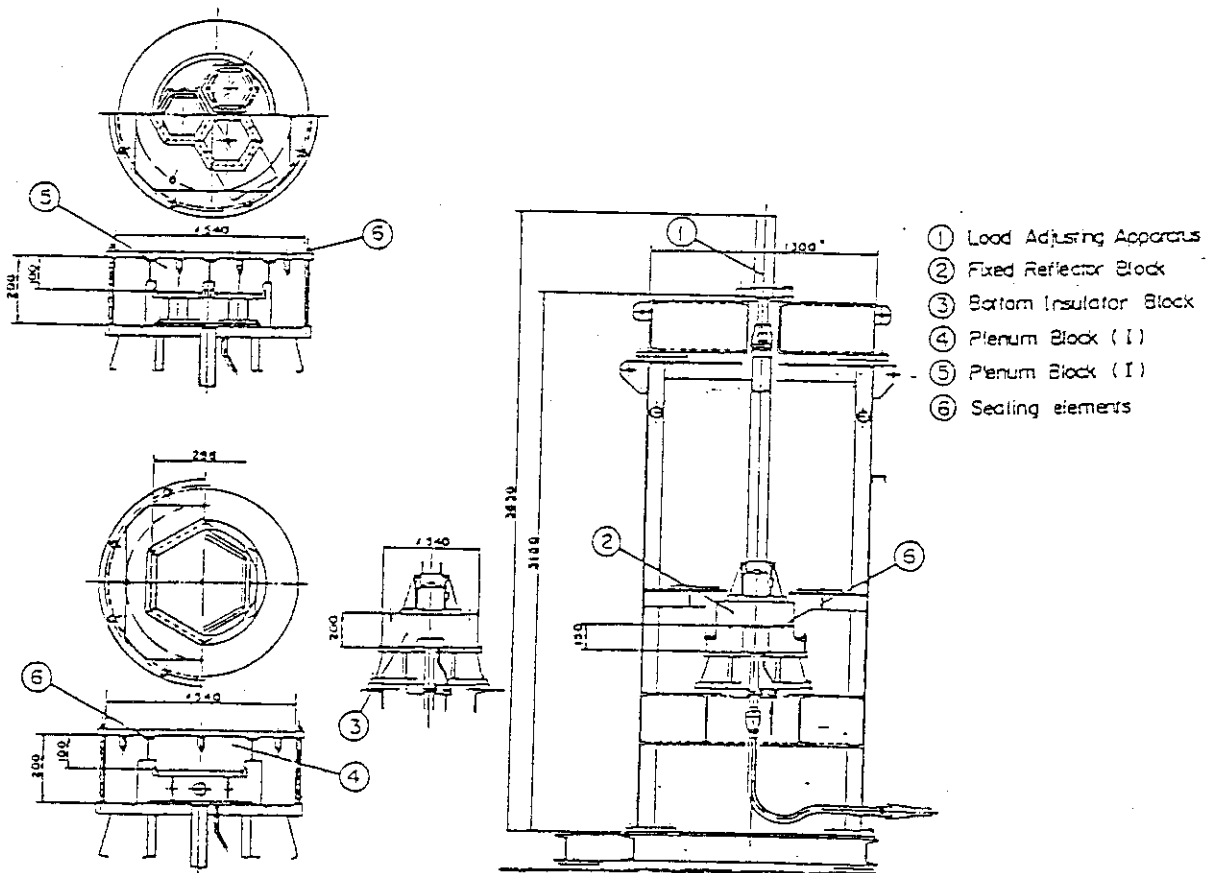
Fig.2.4　Sealing Element Test Rig

2.3 Preliminary Thermal Mixing Test

T. Kunugi, H. Kaburaki and T. Takizuka

In VHTR core, coolant which flows through channels of each fuel block is collected and mixed in a plenum region.

In order to measure the average exit temperature of coolant into the plenum, a temperature sensor (thermocouple) is installed within a core support block which is placed just above the plenum.

The objectives of a preliminary thermal mixing test are to know the coolant characteristics of mixing of 7 jet streams in the plenum such as:

1. Mixing characteristics by nozzle angle configulations.
2. Temperature distribution of coolant within the core support block.

Discription of an apparatus

Test models consist of 3 one-half scale core support block.

Each model is connected by acryle flanges. The flow sheet of this experimental equipment is shown in Fig. 2.5. A duct which connects a blower to a test section includes two flow control valves and a flow meter. Also two 5kw electrical heaters are used to supply heated air to inlets of the model. A thermocouple rake with 11 thermocouples to measure the gas temperature is installed in the model.

Experimental conditions

The experimental conditions are as follows:

Working fluid   : Air at atmospheric pressure
Temperature range   : max. 50°C at the inlet of the model
Total gas flow rate   : max. 6 Nm^3/min

The scale factors and nozzle angles of the models as shown in Fig. 2.6 are as follows:

Plenum diameter of core support
block and main pipe diameter D   : 176 cm
Branch nozzle diameter d_1, d_2, d_3 : 17.5, 25, 35 and 46 cm
Nozzle angles Θ : 30°, 38.7°, 45°, 60° and 90°
Plenum height   : max. 200 cm

Reference

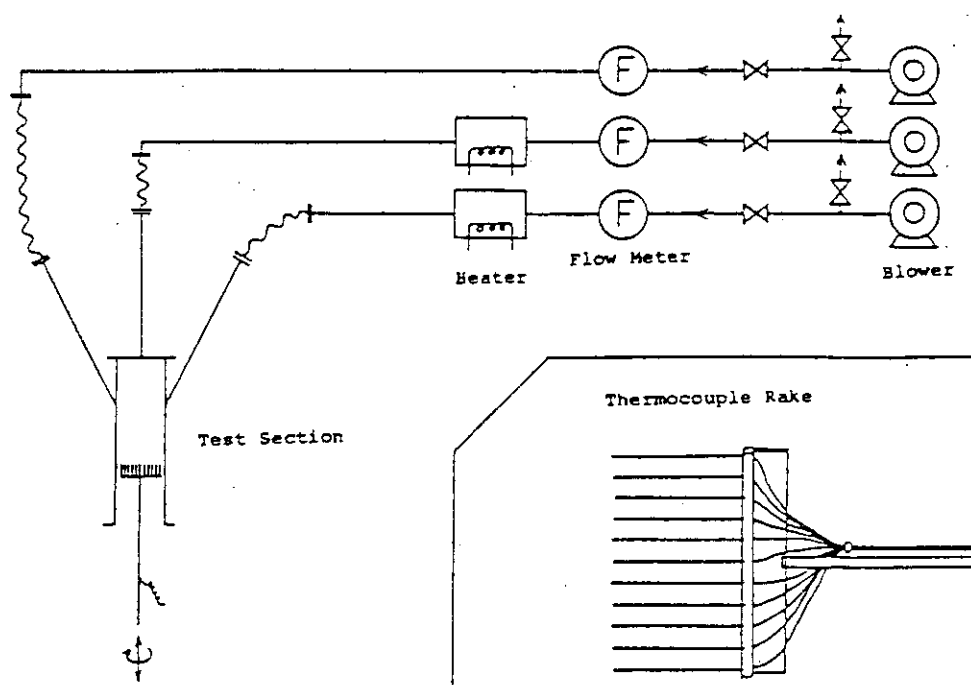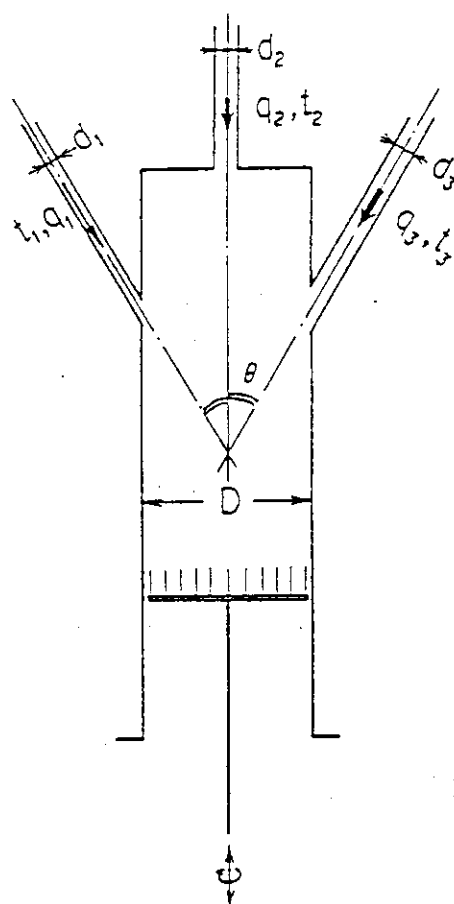1) E. Chin: "Core Support Block Thermal Mixing Test Analysis Report," GA-A15329 (1979).

Fig.2.5 Flow Sheet of Experimental Equipment
and Sketch of Thermocouple Rake

D : Plenum Diameter

d_1, d_2, d_3 : Nozzle Diameter

t_1, t_2, t_3 : Temperature

q_1, q_2, q_3 : Flow Rate

θ : Angle

Fig.2.6 Test Section

2.4 Crossflow Experiment

H. Kaburaki, T. Kunugi, T. Takizuka and K. Sanokawa

In VHTR core which is composed of piled-up graphite blocks, crossflow between the block interface is very severe to the establishment of expected flow distribution. Therefore leakage through a gap between contacting surfaces was examined. Measurements were made for the leakage mass flow and the pressure difference across the contacting graphite surfaces. Theoretical leakage flow model was devised and the equivalent interface gap was evaluated from the experimental data.

Experimental Methods and Results

Experiments were carried out with cylindrical graphite blocks (diameter: 60 mmφ, height: 145 mm) as shown in Fig. 2.7. Leakage flow rate through a block interface gap was measured by a mass flow meter under the applying the pressure difference of 0 ∿ 1.0 kg/cm^2 across contacting surfaces. All experiments were conducted using nitrogen and helium gas at room temperature and atmospheric pressure. The normal static loading pressure applied at the block interface ranged from 0.11 to 1.36 kg/cm^2. The results of this experiment (Fig. 2.7) showed that the leakage flow of nitrogen gas was larger than that of helium gas under the same contacting conditions. It was also found that the gas permeation through graphite blocks could not be neglected. Therefore the true leakage flow data through a block interface gap, i.e. with extraction of gas permeation from the leakage flow data of Fig. 2.7, were plotted in Fig. 2.8. A linear relation between leakage flow and pressure difference is plausible and the slight deviation may be due to the compressibility effects of gas and the reduction of the interface gap caused by pressure difference.

Analysis

The following model is devised to analyze the above-mentioned experimental results. As for the contacting of surfaces, it is generally recognized that the two surfaces are supported by a random array of asperities distributed over each surface. So it is plausible to assume that the flow of gas between contacting surfaces is modeled as a two-dimensional flow of gas between two parallel plates as shown in Fig. 2.9. If an equivalent gas δ is very small compared to other dimensions of the surface, the gas flow through the gap is laminar and two-dimensional pressure distribution p=p(x,y) between parallel plates

is expressed by

$$\frac{\partial}{\partial x} \left(\frac{\delta^3}{\mu} \rho \frac{\partial P}{\partial x} \right) + \frac{\partial}{\partial y} \left(\frac{\delta^3}{\mu} \rho \frac{\partial P}{\partial y} \right) = 0 \tag{1}$$

where μ denotes a viscosity coefficient and ρ is a density of gas.
In the case where pressure difference amounts to atmospheric pressure,
compressibility must be taken into consideration. Assumptions are now
made that the flow is isothermal and fully developed, the pressure
equation (1) becomes

$$\frac{\partial^2 P^2}{\partial x^2} + \frac{\partial^2 P^2}{\partial y^2} = 0 \tag{2}$$

For the type of problem under consideration, Eq. (2) is transformed in
cylindrical coordinates (Fig. 2.10).

$$\frac{1}{r} \frac{\partial}{\partial r} \left(\frac{\partial P^2}{\partial r} \right) + \frac{1}{r^2} \frac{\partial^2 P^2}{\partial \theta^2} = 0 \tag{3}$$

With Eq. (3) and the boundary conditions: $p=p_i+p$ at $r=r_o$ and $p=p_i$
(atmospheric pressure) at $r=r_i$, a mass flow rate M between circular
plates becomes

$$M = \frac{\pi \delta^3}{6\nu} \frac{\Delta P}{\ln(r_o/r_i)} \left(1 + \frac{\Delta P}{\partial P_i} \right) \tag{4}$$
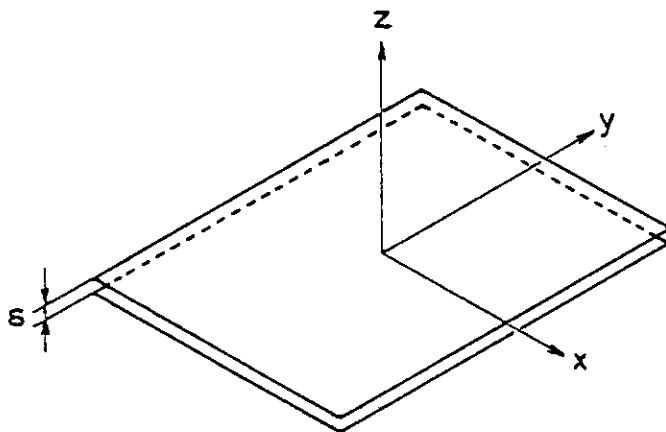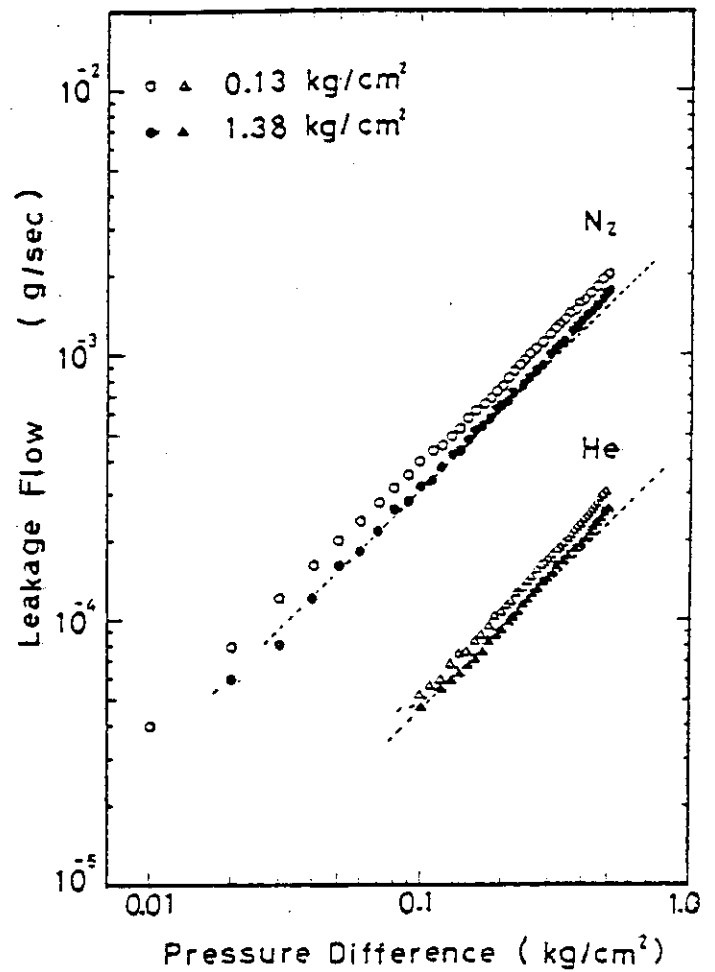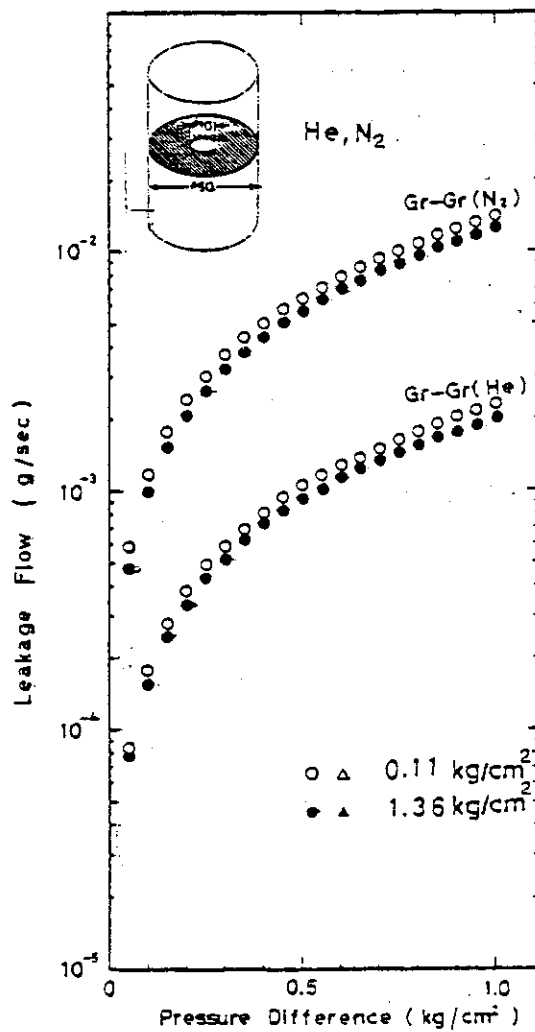
ν denotes a kinematic viscosity of gas. The values of r_o and r_i are
the outer and inner radii of the circular plates respectively.
The second term in Eq. (4) shows the effect of gas compressibility
and can be neglected when $\Delta p << p_i$. It is needless to say that the case
is different with that of a slip flow. Eq. (4) is used to predict the
equivalent interface gap δ for the contacting graphite blocks.
The estimated values of δ are as follows:

δ	Applied pressure at the block interface
12.0 $\sim$ 12.5 μm	0.13 kg/cm^2
11.3 $\sim$ 12.0 μm	1.36 kg/cm^2

It is seen that the equivalent gap δ tends to decrease with the appli-
cation of static load at the block interface.

Conclusion

The results of the experiments showed that the leakage gas flow through an interface gap between contacting graphite blocks was well described by the two-dimensional laminar gas flow between parallel plates and the estimated equivalent gap δ ranged from 11.3 to 12.5 μm.

Fig.2.7 Leakage Flow Test Results

Fig.2.8 Leakage Flow Through a Block
Interface Gap

Fig.2.9 Parallel Plates

Fig.2.10 Test Model
(Cylindrical Coordinates)
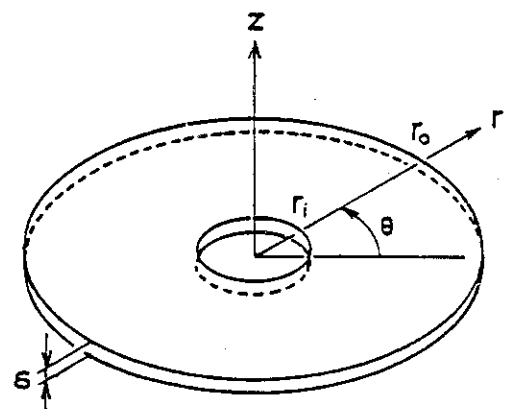
2.5 Numerical Calculation of Crossflow Pressure Distribution

T. Kunugi, H. Kaburaki and T. Takizuka

The quantitative information for crossflow through gaps between fuel blocks is very important for a design of VHTR core. Therefore, a numerical calculation of pressure distribution of coolant is carried out under various boundary conditions.

If the gap between fuel blocks can be assumed as a parallel channel with clearance formed by the surface roughness, the following equations are derived for incompressible and compressible fluid respectively.

$$\nabla^2 P = 0 \qquad \text{for incompressible fluid} \tag{1}$$

$$\nabla^2 P^2 = 0 \qquad \text{for compressible fluid} \tag{2}$$

where, $\nabla^2 = \partial^2/\partial x^2 + \partial^2/\partial y^2$ and P is pressure.

Hexagonal fuel blocks used in VHTR core are very complicated because channel holes, dowel pins and handling hole are located at the top surface of the blocks.

Boundary-fitted coordinate system is very useful for the calculation of pressure distribution of crossflow in the complicated configurations such as hexagonal fuel blocks.

By using transformation, this method is also applicable to a complicated configuration. The technique of the boundary-fitted coordinate system is based on a method of automatic numerical generation of a curvilinear coordinate system. The curvilinear coordinates are generated as the solution of a set of elliptic partial differential equations with Dirichlet boundary conditions. The general transformation from a physical plane (x,y) to a transformed plane (ξ,η) is expressed by

$$\xi = \xi(x,y) \text{ and } \eta = \eta(x,y), \tag{3}$$

and inverse transformation is expressed by

$$x = x(\xi,\eta) \text{ and } y = y(\xi,\eta). \tag{4}$$

The Jacobian of the transformation is denoted by

$$J = J\left[\frac{x,y}{\xi,\eta}\right] = x_\xi y_\eta - x_\eta y_\xi \neq 0$$

The fuel block configuration is shown in Fig. 2.11. The computational grids on the transformation plane is shown in Fig. 2.12, the region of grids being 164(I-direction)x28(J-direction).

The simplest case of the grid-generation must be the Laplace equation in a physical plane:

$$\nabla^2 \xi = 0 \tag{5}$$

$$\nabla^2 \eta = 0 \tag{6}$$

Therefore, the transformed equations are:

$$\alpha x_{\xi\xi} - 2\beta x_{\xi\eta} + \gamma x_{\eta\eta} = 0 \tag{7}$$

$$\alpha y_{\xi\xi} - 2\beta y_{\xi\eta} + \gamma y_{\eta\eta} = 0 \tag{8}$$

where, $\alpha = x_\eta^2 + y_\eta^2$, $= x_\xi x_\eta + y_\xi y_\eta$ and $\gamma = x_\xi^2 + y_\xi^2$

Eqs: (7) and (8) can be solved by the finite-difference method, using second-order central differences, with successive over-relaxation (S.O.R) of dependent variables.

Thus, the discrete values of (x,y) at the corresponding grid point (ξ,η) are determined. The computational grid on the physical plane (x,y) is shown in Fig. 2.13.

The model equations (1) and (2) are transformed to the transformation equations. For incompressible fluid

$$(\alpha P_{\xi\xi} - 2\beta P_{\xi\eta} + \gamma P_{\eta\eta})/J^2 = 0, \tag{9}$$

and for compressible fluid

$$(\alpha P_{\xi\xi}^2 - 2\beta P_{\xi\eta}^2 + \gamma P_{\eta\eta}^2)/J^2 = 0. \tag{10}$$

After transforming quasi-linear elliptic equations (9) and (10) to finite-difference equations, these equations with the Dirichlet boundary conditions (The pressure difference between coolant channel and gaps between fuel blocks (ΔP) is 1.0.) are solved in a transformed plane by the S.L.O.R iteration.

The computational time was about 20 seconds on a FACOM M200 computer. One of the results is shown in Fig. 2.14. From these results the following conclusions are derived:

(i) Boundary-fitted coordinate system is effective for the estimation of the pressure distribution of crossflow.

(ii) Parallel channel model is appliciable to the estimation of the paths and the pressure distribution of crossflow.
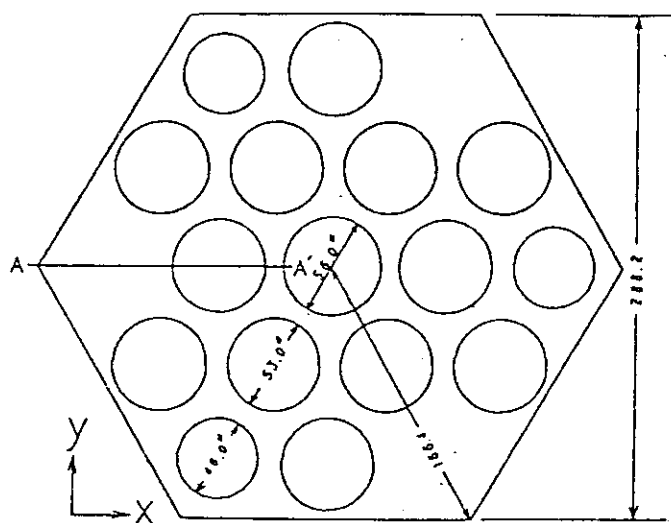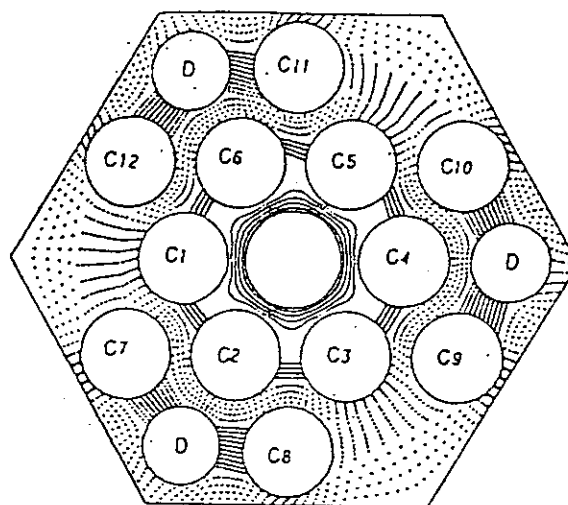
Fig.2.11   Fuel Block
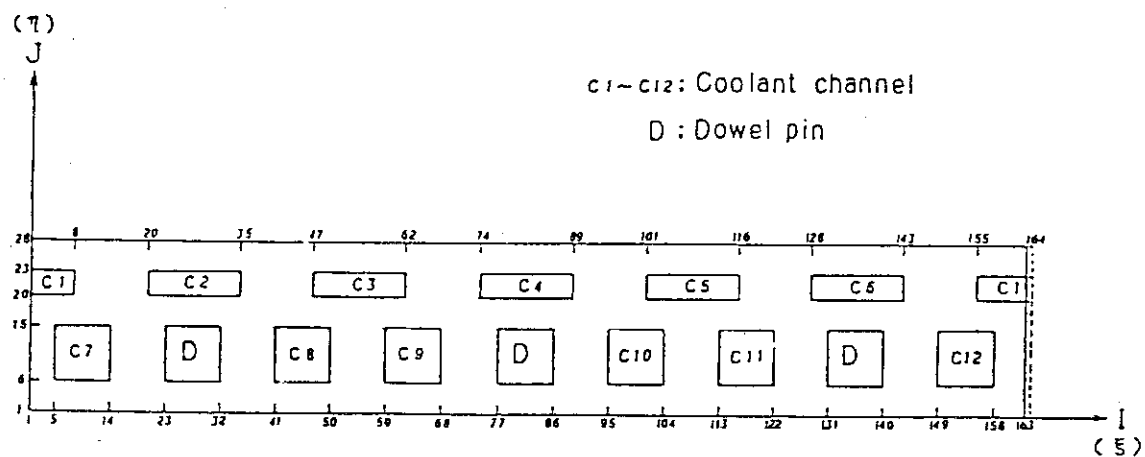

Fig.2.13   Computational Grids on
Physical Plane

$c_1 \sim c_{12}$: Coolant channel

D : Dowel pin

Fig.2.12   Grids on the Transform Plane
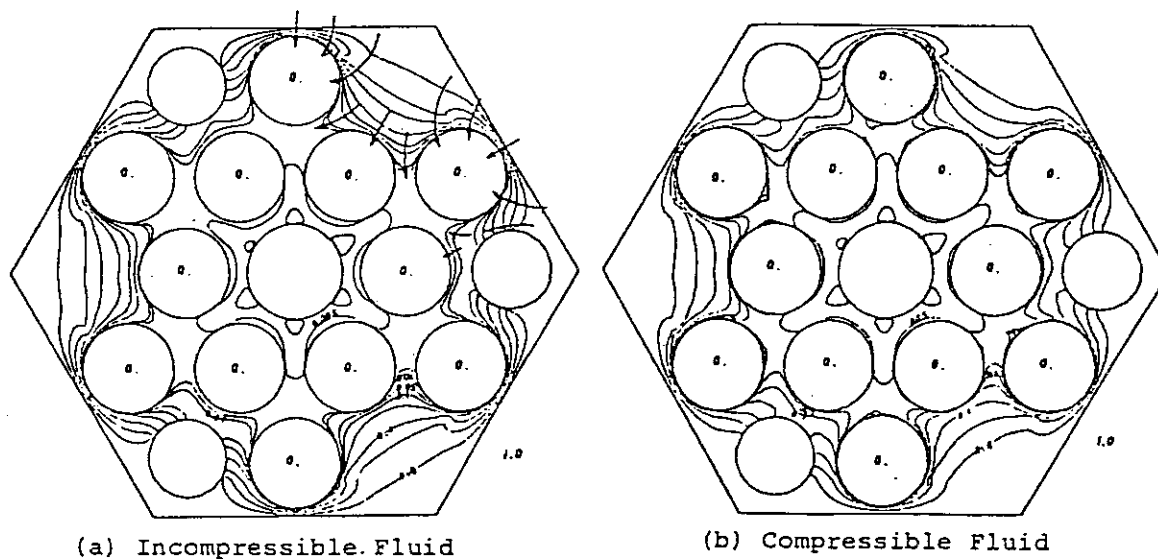

(a) Incompressible. Fluid

(b) Compressible Fluid

Fig.2.14   Contour Lines of Pressure

2.6 Dynamical Characteristics of Double Wall Piping Structure

M. Futakawa, K. Kikuchi and K. Sanokawa

Double wall piping structure is to be attached to a VHTR pressure vessel to connect an intermediate heat exchanger.

High temperature helium gas of 1000°C flows the circular channel of the inside of this inner pipe, and 400°C helium gas flows the annular passage between the inner and outer pipes.

The objective of this study is to obtain dynamical characteristics such as natural frequencies, mode shapes and damping factors of double piping structure.

The test model is a double pipe : a 14 cm dia. X 6 mm thickness X 4.5 m long pipe and a 10 cm dia. X 2 mm thickness X 4.5 m long pipe.

The inner and outer pipes are separated by bolt-type spacers at 4 points circumferentially and 7 points axially respectively. These spacers are fixed on the outer pipe. Number of axial supporting spacers is changeable and the outer pipe is simply supported at both ends by the mounting frams on the ground.

The natural frequencies of this model were measured with accelerometers by hammering responses.

In order to perform simply modified calculation, double wall structure is replaced by a parallel-beam model that has two parallel beams of inner and outer pipes having equivalent stiffness to each of pipes. And they are connected by spacer beams also having equivalent stiffnesses to the bolt-type spacers, as shown in Fig. 2.15. Natural frequencies and mode shapes are calculated with a SAP-V code.

Table 2.1. summarizes the natiral frequencies of experimental and numerical results.

The numerical results of the frequencies of straight double wall piping structure are in good agreement with experimental results.

We are now planning the next experiments to study the damping factor of this model and the vibrational characteristics of double piping structure composed of straight and curved pipes.
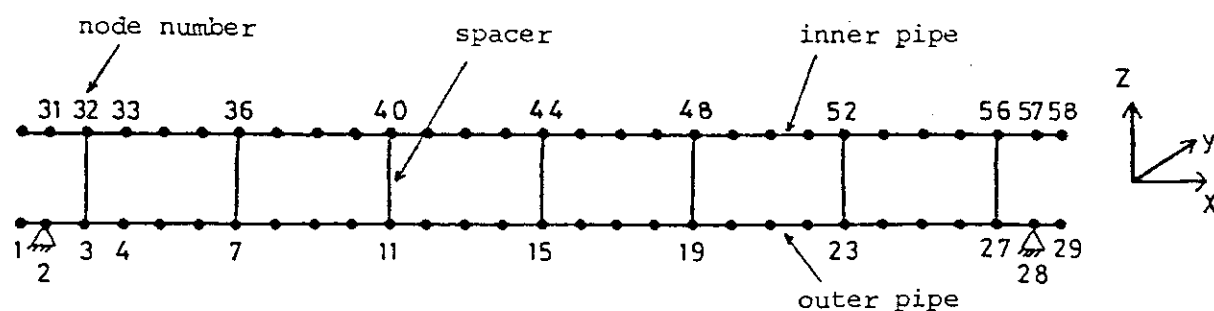
Fig.2.15　Element Mesh of the Parallel Beam Model　(7 Points Support)

Table 2.1　Comparison of Natural Frequencies

mode number		natural　frequency　　　　　(Hz)					
		double wall tube				inner tube	outer tube
		2 points support	3 points support	4 points support	7 points support		
1	experimental value	18.0	19.5	19.7	19.7	15.6	21.9
	numerical value	17.2	19.2	19.2	19.2	16.3	20.1
2	experimental value	21.9	66.4	74.6	75.8	61.7	82.0
	numerical value	20.4	66.5	75.8	76.0	64.6	79.5
3	experimental value	63.3	82.4	151.6	163.1	145.3	175.0
	numerical value	65.7	80.0	146.5	168.2	143.2	176.3
4	experimental value	81.1	102.4	176.6			
	numerical value	79.9	105.3	176.4			

3. RESEARCH ON HEAT TRANSFER AND FLUID DYNAMICS

3.1 Heat Transfer and Pressure Drop of Laminar, Transitional and Turblent Helium Gas Flow in Smooth Annuli Strongly Heated from Inside Wall

N. Akino, S. Nakauchi[*] and K. Hashimoto[**]

Introduction

A VHTR planned by JAERI is composed of block type fuel elements. Helium gas coolant flows through annular channels between the fuel rods and the inner walls of the holes in hexagonal graphite blocks. To get very high exit coolant temprature of 1000°C, flow rate is rather low, and Reynolds number is not large enough to be able to be considered that the coolant flow is in fully turbulent condition, in which heat transfer and pressure drop characteristics have been well established.

It is absolutley important for VHTR design to resolve the following problems for annular channels in transitional region;

(1) lack of experimental data and correlation of heat transfer and pressure drop

(2) lack of the knowledge about the flow behavior during transition

(3) determination of the occurrence of heated laminarization, which causes dangerous deterioration of heat transfer, observed for circular tubes.[1),2),3)]

A series of mesurements were made to study the annular flow of strongly heated helium gas in laminar, transitinal and turbulent regions.

Apparutus

Figure 3.1 shows the helium gas loop(SGL), which circulated pure helium gas up to 30g/s at 4 bar. Two tanks were settled to reduce pressure pulsation caused by a reciprocal type compressor.

At the upstream of test section, a heat exchanger was equipped to cool helium gas by liquid nitrogen so as to get higher heating rate condition. Figure 3.2 shows an annular heat transfer test section.

Helium gas entered from upper inlet nozzle and flowed downward through
an annular channel, which was composed of a heater rod and an outer tube
(inner diameter: 40.3 mm, length: 1,230 mm).

Three heater rods with different diameters of 28,32 and 34 mm were
used. They were made of buss parts (Ni, Cu) and heating parts (Inconnel-
600, SUS304). The heating part was about 0.9 m in length and was equipp-
ed with about 20 thermocouples. Electric current directly passed the
tube wall and generated heat by the Ohmic law.

Outer tube had 11 pressure taps to measure the pressure drop.
Outside of test section were insulated by two layers of mineral wool and
6 sets of guard heaters.

Experiment

Heat transfer and pressure drop were measured for the three
annular channels in the following conditions;

    (1) Reynolds number $Re = 700 \sim 30000$

    (2) Gas temperature $T_g = -150 \sim 400C$

    (3) Heat flux parameter $q_i^+ = 0.2 \times 10^{-3} \sim 15 \times 10^{-3}$

    (4) Eccentricity $E < 10\%$

$q_i^+ = q/(G \cdot c_p \cdot T_i)$

    q=heat flux,

    G=mass velocity,

    c_p=specific heat capacity of helium gas,

    T_i=inlet gas temperature

One of the most difficult technical problems was to reduce the
eccentricity between inner and outer tubes of the annuli. Large
eccentricity resulted in large scatter of measured heat transfer
coefficients. To improve it, position of the heater rod was moved at
the upper support by fine adjustment of screws and measured at the
middle of heating part by specially devised probes.

Result

Figure 3.3 shows the measured Nusselt and Reynolds numbers for the
34 mm-diameter heater rod at a downstream position. In the region of
Reynolds number below about 3000 the obtained Nusselt numbers agree
with analytical values for the laminar flow with constant properties.
For large Reynolds number and small heat flux parameter, Nusselt numbers
are parallel to Dalle-Donne's experimental correlation for turbulent
flow.[4] As heat flux parameter is increased, Nusselt numbers depart

from his correlation. But Nusselt numbers do not decrease below a lower limit line. This means that such strong deterioration of heat transfer observed in a circular tube does not occur for the annular channels heated from an inner tube up to a relatively high heating rate.

Figure 3.4 shows the measured friction factor. In laminar region, friction factor increases as hating rate increses. By contrast, in turbulent tegion, friction factor decreases as heating rate increases.

Conclusion

Fundamental charateristics of heat transfer and pressure drop of the annular gas flow are clarified by this experiment.

Theoretical and experimental explanation of the existence of a lower limit line and the absense of heat tranfer deterioration by heated laminarization should be studied hereafter.

Reference

1) C.A. Bankston, Trans, ASME, C92, R569 579 (1970).

2) C. W coon, et al., Trans ASME, C92, p. 506 512 (1970).

3) Y. Mori, et, al., J. Japan Mechanical Enger, 4s, p. 1343∿1353 (1979).

4) M. Dalle-Donne, Int. J. Heat Mass Transfer, 16, p. 787∿809 (1973).

FLUID	He gas
PRESSURE	3 kg/cm^2 G
TEMPERATURE	1000 °C
FLOW RATE	30 g/s
PURIFER	Tl absorber bed

ANNULAR HEAT TRASFER TEST SECTION

PRE-COOLER

COOLER

STORAGE TANK

LIQUID NITROGEN COOLER

PURIFIER COOLER

FLOW CONTROL VALVE

COMPRESSOR

AFTER COOLER

FLOW METERS

FILTER

SURGE TANK
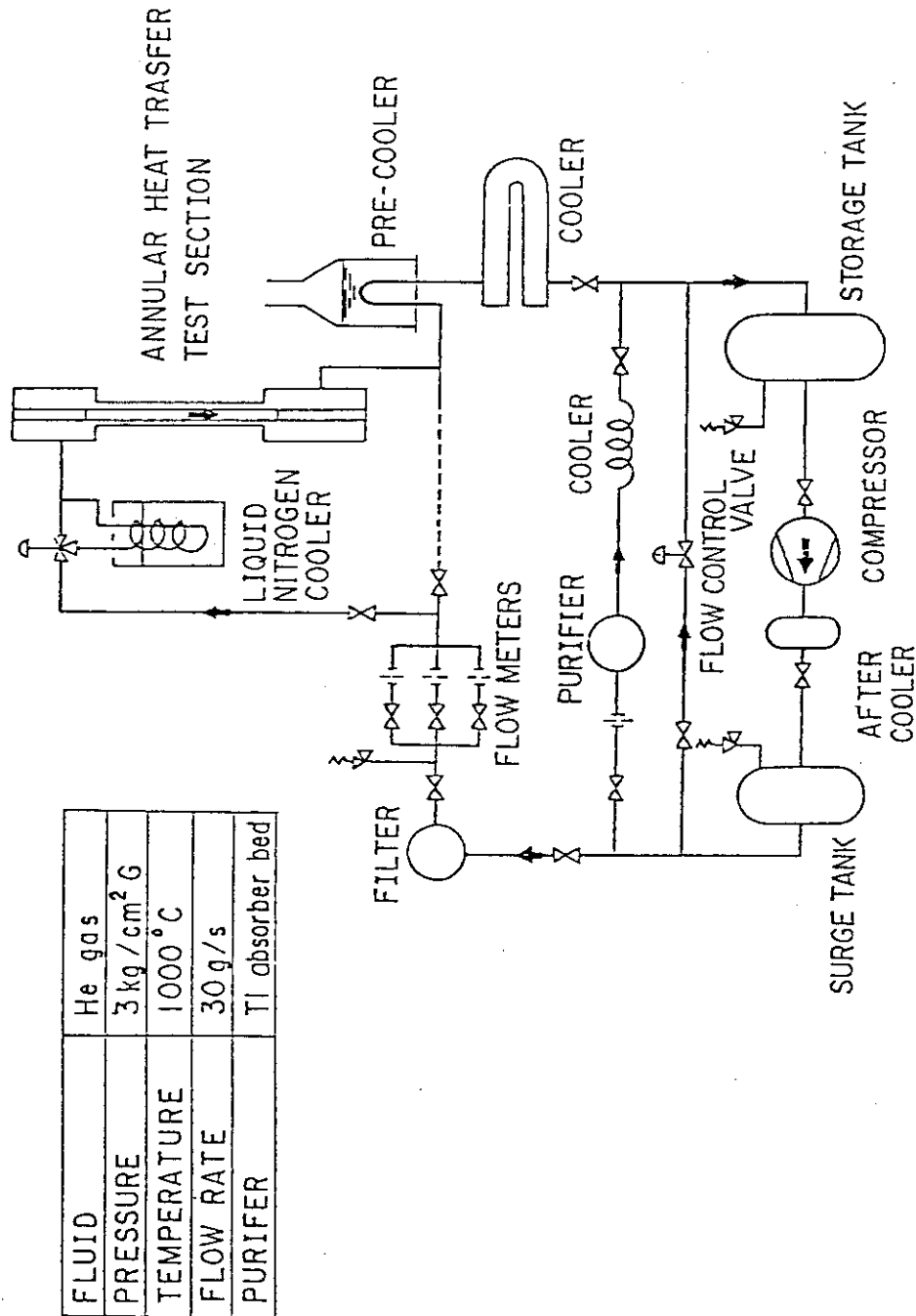
Fig. 3.1   Flow Diagram and Specification of a Small-Scale Helium Gas Loop (SGL)
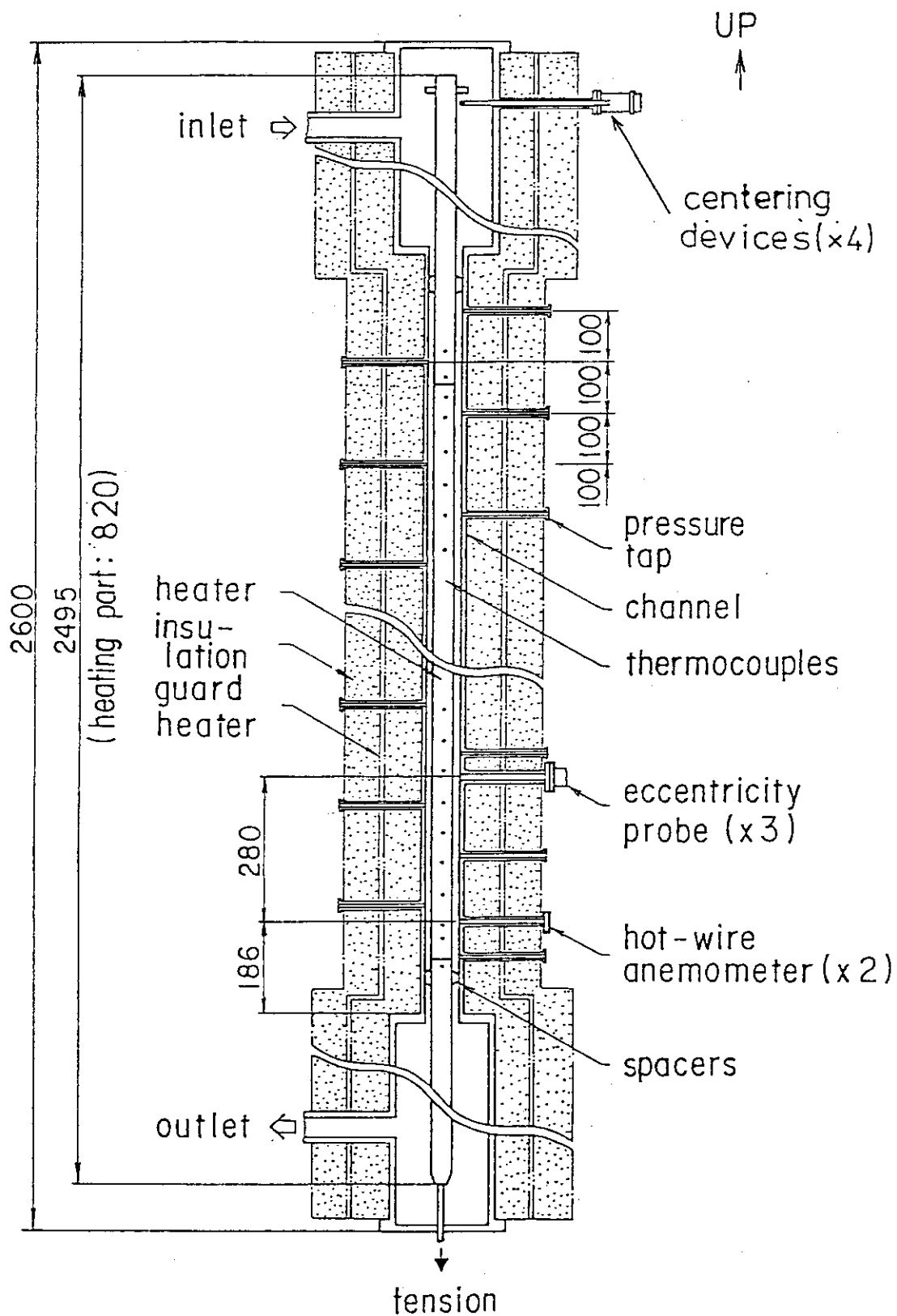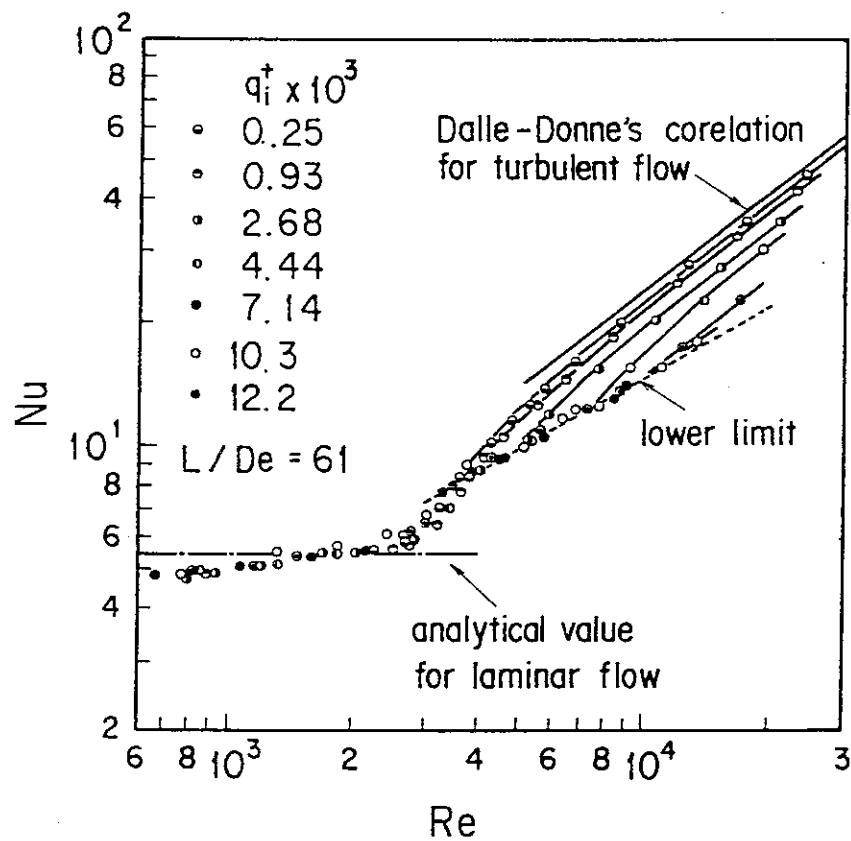
Fig.3.2　An Annular Heat Transfer Test Section

Fig.3.3   An Example of Heat Transfer Characteristics

(34 mm-diameter Heater)
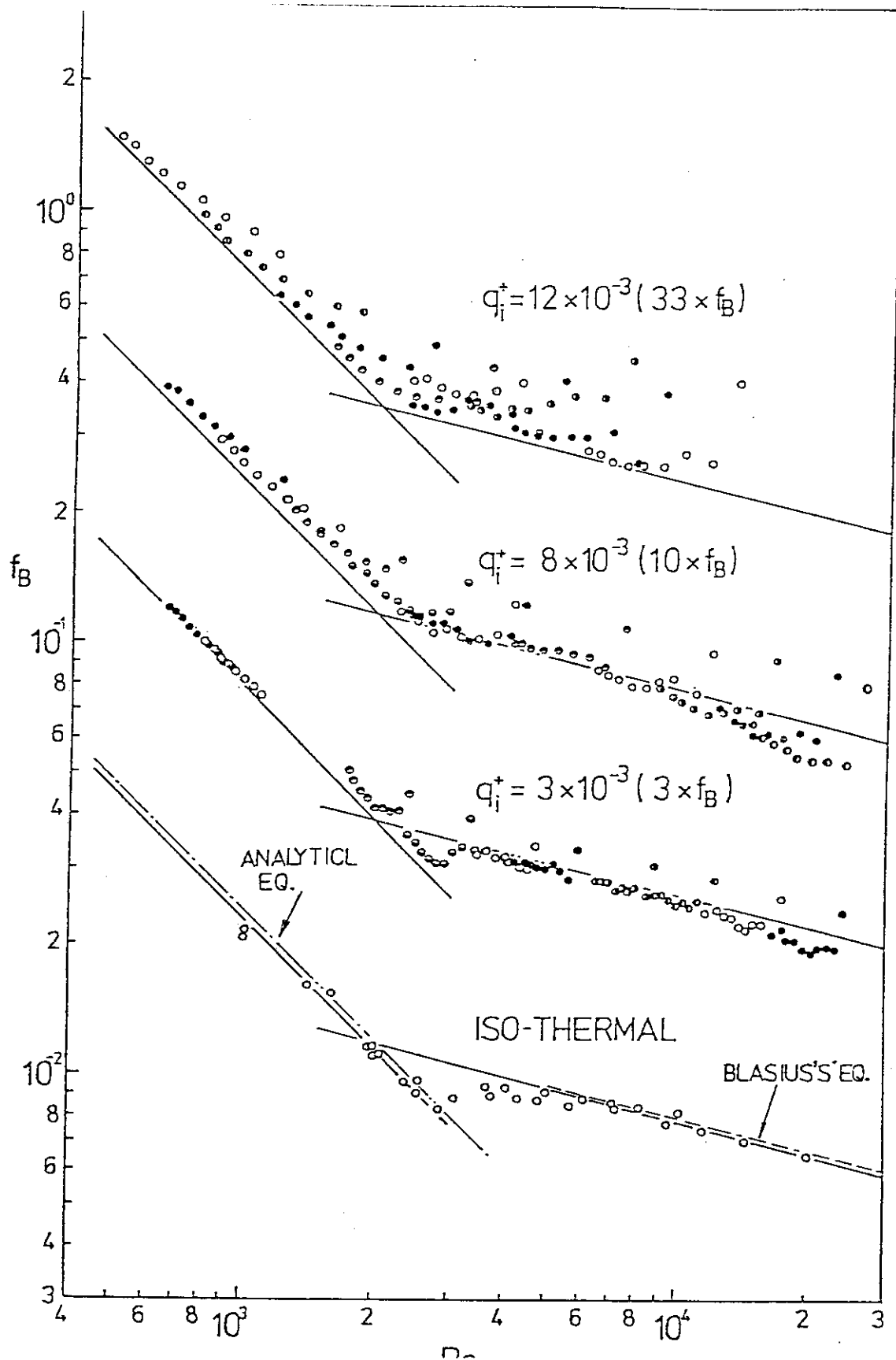
Fig.3.4　Relationship between Friction Factors and Reynolds Numbers
(34 mm-diameter Heater)

3.2 Heat Transfer around Spacer-Ribs on Fuel Rod by Temperature Vizualization Method

H. Akino, K. Suzuki and S. Nakauchi[*]

The experiment on heat transfer and pressure drop of smooth annular channels, presented in the previous section 3.1, has offered the basic data essential to the thermal design of VHTR core with block type fuel elements. On the other hand, there are spacer-ribs and gaps between fuel rods in the annular channels of the actual fuel element.

These abrupt changes of channel shape disturb coolant flow, and may bring about some increase and local distribution of heat transfer, some increase in pressure drop and some difference of flow charateristics in the transitional region.

A performance test is now under preparation to evaluate the effects of the existence of spacer-ribs and gaps, using electrical heaters which simulate the actual fuel rods.

Prior to that experiment, a simple experiment was carried out to study the main feature of the effect of spacer-rib on heat transfer.

A marked point of this experiment was the application of thermo-sensitive liquid crystal to transform the surface temperature distribution around spacer-ribs into color distribution, so that one could easily and efficiently recognize the pattern of the temperature distribution.

Annular coolant channel was simulated by a rectangular duct with 10 mm in height, 200 mm in width and 1100 mm in length. Lower wall was heated by a thin stainless steel foil(0.05 mm×200 mm×400 mm) adhered on the surface. Thermo-sensitive liquid crystal film was covered on the heater surface. Various shapes of spacer-rib models were placed on the liquid crystal film. The characteristic of the liquid crystal film was examined by a calibration test. The sensitivity range was from 28 to 36°C, nine colors were observed and the accuracy of temperature measurement was within 1°C. Conditioned air flow was led into the test channel and electrical current was supplied to the foil heater. After the temperature reached steady state, the color distribution was recorded by a color photograph.

Figure 3.5 shows the isotherms surrounding a spacer-rib of rectangular shape at various Reynolds numbers. Around the leading end, tem-

---

perature was low and heat transfer was enhanced by about 2 times greater
than uninfluenced zone. The width of the colored pattern decreased as
Reynolds number increased, but the pattern did not change. The pattern
suggests the existence of the Hose-shoe vortex (or Necklace vortex).
On the other hand, just downstream of the trailing end, high temperature
zone was observed and heat transfer was deteriorated. The length of
this zone increased as Reynolds number decreased. In this region,
there may be stagnant flow or confined vorteces. In the further down-
stream, slightly low temperature zone was observed. This region may
be swept by the wake.

The patterns of temperature distribution were found to be very
sensitive to the leading and trailing ends of a spacer. Therefore, if
the shape of a spacer-rib is chosen properly, it is possible to obtain
an effective smooth temperature distribution so as to avoid unfavorable
thermal stress.

Hereafter, the flow structure will be studied by a flow vizualiza-
tion technique to understand the temperature pattern and the experimental
technique should be improved to apply it to a complex configuration,
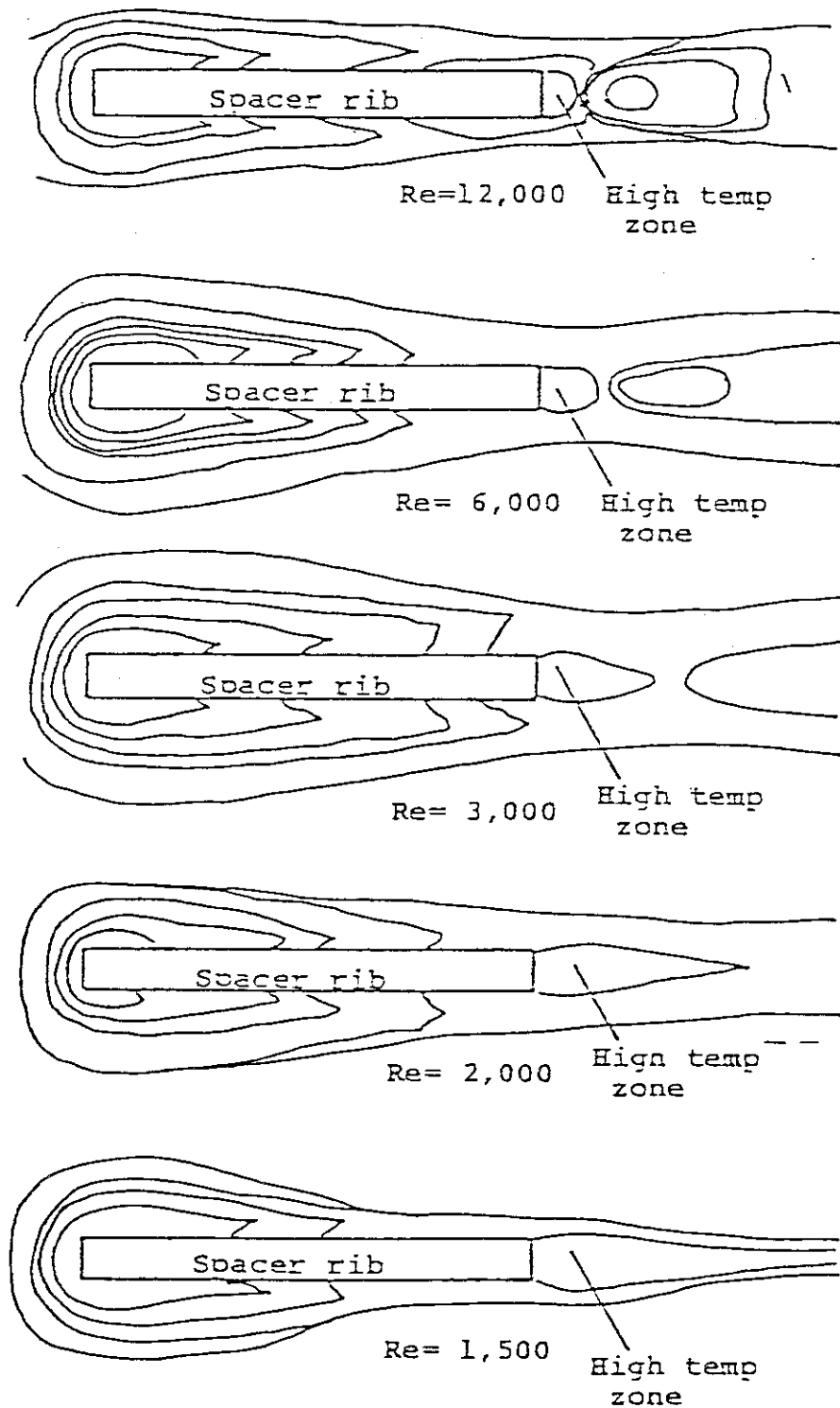such as a fuel rod.

Fig.3.5   Isotherms Around a Spacer-rib Model with Rectangular Cross Section

3.3 Laminarization with Acceleration in Converging Channels

Y. Shiina and K. Fujimura

Introduction

Transition from turbulent to laminar flow occurs in a channel with large temperature variation, although Reynolds number is larger than its critical value. This is mainly due to acceleration of flow induced by fluid expansion. Accordingly, laminarization phenomenon caused by large temperature variation can be simulated by flow acceleration of isothermal flow in a converging channel. In the present study, the recovery of turbulence intensities of laminarized flow in a channel without adding heat was examined for a parallel and converging channel flow.

The fluctuations of velocity components in flow direction u' and transverse direction v' were measured by a constant-temperature hot-wire anemometer.

Experimental apparatus and results

Figure 3.6 shows a configuration of experimental appartus. The apparatus consisted of three parts, upstream parallel channel of 1500 mm in length, converging channel of 500 mm in length and downstream parallel channel of 1000 mm in length. The channel width is 30 mm in the upstream parallel channel, and variable in the downstream parallel channel. A constant-temperature hot-wire anemometer was inserted in the test channel at positions from 1 to 7, as shown in Fig. 3.6. The range of Reynolds numbers in this experiment was from 5500 to 15000 based on a hydlauric diameter. Half-taper angles of the converging channels were 0.015 and 0.004 in radian.

The measurement of the dimensionless turbulence intensities in the converging channel normalized by the friciton velocity showed that the accelerated velocity fluctuation u' diminished at first when equilibrium condition in turbulence between generation and dissipation can hardly be maintained, and then v' diminished. On the other hand, these fluctuations were recovered in the downstream parallel channel. Particularly the fluctuation v' was recovered to the same level as u'. Figure 3.7 shows dimensionless Reynolds stress for the case of Re=10000 and α=0.015. Dimensionless Reynolds stress diminishes in the converging channel. In the downstream parallel channel, however, dimensionless Reynolds stress is recovered in the vicinity of the wall and the region

of recovery is extended from the wall to the channel center as the flow goes downstream.

Figure 3.8 shows the velocity fluctuations near the wall for the case of Re=8000 and α=0.015. The top curve in each figure is the trace of u', and the bottom curve v'. The differences in the velocity fluctuation between position 1 and position 2 or 3 was not appreciable. Velocity fluctuations decrease at position 4 and the new fluctuations with high frequency and large amplitude appear intermittently as shown in the trace of position 6. These fluctuations appear more frequently at position 7. When measuring postion is fixed, appearing frequency of the fluctuation described above increases with Reynolds number. It is considered that this fluctuation plays an important role on the recovery process of turbulence in the downstream parallel channel.
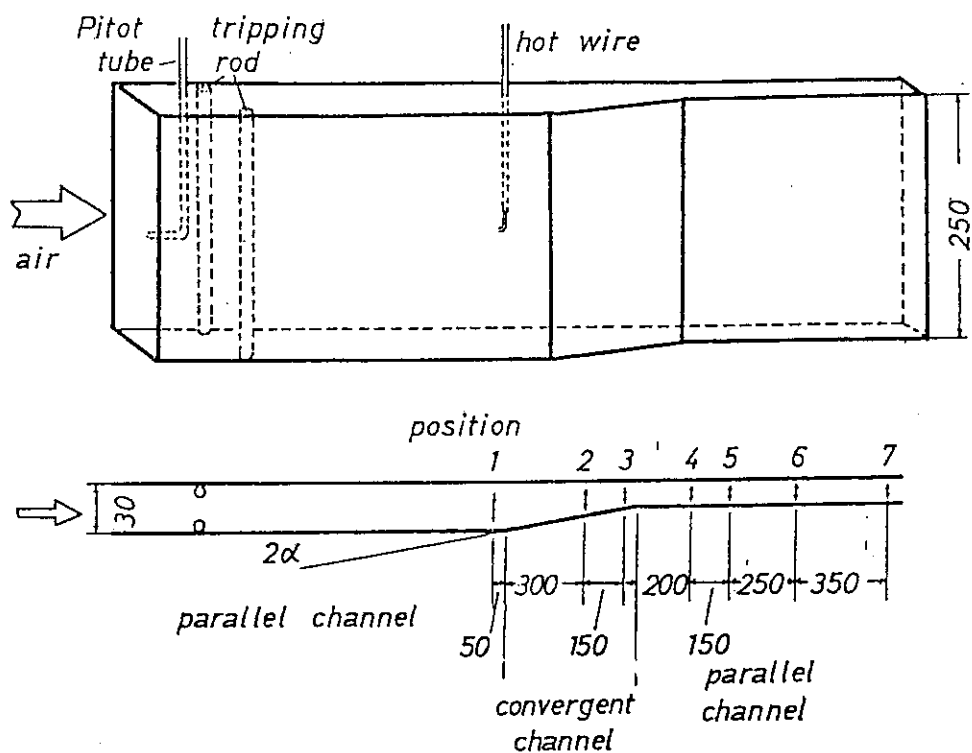
Fig.3.6　A Test Section
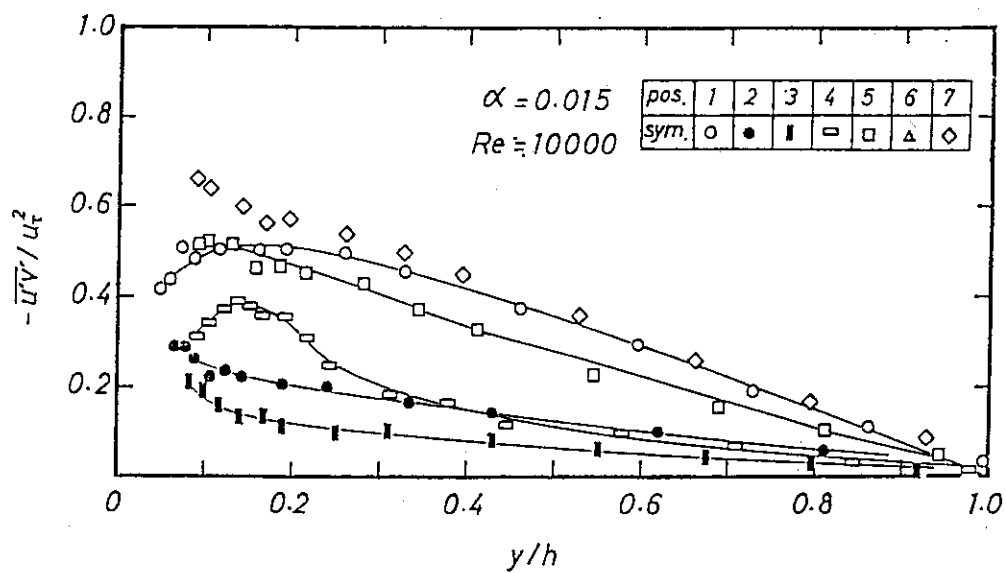
Fig.3.7　Distribution of Dimensionless Reynolds Stress; Re=10000, α=0.015
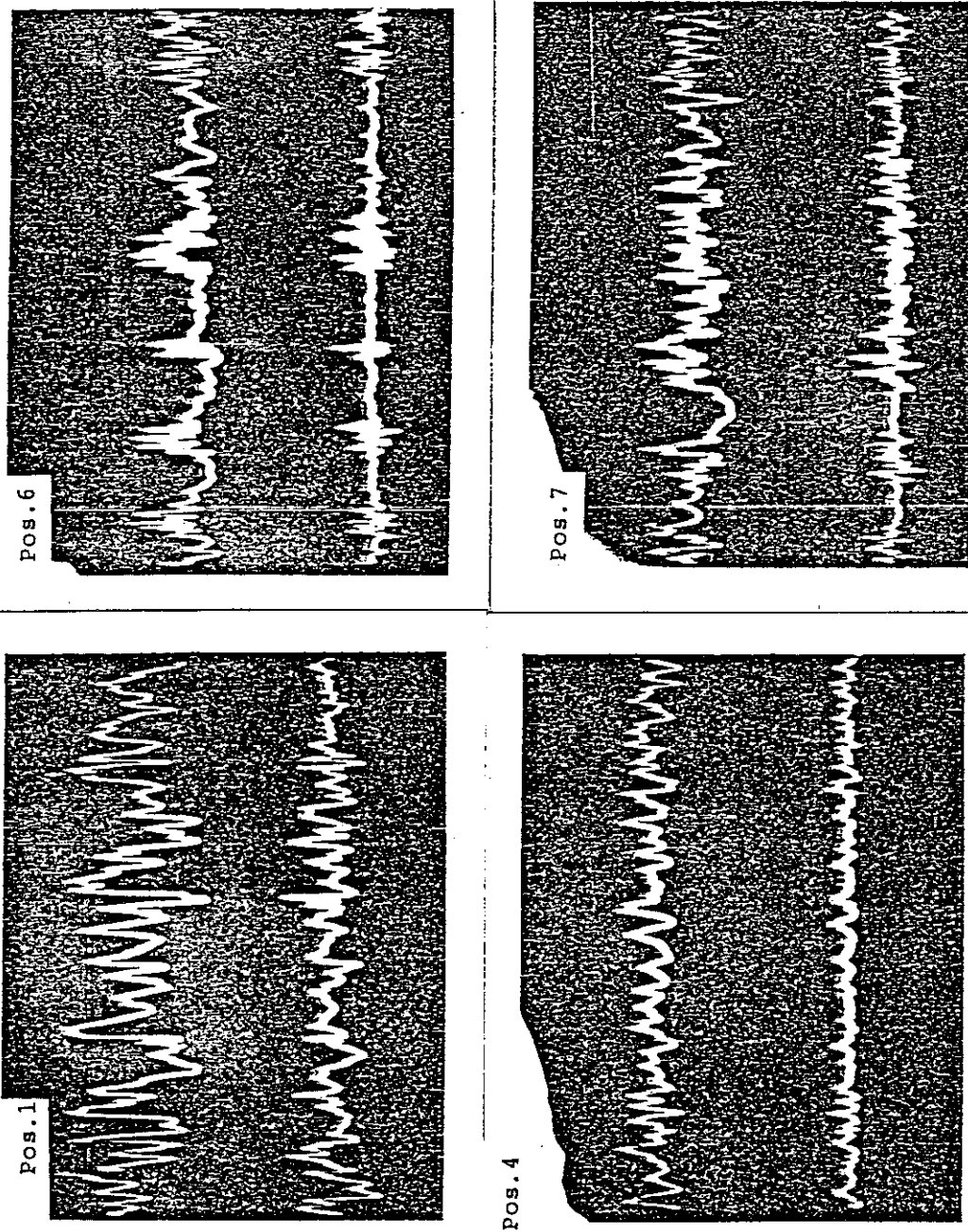
Fig.3.8 Traces of Velocity Fluctuations; Upper Curve of Each Figure
is a Trace of u', Lower Curve a Trace of v'

3.4 Experiment on Laminarization of Strongly Heated Gas Flow in a Circular Tube

M. Ogawa, H. Kawamura, T. Takizuka and N. Akino

Introduction

Bankston[1], McEligot et al.[2], Coon et al.[3] and Mori et al.[4] examined that heat transfer coefficients in strongly heated gas flow decreased down to the laminar prediction for a circular tube even though the bulk Reynolds number was still higher that the normal transition Reynolds number for isothermal flow. This phenomenon is called laminarization. Heated gas is accelerated by the increasing velocity due to the decrease of density. Since physical properties depend on temperature, the properties at the center of flow are different from those near the wall. These effects appear to be a cause of the so-called laminarization. It is not yet clarified, however, in the case where the flow shifts reversely from the turbulent to the laminar. So it is necessary to observe the regimes of strongly heated gas flow in a circular tube and define qualitatively and quantatively a criterion for initiation and termination of laminarization.

In the present study a hot-wire anemometer and a miniaturized thermocouple were used to examine the flow regimes. The criterion was provided as the relation between inlet Reynolds number Re_i and inlet dimensionless average heat flux parameter $\bar{q}^+_i$ $(=\bar{q}_w/G \cdot C_p \cdot T_i)$.

Experimental apparatus and methods

The experiments were conducted with a forced convection helium gas loop. The test section is constructed from a stainless steel tube with an inside diameter of 4 mm and a wall thickness of 1 mm. A 109 mm (27.3 diameter length) adiabatic entry section precedes a 630 mm (158 diameter length) heating section as shown in Fig. 3.9. The test section is surrounded by gold-plated glass tubes in order to reduce radiation heat loss. The vacuum jacket surrounding the test section is maintained at a pressure of less than 10^{-3} torr. The vertical circular tube is resistively heated with alternating current of constant voltage. To calculate the local wall heat flux, the heat losses by radiation and heat conduction in the axial direction of the tube wall were considered.

The hot-wire anemometer (H.W.) and miniaturized thermocouple (T.C.) shown in Fig. 3.10 are inserted at 150 diameter location from top end of the heating section.

Turbulent fluctuations in the heated gas flow were observed by using H.W., and gas temperature at the center of flow by using T.C..

Heat transfer experiments were performed in the case of Re_i=1340-40000, $\bar{q}_i^+ \leq 7.2\times10^{-3}$ $T_i \geq 98$ K, $T_w/T_b \leq 3.36$ and $P=1.45\sim4.25\times10^5$Pa. Re_i was fixed and $\bar{q}_i^+$ was gradually increased.

Experimental results and discussions

1) Isothermal experiments

The velosity fluctuations measured by H.W. are shown in Fig. 3.11, and this served a great help of understanding the transition range of isothermal flow. The value of γ is called an intermittency factor and denotes the fraction of time in which the flow is turbulent. The intermittency factor equals to unity in the turbulent flow, and zero in the laminar flow. The value of f denotes an occurrence frequency of a pair of turbulent and laminar parts. The oscillograms of velocity are shown in the top of Fig. 3.11. When the flow rate is increased in the laminar region, the turbulent fluctuation starts to appear at Reynolds number of 2800 and the flow is almost turbulent at Reynolds numbers greater than 3140.

2) Experiments on laminarization

The axial variations of local heat transfer coefficients are shown in Fig. 3.12. The inlet Reynolds number was fixed at Re_i=10000 and $\bar{q}_i^+$ was increased stepwise. Same signs in the figure correspond to the axial variation (eleven points from 10.4 to 129 diameter location) of Stanton numbers in a run of a specified heat flux. The arrows show the flow direction. Figures 3.13 and 3.14 show respectively the oscillograms of T.C. and H.W. corresponding to each value of $\bar{q}_i^+$ in Fig. 3.12. The top of the H.W. signal in Fig. 3.14 is the one obtained by the constant-temperature method, and the bottom is the signal passed through a high pass filter of 1 kHz.

In the case of 1:$\bar{q}_i^+$=2.96×10^{-3} and 2:$\bar{q}_i^+$=4.18×10^{-3} in Fig. 3.12-3.14, all the data suggest that the flow is turbulent. In the case of 3:$\bar{q}_i^+$=4.62× 10^{-3}, a spine in the signal of T.C. and a part without turbulent fluctuations in the signal of H.W. are observed. It is seen that the flow is of an intermittent character associated with an isothermal transitional flow because of high heat flux. Gas temperature at the center in the laminar part of the intermittent flow is lower that in the turbulent part because the mixing is less prominent in the laminar part than in the turbulent part. Consequently, the spine appears in the signal of T.C.,

Local heat transfer coefficients of case 3 shown in Fig. 3.12 decrease once toward the laminar prediction and return to the turbulent prediction.

In the case of $4: \bar{q}_i^+ = 4.78 \times 10^{-3}$, downstream wall temperature changes slowly up and down. This condition seems to be just on the border whether the laminar part expands axially or not. More heat being added, in the case of $5: \bar{q}_i^+ = 4.85 \times 10^{-3}$, the laminar part appears more frequently and local heat transfer coefficients go on decreasing to the laminar prediciton. In the case of $8: \bar{q}_i^+ = 5.72 \times 10^{-3}$, the signals corresponding to turbulent parts almost disappear and laminarization has been terminated. In the H.W. oscillogram some fluctuations are still observed. The wave profile, however, is different from that of turbulent fluctuations. It seems to be a trace of upstream turbulent flow.

3) The criteria for initiation and termination of laminarization

Figure 3.15 shows the relation between Re_i and $\bar{q}_i^+$ when laminarization initiates and terminates. In the present study, initiation of laminarization is defined as a point where the intermittency starts to be observed and termination as a point where the signal corresponding to turbulent parts disappears. The critria by McEligot et al[2]. and Coon et al[3]. do not agree with the present study at high Reynolds numbers. In the inlet Reynolds numbers higher than 10000, laminarization occurs at the heat flux lower than their predictions. The following equations were derived for the criteria from measured data approximated by means of the least square method.

Initiation of laminarization
$$\bar{q}_i^+ = 4.94 \times 10^{-3} \cdot Re_i^{0.05} \{ 1 - (Re_{tr}/Re_i)^{0.75} \} \tag{1}$$
$$Re_{tr} = 3140, \quad 4500 \leq Re_i \leq 40000$$

Termination of laminarization
$$\bar{q}_i^+ = 5.87 \times 10^{-3} \cdot Re_i^{0.05} \{ 1 - (Re_{tr}/Re_i)^{0.75} \} \tag{2}$$
$$Re_{tr} = 2800, \quad 4500 \leq Re_i \leq 11000$$

References

1) Bankston C.A.: J. of Heat Transfer, 92, 569 (1970).

2) McEligot D.M. et al.: Int. J. Heat & Mass Transfer, 13-2, 431 (1970).

3) Coon C.W. et al.: Trans. ASME, Ser. C, 92-3, 506 (1970).

4) Mori Y. & Watanabe K.: Trans. JSME, Ser. B, 45-397, 1343 (1979).

5) Coon C.W.: Ph.D. Thesis, The University of Arizona (1968).

6) Perkins H.C. & Worsoe-Schmidt P.M.: Tech. Report SU 247-7, Mechanical
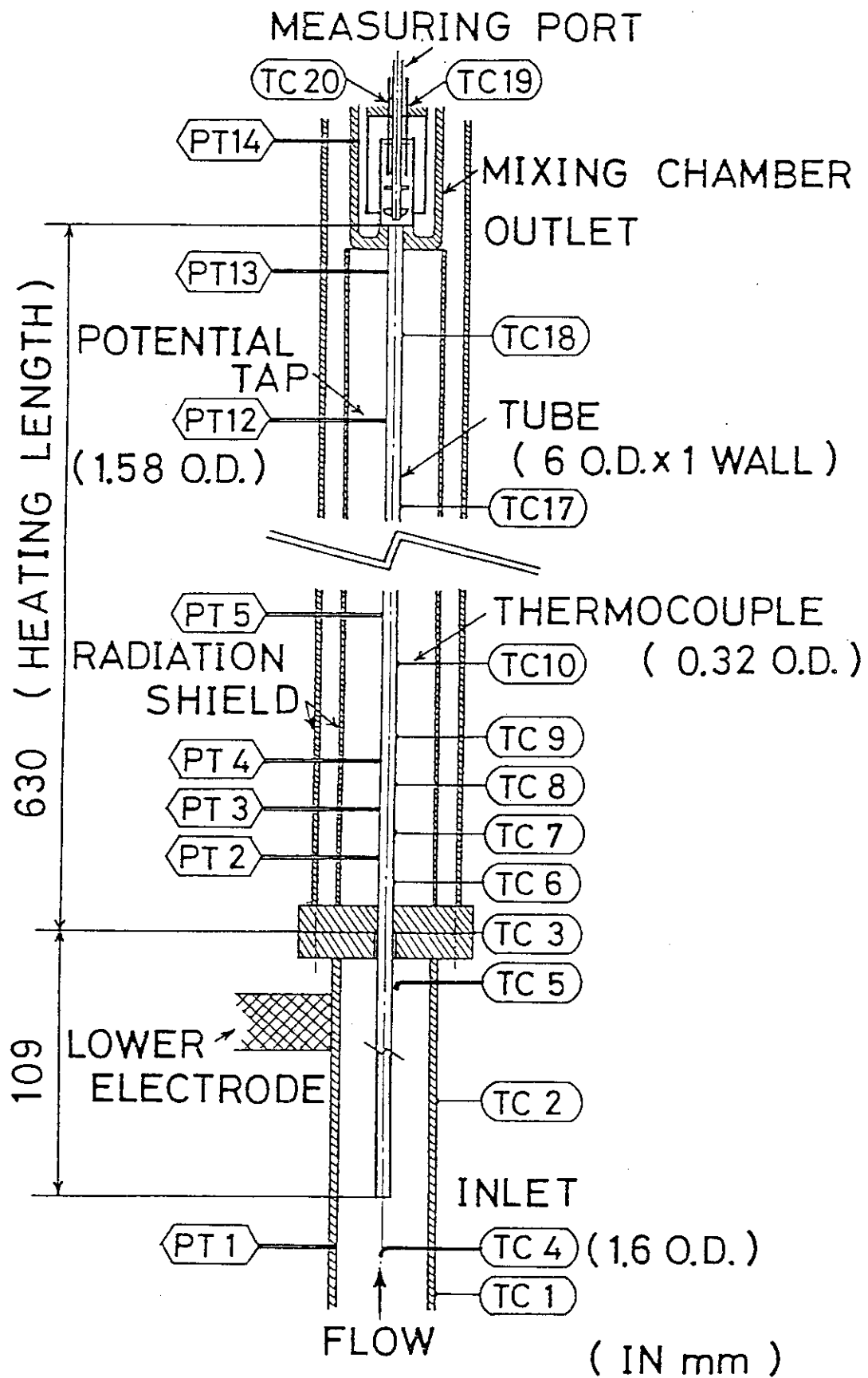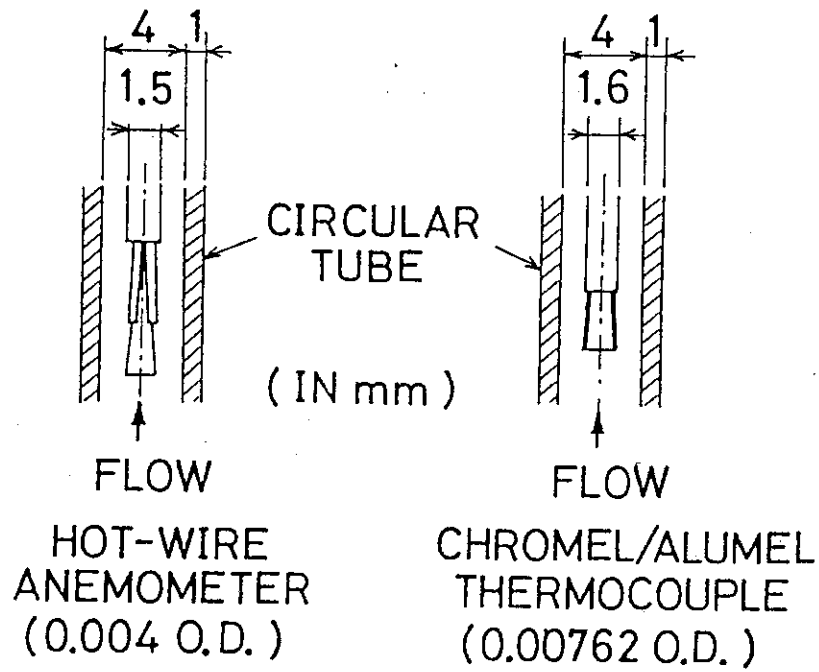   Engineering Dept., Stanford University (1964).

Fig.3.9　A Circular Heat Transfer Test Section

Fig.3.10   Probes for Measuring Turbulent Fluctuation and Gas Temperature
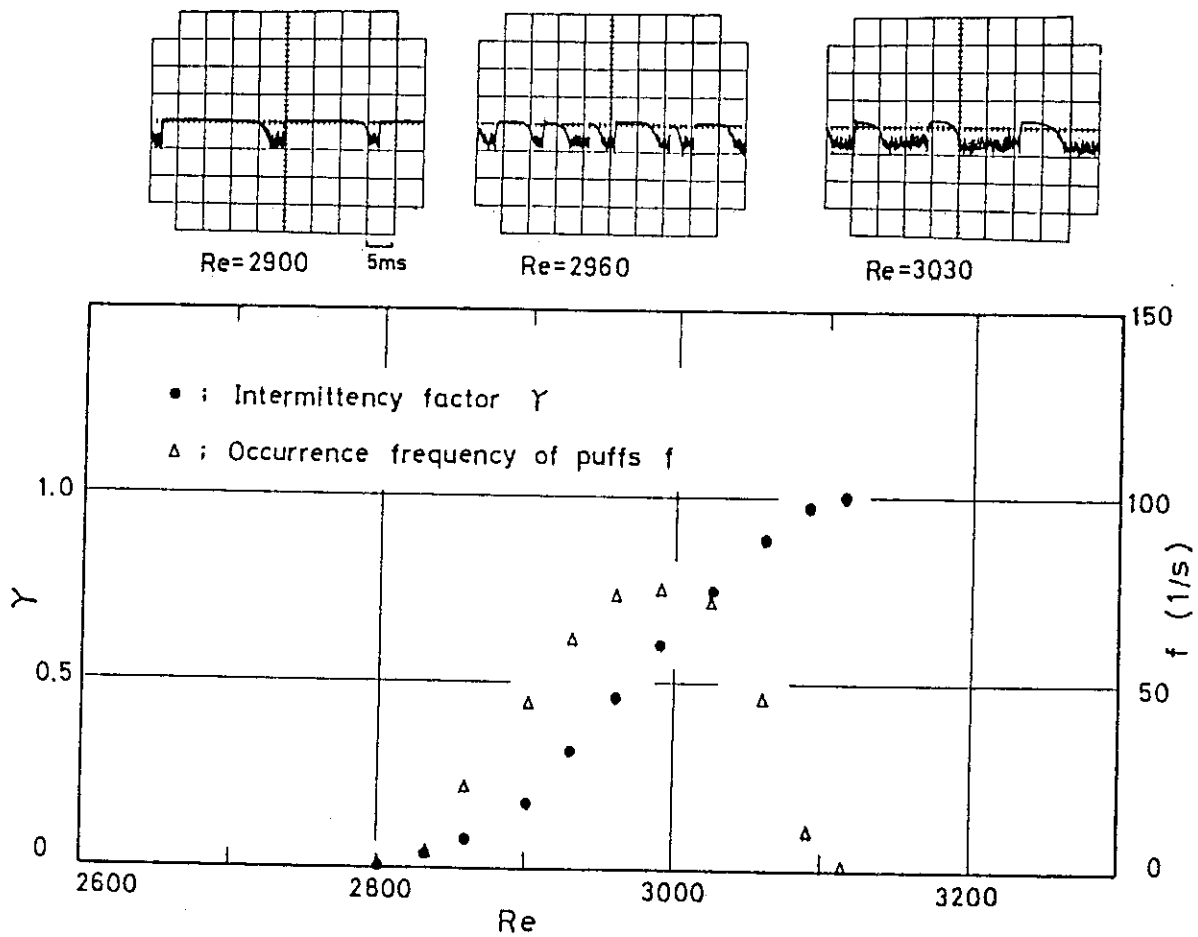
Fig.3.11   Flow Characteristics of Transition Region

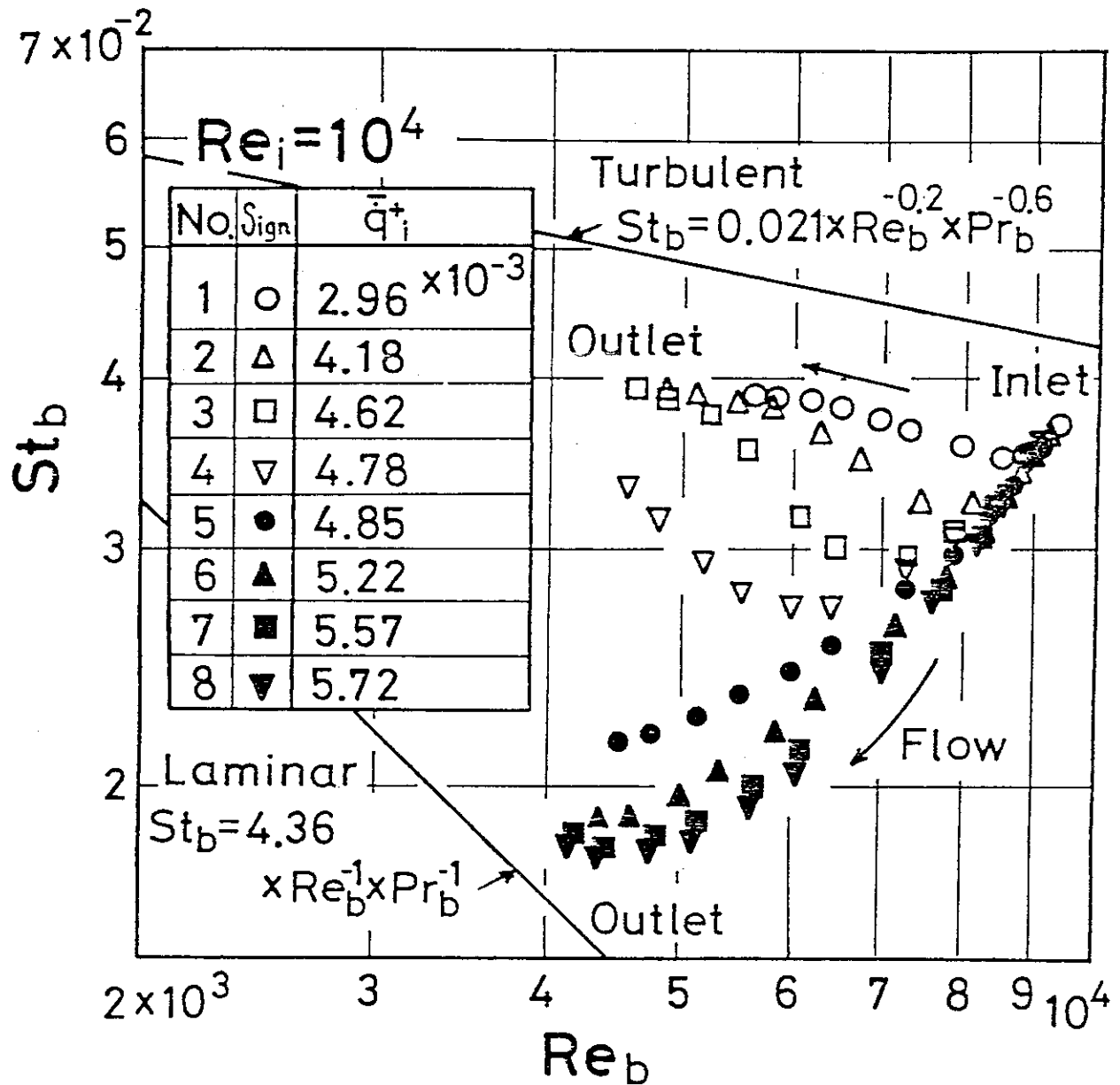Upper Figures: Oscilloscope Traces of Hot-wire Anemometer

Fig.3.12 Relation between Stanton Numbers and Reynolds Numbers in a Circular
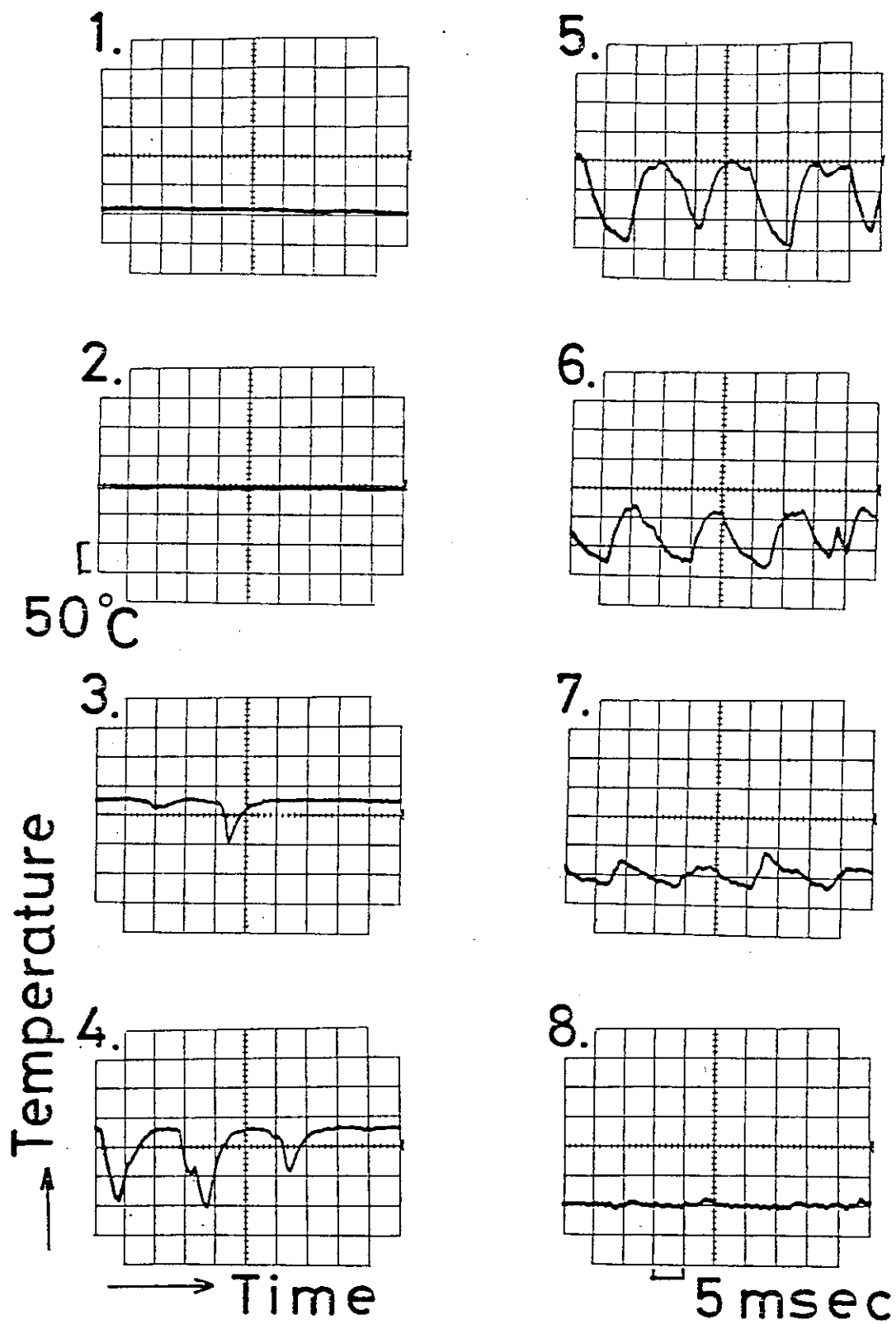Tube When the Flow is Strongly Heated

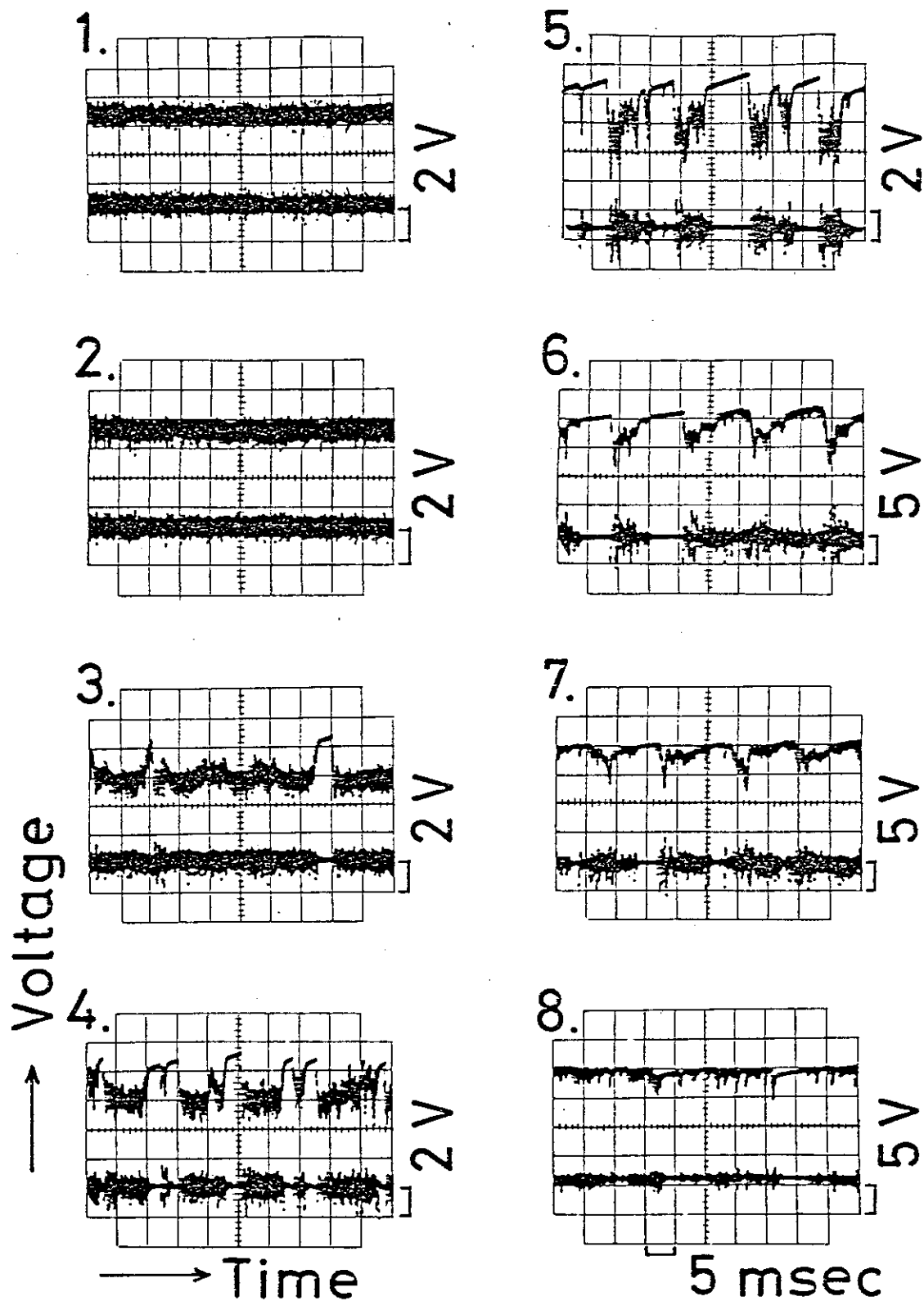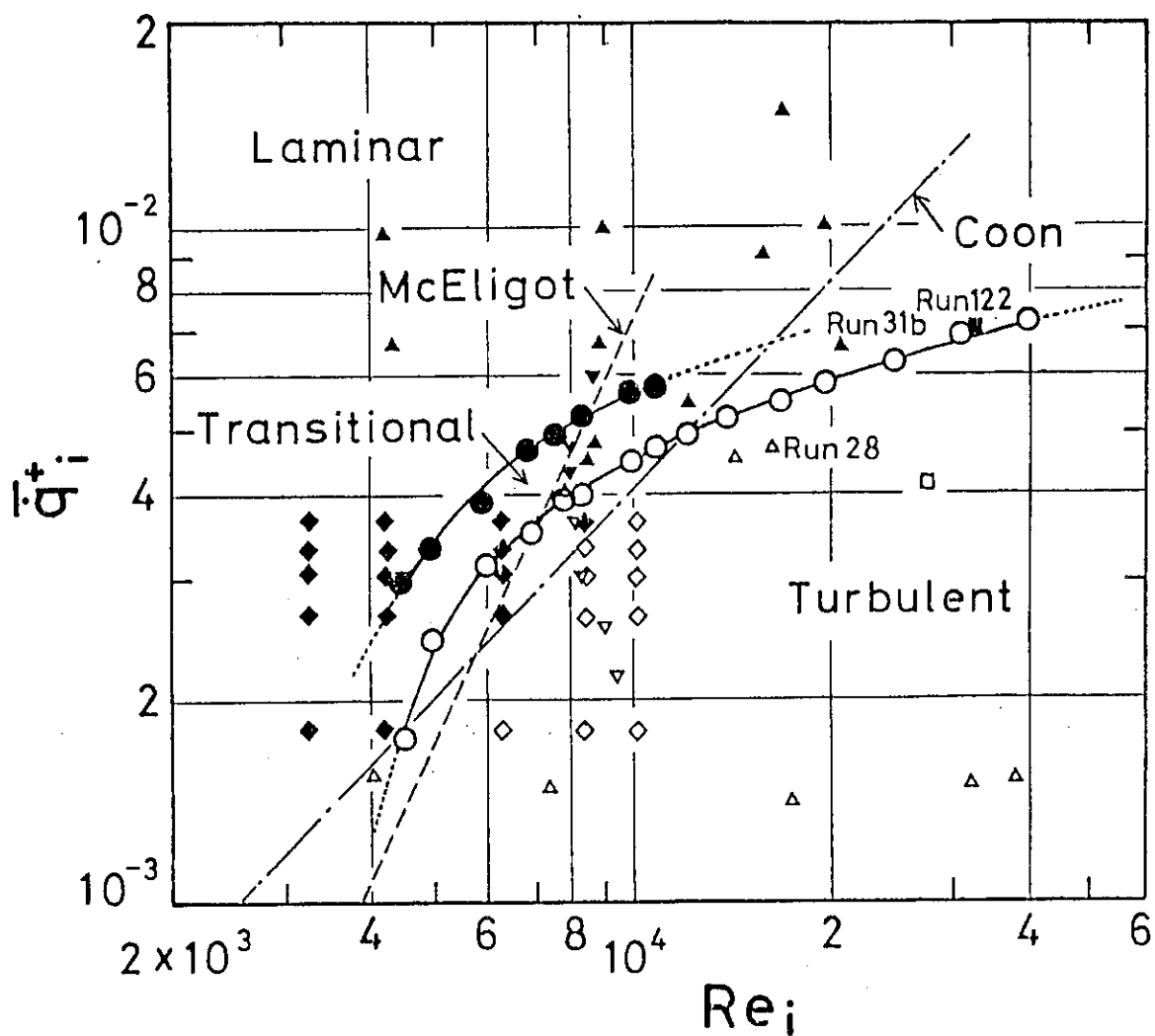Fig.3.13 Oscilloscope Traces of Miniaturized Thermocouple

Fig.3.14   Oscilloscope Traces of Hot—wire Anemometer

Fig.3.15 Flow Regime of Heated Gas in a Circular Tube

3.5 Experiment on Heat Transfer Augumentation

M. Hishida, M. Ouchi and H. Kitagawa

Ribbed surface is one of the promissing methods to improve heat transfer performance of fuel rods and heat exchangers of VHTR. It increases heat transfer rate by a factor of more than 2 and is possible to prevent "laminarization" by inducing turbulence in coolant flow.

Although many studies have been published on heat transfer of turbulence promoter or ribbed surface in relation to fuel rods of AGR and GCFR, few studies were found on local heat transfer coefficient and heat transfer performance in low Reynolds number range $(Re \leq 10^4)$.

The objectives of the present study are:

(1) to make clear of local heat transfer coefficient of ribbed surface including rib surface itself.

(2) to make clear of heat transfer performance of ribbed surface in low Reynolds number range of $Re \leq 10^4$, in which the reactor core of VHTR is to be designed.

Figure 3.16 shows the increased ratio of the local Nusselt number, Nu_r/Nu_s. Nu_r is Nusselt number of the ribbed surface, and Nu_s is that of a smooth surface. Nu_s is calculated from the equation: $Nu_s = 0.018 \cdot Re^{0.8} \cdot Pr^{0.4}$. The increased ratio of Nusselt number on the base surface where the ribs are attached is around 2 to 5. The local maximum value appears at $x/h_p = 3 \sim 4$, depending on the Reynolds number. Where x and h_p denote respectively a coordinate along flow direction and a height of the rib. An interesting point is that the local Nusselt number Nu_r is larger than Nu_s even in the vicinity of the back face of the rib. This enhanced heat transfer is attributed to the vortexes which are generated behind the rib and are flowing downstream with high frequency. The ratio, Nu_r/Nu_s, on the front face of the rib is much higher than that on the base surface. It increases towards the top of the rib, and becomes maximum at the front top of the rib. The maximum value is around 4 to 6. Nu_r/Nu_s on the back face of the rib is almost even and its value is from 2 to 4.

On the top of the rib, the distribution of local Nusselt numbers changes with Reynolds number, while, on the rest parts of the ribbed surface, Nu_f distribution is similar for various Reynolds numbers. Local Nusselt number on the top of the rib increases downstream when

Reynolds number is high, which is related to the separation of flow at
the front top of the rib. On the contrary, local Nusselt number decreases
downstream when Reynolds number is low, which indicates development of a
boundary layer from the front top of the rib.

The ribbed surface was devided into five local zones: zone 1 - front
face of a rib, zone 2 - top face of a rib, zone 3 - back face of a rib,
zone 4 - base surface before the reattachment point of flow and zone
5 - base surface after the reattachment point. The Nusselt number
averaged locally for each zone was obtained and shown in Fig. 3.17.
The local average Nusselt number is highest on the front face of the
rib, and is second highest on the top face of the rib. The local average
Nusselt numbers at zones 3 , 4 , and 5 , are nearly the same.
This shows that the influence on heat transfer from the rib itself is
not small.

Figure 3.18 shows overall average Nusselt number, which is the mean
value of the whole zone. The signs (0,●) indicate the average Nusselt
number of a ribbed surface, while, the signs (Δ,▲) designate that of an
opposite smooth surface. The average Nusselt number of the ribbed surface
increases in proportion to around 0.2-th power of Reynolds number when
Reynolds number is below 5000, and it increases in proportion to about
0.7-th power of Reynolds number when Reynolds number is above 5000.
This causes the higher ratio, Nu_r/Nu_s in the low Reynolds number range,
compared with the one in the high Reynolds number range. This indicates
that a ribbed surface can be used effectively in low Reynolds number range.
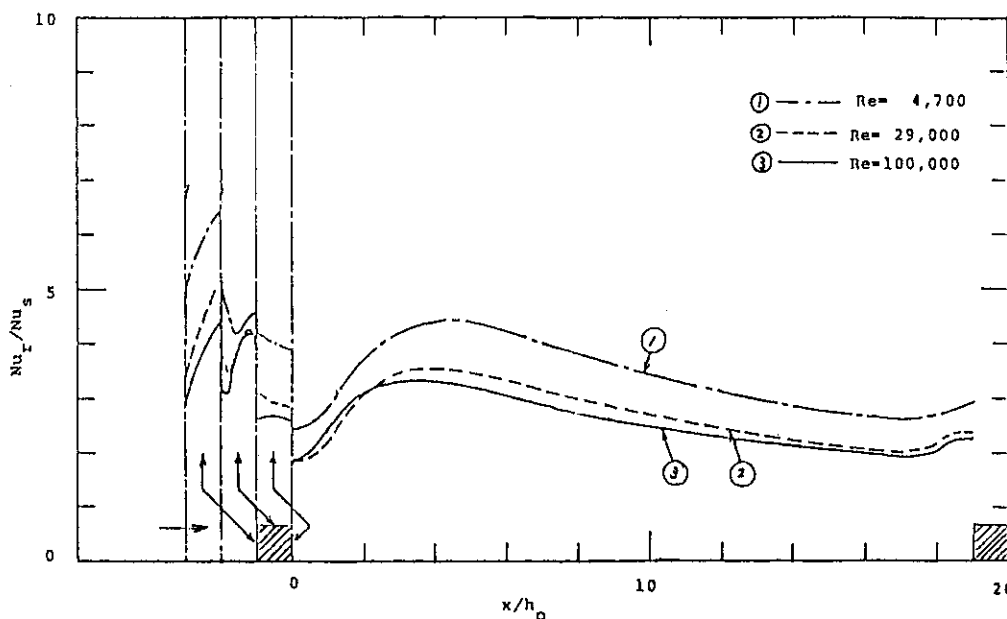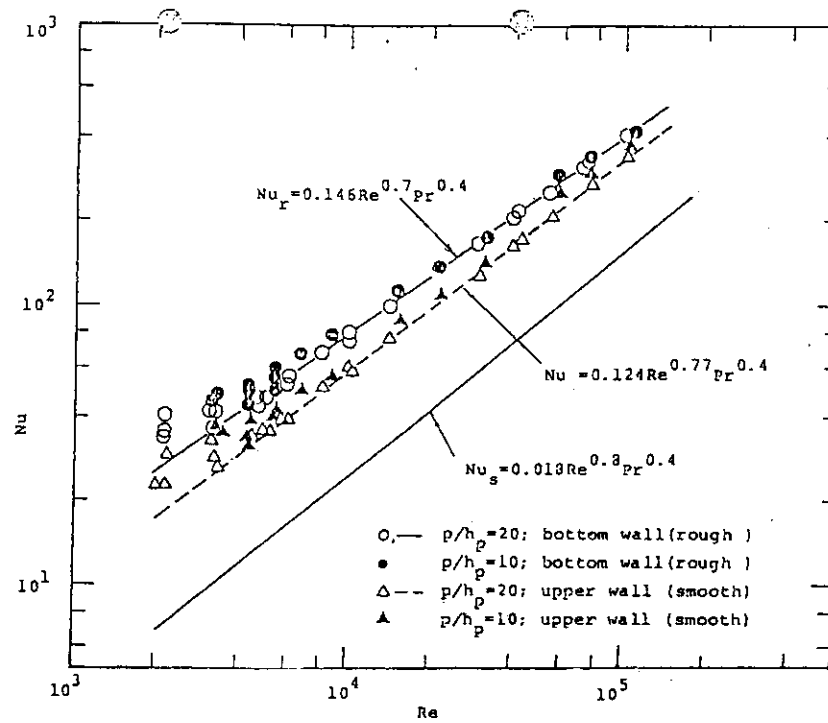

Fig. 3.16 Nu_r/Nu_s Distribution
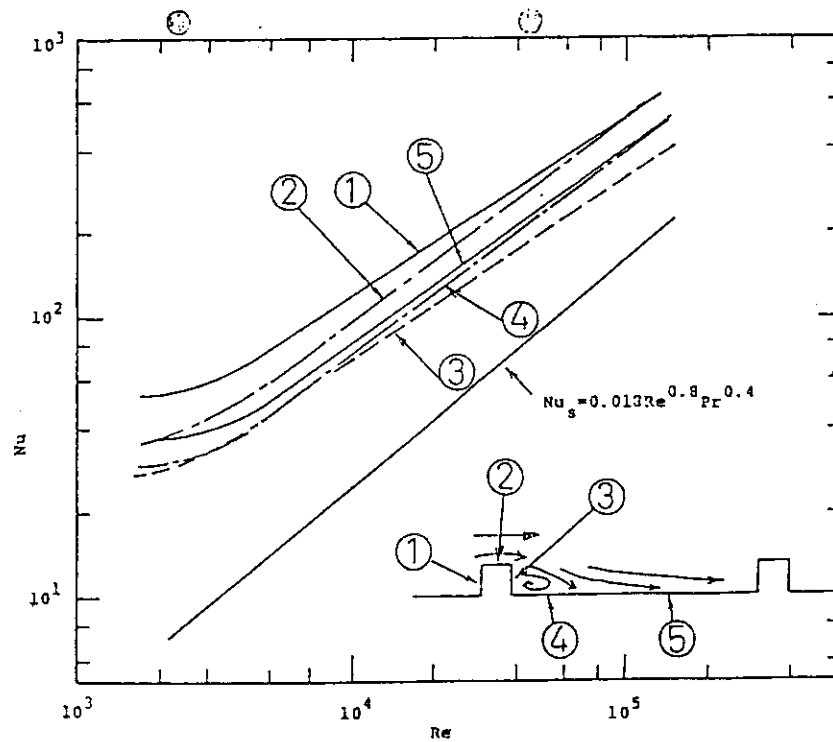
Fig.3.17　Average Nusselt Number

Fig.3.18　Average Nusselt Number at Various Zone

3.6   On the Transition of Circular Pipe Flow

   K. Fujimura, Y. Shiina and H. Kawamura

When an accident occurs in VHTR core cooling system, coolant-flow
in the reactor core will be reversed by the buoyancy effect; the flow
regime will change from the turbulent to the laminar, then from the
laminar to the turbulent. We have been studied the flow characteristics
in laminar-turbulent transition regime for a circular pipe. This report
describes the process of formation of so-called turbulent slugs.

The experimental apparatus is illustrated in Fig. 3.19. (For the
details, see ref.1.) A smooth pipe of 46.5 mm in diameter was used.
The disturbance was generated by small jets emanating from a hole with
a diameter of 1 mm. The nozzle was located at $\overline{X}/D=0.5$, where $\overline{X}$ is a
distance from the inlet and D is a diameter of the pipe. The distance
from the jet nozzle will be denoted as X.

Throughout this experiment, Reynolds number R was maintained to be
nearly 16300, where $R=<U>D/\nu$, $<U>$ a mean velocity based on volumetric
flow rate and ν a kinematic viscosity. In the absence of disturbance,
the flow field was completely laminar. The jets were produced by a
loudspeaker activated by square wave signals. The leading edge of the
signal caused the membrane of the speaker to contract rapidly and produc-
ed jets.

Streamwise velocity component was measured with a hot-wire probe
on the 6 equi-angular lines at three fixed positions; X/D=1.03, 11.7 and
22.5.

Ensemble-averaged time records of the streamwise velocity are pre-
sented for different radial directions in Fig. 3.20. Thirty-two events
constitute an ensemble. The abscissa in thess figures is time measured
from the leading edge of the square wave signals. The ordinate represents
a streamwise velocity component normalized by the laminar velocity u_0
at the center line of the pipe.

Each trace was recorded by a hot-wire at the different radial
position, the numbers on the right-hand side of each figure indicate
the locations of the sensor, where r denotes a distance in the radial
direction from the center line of the pipe, and r_0 a radius of the pipe.

As X/D increases, turbulent region develops not only in the stream-
wise direction but also in the radial direction (i.e. perpendicular to
the pipe wall). At X/D=1.03, the traces are completely laminar-like

from r/r_0=0.6 to the counter wall. (i.e, $0.6 > r/r_0 > -1.0$) Turbulence is localized near a disturbance injector. At X/D=11.7, the turbulent fluctuation is found in $1 > r/r_0 > 0.17$. In the remainder region, hot-wire traces contain only a fluctuation like one period of sine wave; this is a low wave number fluctuation, which can be distinguished from turbulent fluctuation. A nearly vertical straight line connects the peak points of these low wave-number fluctuations. From this line, the travelling velocity of the peak point in the radial direction is found to be about $0.22 < U >$. At X/D=22.5, the low wave-number fluctuations are localized only near the center line of the pipe and the other part contains the turbulent fluctuations.

In order to show the development of the turbulent region, equi-RMS curves of the streamwise velocity fluctuations are presented in Fig. 3.21. The RMS value was obtained by using a band path filter of 100 Hz-10 kHz, which is typical for turbulent fluctuation. Thus the degree of transition is seen clearly in Fig. 3.21.

Since these figures are based on the measurements along only three lines of A-A, B-B and C-C, the equi-RMS curves drawn are interpolation of the measured values.

For the turbulent region generated from the jet nozzle, the deveolpment rate in the circumferential direction (parallel to the wall) is much greater than the rate in the radial direction (perpendicular to the wall). After being axisymmetrized, the turbulent region develops to the so-called turbulent slug with almost uniform increase of turbulent fluctuation.

One possible feature for the process of the occurrence of slugs in a circular pipe was obtained. For the Blasius flow, it is well understood that, as the result of the higher order instability of the laminar flow, the turbulent spot occurs in the flow field at the final stage of laminar-to-turbulent transition. For a circular pipe flow, however, no such clear understanding of the transition has been obtained; so the above feature of transition is only a possible one. Another feature of transition is also possible at least for the natural transition, in which no artificial jet is introduced.

Reference

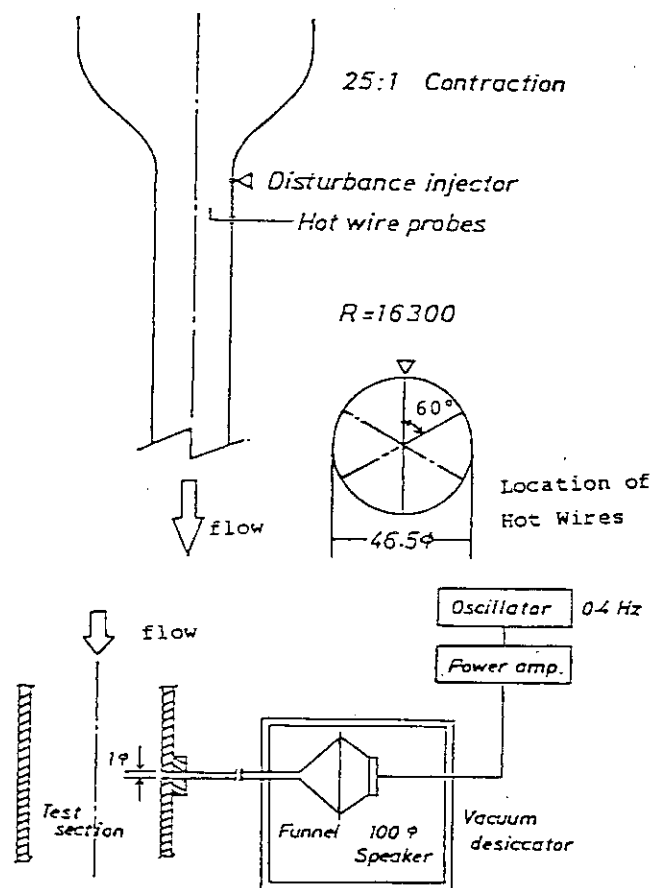1) K. Fujimura et. al.: "Proc. 13th Turbulence Symp." Tokyo Univ.
146 (1981) (in Japanese).
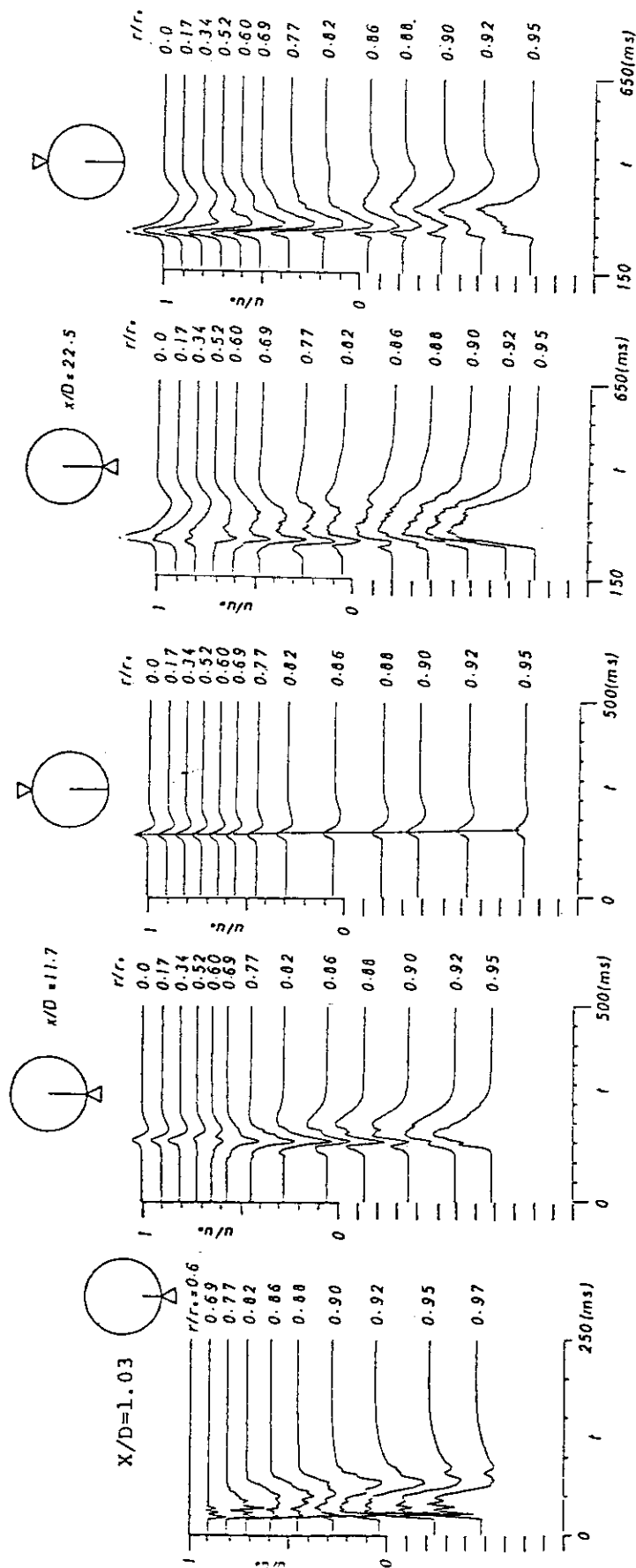

Fig.3.19   A Schematic Diagram of an Apparatus

Fig.3.20 Ensemble Averaged Record of the Streamwise Component of Velocity,
u=⟨u⟩ + u'. u_0 denotes the velocity in the laminar state on the
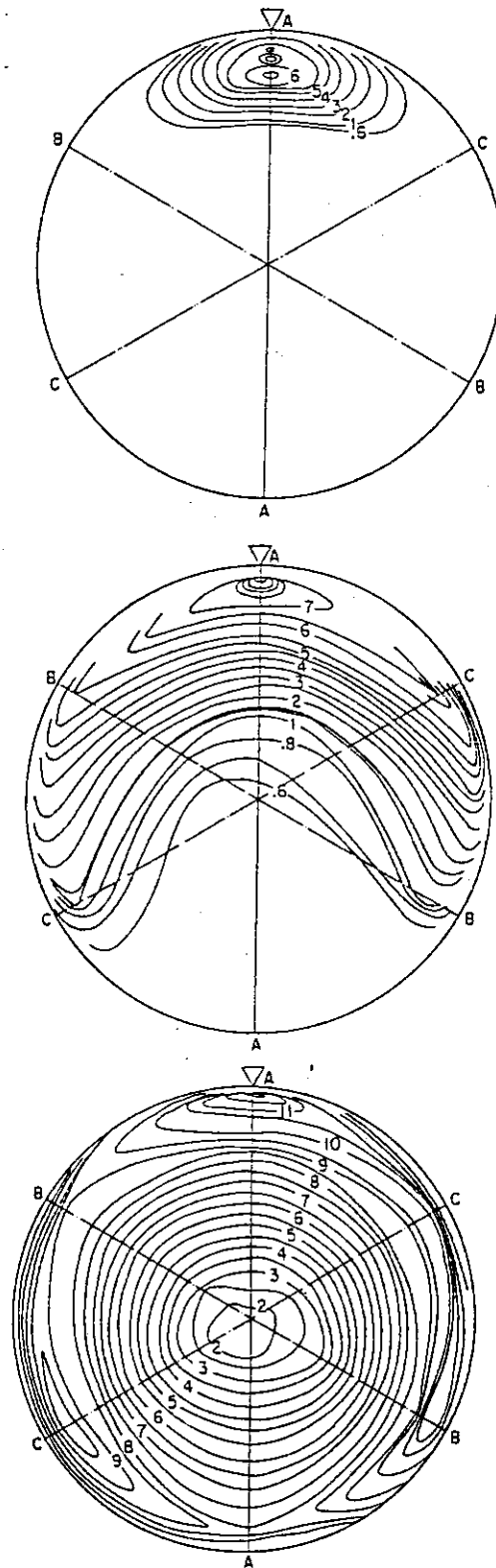centerline of a pipe, r_0 the radius of a pipe.

Fig. 3.21 Equi-RMS Curves of the Fluctuation of Streamwise Velocity, u'.
These curves are obtained by using 100 Hz–10 kHz band path
filters.

3.7 Transient Heat Transfer to Liquid Helium

M. Seki, and K. Sanokawa

Introduction

In order to understand fully the stability of superconducting magnets, knowledge on transient heat transfer to liquid helium is required. As for pool boiling, a lot of data are available for steady state, but a few works have been published on transient conditions.

In an experiment of transient heat transfer, rapid changes in temperature at the heater surface and in heat flux to surrounding fluid must be measured accurately, namely the measuring instrument should be quick to response.

In the present study, the possibility of a germanium thin film for use as a resistance thermometer to measure transient heat transfer of liquid helium has been examined. Germanium was chosen as the sensing material because of its large temperature coefficient of resistance (TCR) which is negative at low temperatures and of its easiness of evaporation.

The fabrication and the characteristics of the germanium thin film thermometers are described and typical results on the measurements of the surface temperatures are given.

Preparation of the germanium film and its characteristics as a resistance thermometer

The germanium films were prepared by vacuum deposition in a conventional bell jar at a pressure of about 1×10^{-3} Pa. The substrates were 40×80 mm stainless steel ribbons, the surfaces of which were insulated by evaporated silicon monoxide films. The ribbons were used as a heater in a liquid helium pool.

In order to obtain polycristalline films of germanium, the substrates were heated up and kept at 400 - 450 °C during evaporation. Electrical contacts were formed on the top of the germanium films by evaporation of silver as shown in Fig. 3.22.

The film thickness was measured with a surface finish microscope by multiple beam interferometry. It was 0.2 - 0.8 μm for silicon monoxide, 0.5 - 1.0 μm for germanium, and 0.3 - 0.6 μm for silver.

A conventional four-wire potentiometric system was employed to determine the resistance of the germanium film. Excitation currents in

the rage of 10 µA - 1.0 mA passed through the films and the potential difference across them were measured by digital voltmeters.

Figure 3.23 shows bi-logarithmic plots of the resistance versus temperature of the typical films. The calibrations indicate that the resistance-temperature curves of the films are smooth without any noticeable bumps in the entire cryogenic range between 4.2 K and 300 K. Figure 3.23 indicates that the fits of these data below 20 K can be expressed by a simple form $\log R = C_0 + C_1 \log T$. The values of C_0 and C_1 are given in the figure.

Transient Heat Transfer Tests

The stainless steel ribbon, 40 mm wide and 80 mm long, and 0.05 mm thick was heated by a direct current in a liquid helium pool under an atomospheric pressure. On both surfaces of the ribbon, insulation and sensing films were deposited.

Typical temperature traces for the stepwise power input are shown in Fig. 3.24. The surface temperature suddenly rises up to a certain value corresponding to superheat of nucleate boiling ($\Delta T_{NB,tr}$). When the heat flux is below the burn-out heat flux, the surface temperature is kept at this superheat, which is equal to the value obtained by a steady state experiment. When the heat flux is higher than the burn out heat flux, the surface temperature begins to rise gradually after keeping $\Delta T_{NB,tr}$ for some time, and reaches the value of the steady state film boiling. The duration time when the surface temperature is kept at $\Delta T_{NB,tr}$ becomes shorter for the higher heat flux.

The steady state boiling curve is obtained with increasing the surface heat flux (Fig. 3.25). The transient superheat of nucleate boiling is shown in the figure by a triangular symbol. The transient superheat is in the extrapolated range of the steady state superheat.
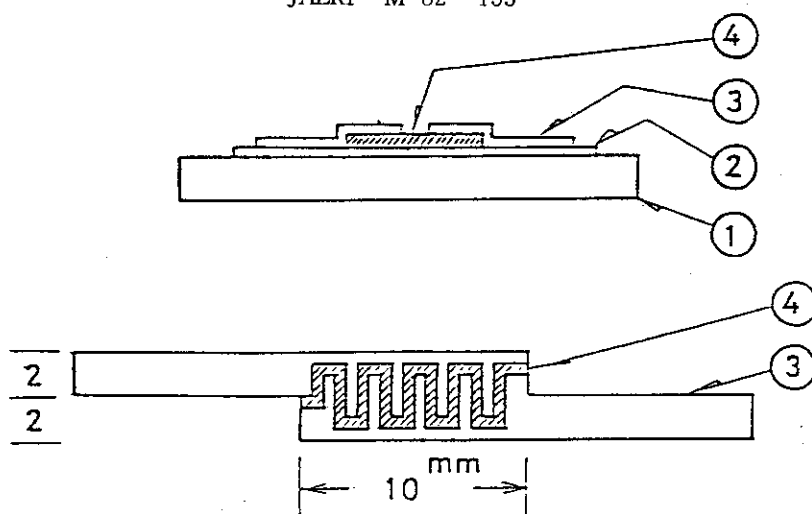
1. SS304 substrate

2. Silicon monoxide insulation film

3. Silver electrodes

4. Germanium sensing film

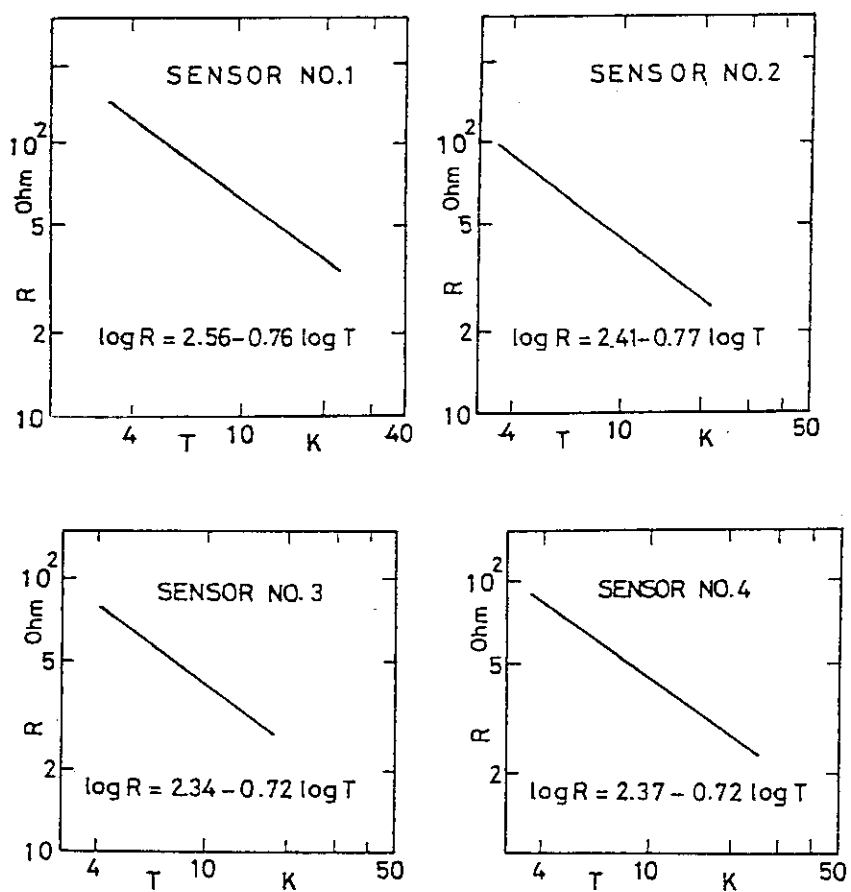Fig.3.22　A Resistance Thermometer

Fig.3.23　Temperature Coefficient of Resistance
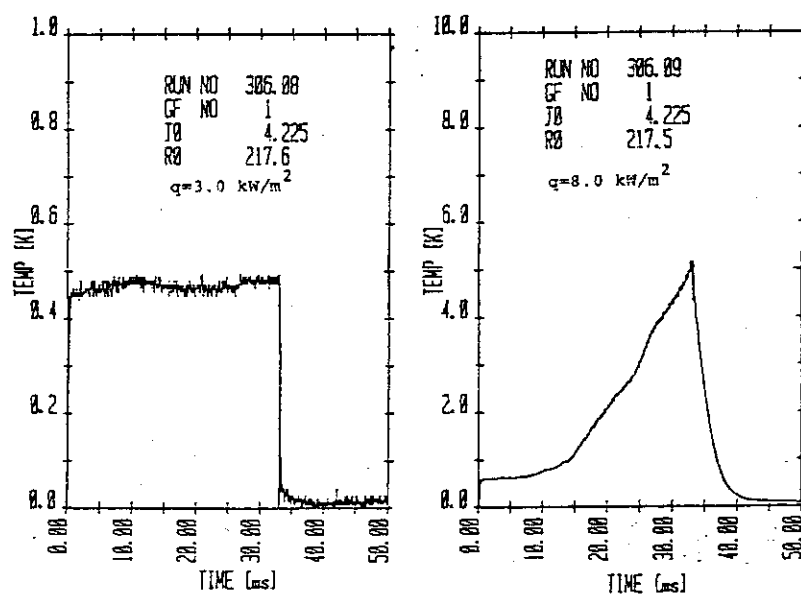
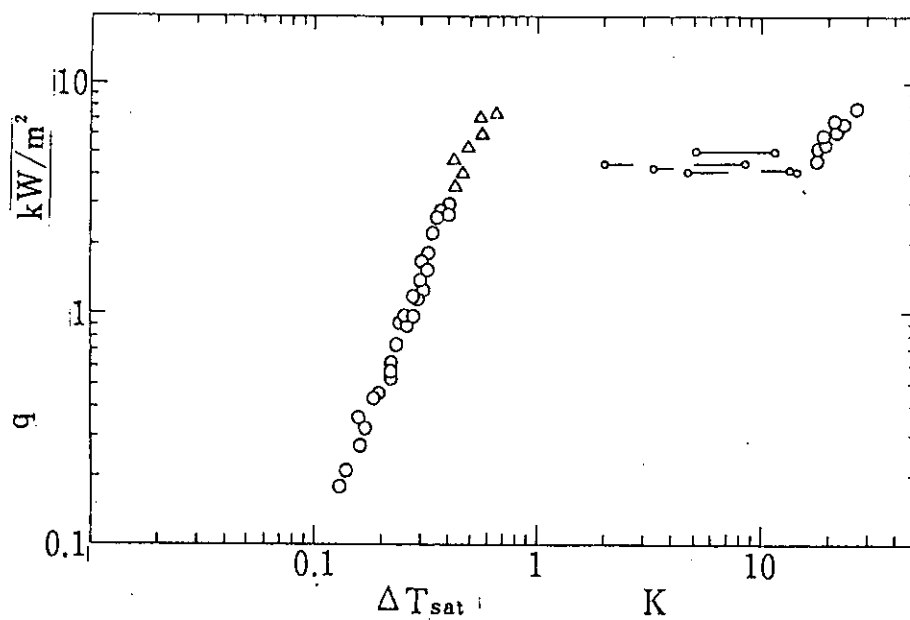Fig.3.24   Typical Temperature Trace for Stepwise
           Power Input

Fig. 3.25   Boiling Curve of Liquid Helium

(Circular Symbols : Steady State   )
(Triangular Symbols: Transient State)

4. RESEARCH ON STRUCTURAL MATERIAL

4.1 Screening Test of Graphite Materials for VHTR

T. Oku, K. Fujisaki, M. Eto and S. Yoda

Introduction

Screening test of graphite materials for VHTR was performed during the period from 1980 to 1981. The detailed results were already reported. In this report we present some new information on ten kinds of nuclear grade commercial graphites.

(1) Correlation between some mechanical and physical properties of polycrystalline graphite.

We studied the correlation between some properties of graphites, based on the results obtained from the screening tests. Figure 4.1 shows that Young's modulus decreases with increasing total porosity. This phenomenon corresponds to the decrease in amount of internal defect in graphite.

Correlation between compressive strength and total porosity is shown in Fig. 4.2, where compressive strength decreases with increasing porosity except some finegrained graphites. A similar tendency was found in the relationship between bending strength and total porosity, but was not found between tensile strength and total porosity. Tensile strength rather depended on coke grain size of graphite material as shown in Fig. 4.3.

Figure 4.4 shows the relation between maximum grain size and log (k_c/σ_t), where k_c and σ_t are fracture toughness and tensile strength respectively. This indicates that graphite materials with the coarser grain size are believed to contain the larger inherent defects. Figure 4.5 shows the correlation between bending (σ_b) and compressive strengths (σ_c) in MPa unit. In this figure the data are well fitted to an equation: $\sigma_b = 0.46\sigma_c + 0.09$. Correlation between tensile (σ_t) and bending strengths (σ_b), and tensile (σ_t) and compressive strengths (σ_c) are also found: $\sigma_t = 0.87\sigma_b - 5.87, \sigma_t = 0.40\sigma_c - 6.55$.

Figure 4.6 shows the strain energy release rate G vs the Warren parameter P_1 indicative of degree of graphitization. In this figure, graphite materials with better graphitization lead to smaller value of strain energy release rate. The result is explained as follows: delamination gives rise to the reduction of thermal stresses generated

by interaction between anisotropic plastic and elastic contractions of
each grain which is believed to be oriented randomly in the graphite
upon cooling from graphitization temperatures. The amount of delamina-
tion increases as the degree of graphitization becomes higher.
And the closed pore in graphite increases as delaminations becomes
more frequent. Therefore, the surface energy which influences strain
energy release rate decreases with the increase in pore volume fraction.

(2) Changes in strength and other properties caused by oxidation.

Ten candidate graphites for VHTR were oxidized at 1000°C in 1.8 vol%
H_2O helium gas to examine the effect of oxidation on bending or compres-
sive strength and other physical properties such as Young's modulus,
electrical resistivity and thermal expansion coefficient. Flow rate
was 650 ml/min (linear velocity 0.45 cm/sec) and reaction temperature
was controlled within ±5°C.

The main results were as follows:

1) Difference in the strength loss between the graphite brands

Figure 4.7 shows the bending strength of oxidized TS-1240 graphite
as a function of burnoff. Ten percent burnoff caused about 50 % strength
loss for six brands of graphites including the oxidized TS-1240 graphite,
whereas the bending strengths of ATR-2E and P3JHA graphites decreased
more than 70 % of their original values. In contrast, the decrease was
about 20-30 % for G140 A and PGX graphites, which was attributable to
oxidation gradients within the specimens.

2) Relationship between strength loss and burnoff

Strength data obtained for various graphites were fitted to an
equation:

$$S/S_m = \alpha(d/d_o)^\beta + (1-\alpha)(d/d_o)^\delta \tag{1}$$

where S, S_m, d and d_o are respectively strength of oxidized specimen,
mean strength of unoxidized specimen and density after and before oxida-
tion. The values of α, β and γ are constants depending on materials.
Table 4.1 summarizes the result of the calculation. As for the relation-
ship between strength loss and density change caused by oxidation, the
following equation has been employed by a number of investigators (1-4).

$$S/S_m = (E/E_o)^\beta, \tag{2}$$

It was found that the data particularly at lower burnoff were represented
well by Eq. (1). The second term of the right-hand side of Eq. (1)
corresponds to the oxidation through micropores which would be dominant
at the earlier stage.

3) Strength loss and Young's modulus

Strength loss caused by oxidation was well related to the Young's modulus by an equation:

$$S/S_m = (E/E_o)^\beta, \tag{3}$$

where E_o and E are the Young's moduli before and after oxidation respectively. The value of β ranged roughly from 0.9 to 1.1, or from 1.4 to 1.6, depending on the kind of graphites examined.

4) Strength loss and electrical resistivity

Figure 4.8 shows the resistivity change caused by oxidation as a function of total burnoff for ATR-2E graphite. All the graphites examined in the present experiment, except PGX and ATJ, showed a good correlation between the changes in resistivity and density, which is expressed as:

$$\rho/\rho_m = a + b(1 - (d/d_o)). \tag{4}$$

Where ρ and ρ_m are respectively the resistivity of oxidized specimens and the mean value of resistivity of unoxidized specimens. The values of a and b are material constants. The latter indicates the resistivity increase caused by oxidation per unit density change. It was found that the strength decrease per unit density change was larger for materials with larger values of b. This suggests that the resistivity would be a good measure for studying the relationship between strength change of graphite and its microstructure.

(3) Stress-strain curves for VHTR graphites

Compressive tests were carried out for graphites except for P3JHA by an Instron-type testing machine. Specimen size was 12 square mm and 25 mm long. Strain was measured by strain gages, which were adhered parallel to loading axis at opposite side of the specimen. Compressive tests were carried out at a strain rate of 3.3×10^{-4} s^{-1}. Load-strain diagram was recorded by an X-Y recorder. Stress-strain curves obtained by compressive tests for 9 commercial graphites are classified into two kinds of compressive behaviors as follows; one (Type 1) is known as the fracture of IG-11 graphite occurred at the point of maximum compressive stress as shown in Fig. 4.9, and the other (Type 2) is like ART-2E graphite which is seemingly unchanged when the applied stress exceeds the maximum compressive stress, as shown in Fig. 4.10, whereas cracking was obviously observed over the surface of a specimen. From the design point of view, since Type 1 graphite behaves considerably as brittle fracture under compressive loading, loading must be kept below

the maximum compressive strength, It is, however, important to note that Type 2 graphite specimen unchanged its shape even at the maximum compressive strength,

A comparison of stress-strain behaviors of VHTR graphites obtained from compressive tests shows as follows:

1) <u>Graphites for fuel element</u>

  1. Stress-strain behavior of TS-1240 graphite is Type 1, whereas, that of H-451 graphite is Type 2.

  2. Fracture strength of IG-11 graphite is the largest, and H-451 and ATR-2E in this order.

  3. Fracture strain of IG-11 is more than 3 % that of TS-1240 and H 451 above 2 %, and that of ATR-2E below 2 %.

2) <u>Graphites for core bottom</u>

  1. Stress-strain behaviors of the three graphites are the same as Type 2.

  2. Fracture strength of ASR-1RG is the largest, and PGX and G-140A, are the next largest in this order.

  3. Fracture strains of across-grain and with-grain specimens of ASR-1RG are more than 2 %, whereas those of across-grain specimens of PGX and G-140A more than 2 % and those of with-grain specimens less than 2 %.

3) Graphites for support post

  1. Stress-strain behaviors of the three graphites are the same as Type 1.

  2. Fracture strength of ATJ is the largest, and IG-11 and V 483T are the next largest in this order.

  3. Fracture strain of IG-11 graphite is more than 3 %, and ATJ and V 483T are the next largest in this order.

Compressive loading-unloading response of IG-11 graphite is shown in Fig. 4.11.

The results obtained here are as follows: .

1. The deformation of graphite does not obey Hooke's law, and plastic deformation occurs even at small stress.

2. Plastic strain increases with increase of stress. Datailed results are described in reference (5).

REFERENCES

1. C. Rounthwaite, G.A. Lyons and R.A. Snowdon, Proc. of 2nd Conf. on
   Industrial Carbon and Graphite, Society of Chemical Industry, London,
   p. 299 (1966).
2. J.A. Board and R.L. Squires, ibid., p. 289.
3. R.H. Knibbs and J.B. Morris, Proc. of 3rd Conf. on Industrial Carbon
   and Graphite, Society of Chemical Industry, London, p. 297 (1971).
4. F.B. Growcock, M. Eto, J. Heiser, 3 and C.A. Sastre, 3rd International
   Carbon Conference, Baden-Barden, June 30-july 4, 1980, Extended
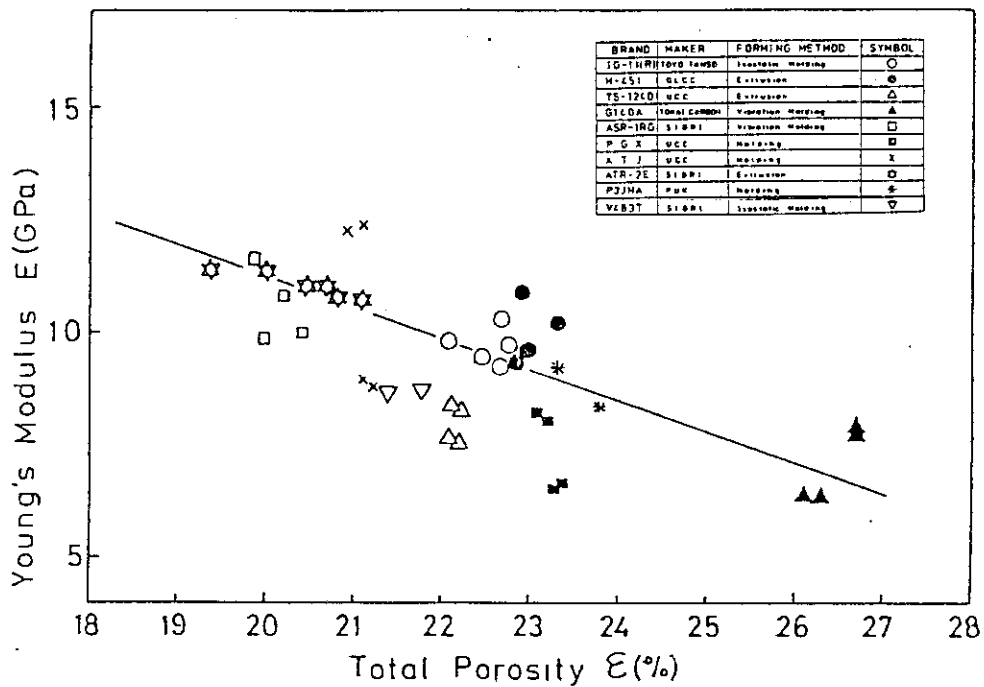   Abstracts, p. 238.
5. Yoda S., JAERI-M 9758.

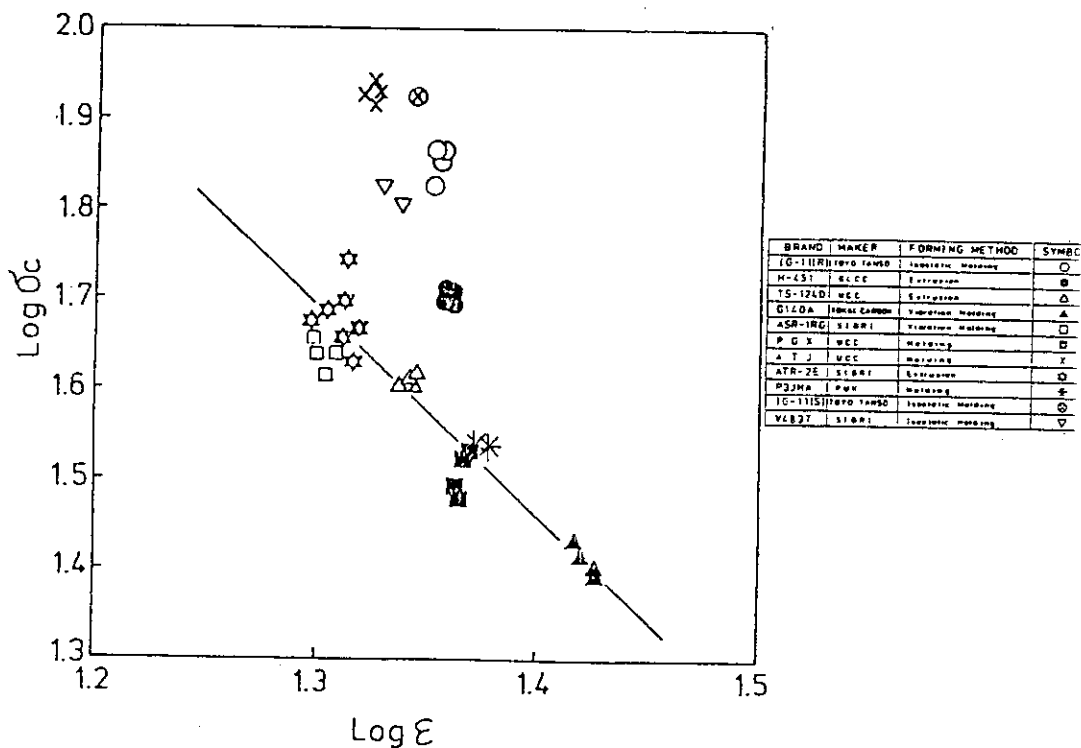Fig.4.1   Porosity vs Young's Modulus of Graphites

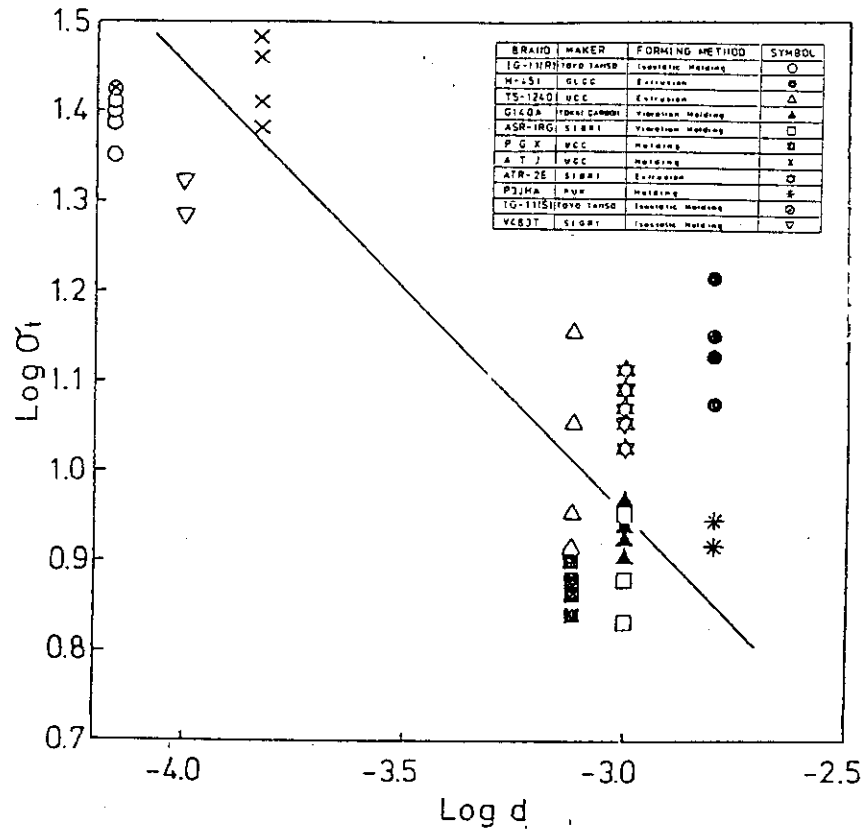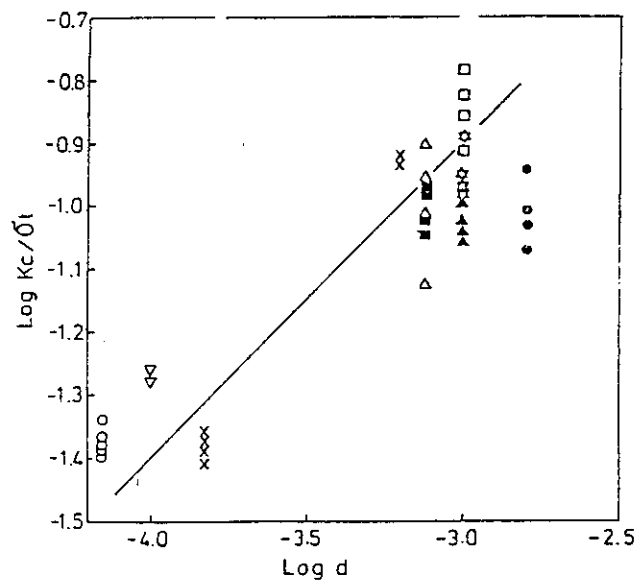Fig.4.2   Compressive Strength vs Volume Fraction of Porosity

BRAND	MAKER	FORMING METHOD	SYMBOL
TG-11HR	Toyo Tanso	Isostatic Molding	○
H-451	GLCC	Extrusion	◉
TS-1240	UCC	Extrusion	△
G140A	Tokai Carbon	Vibration Molding	▲
ASR-1RG	SIGRI	Vibration Molding	□
PGX	UCC	Molding	◘
ATJ	UCC	Molding	X
ATR-2E	SIGRI	Extrusion	✿
P3JHA	PYE	Molding	✴
TG-11ISI	Toyo Tanso	Isostatic Molding	⊘
VC8JT	SIGRI	Isostatic Molding	▽

Fig.4.3　Tensile Strength vs Grain Size

Fig.4.4　Calculated Crack Length vs Grain Size

BRAND	MAKER	FORMING METHOD	SYMBOL
TG-11HR	Toyo Tanso	Isostatic Molding	○
H-451	GLCC	Extrusion	●
TS-1240	UCC	Extrusion	△
G140A	Tokai Carbon	Vibration Molding	▲
ASR-1RG	SIGRI	Vibration Molding	□
PGX	UCC	Molding	◘
ATJ	UCC	Molding	X
ATR-2E	SIGRI	Extrusion	✿
VC8JT	SIGRI	Isostatic Molding	▽
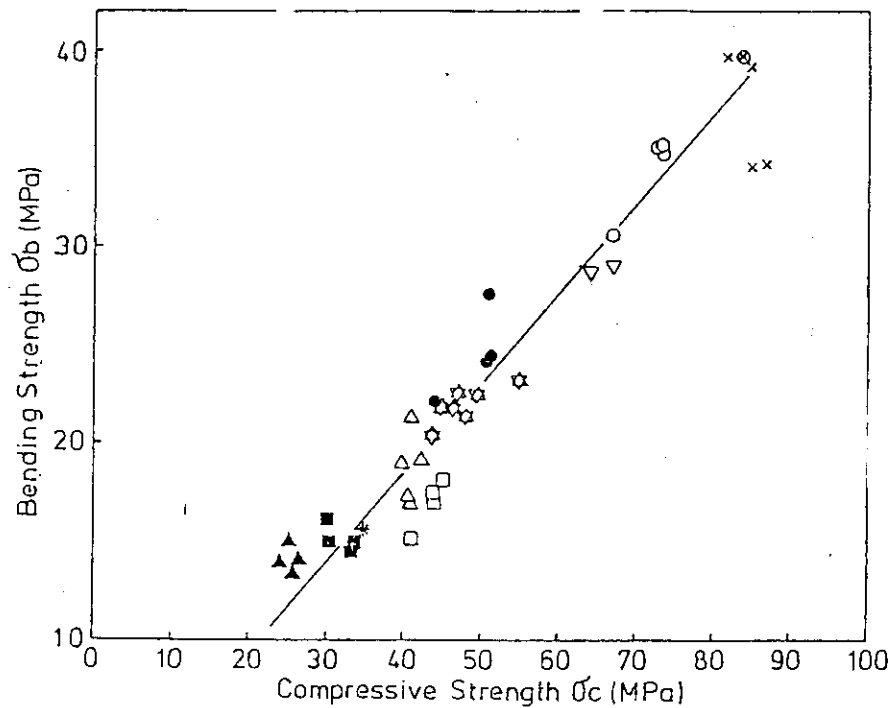
Fig.4.5 Bending Strength vs Compressive Strength

BRAND	MAKER	FORMING METHOD	SYMBOL
IG-11(R)	TOYO TANSO	Isostatic Molding	O
H-451	GLCC	Extrusion	◉
TS-1240	UCC	Extrusion	△
G140A	TOKAI CARBON	Vibration Molding	▲
ASR-1RG	SIGRI	Vibration Molding	□
P G X	UCC	Molding	◪
A T J	UCC	Molding	X
ATR-2E	SIGRI	Extrusion	✿
P3JHA	PUK	Molding	‡
IG-11(S)	TOYO TANSO	Isostatic Molding	⊗
V483T	SIGRI	Isostatic Molding	▽

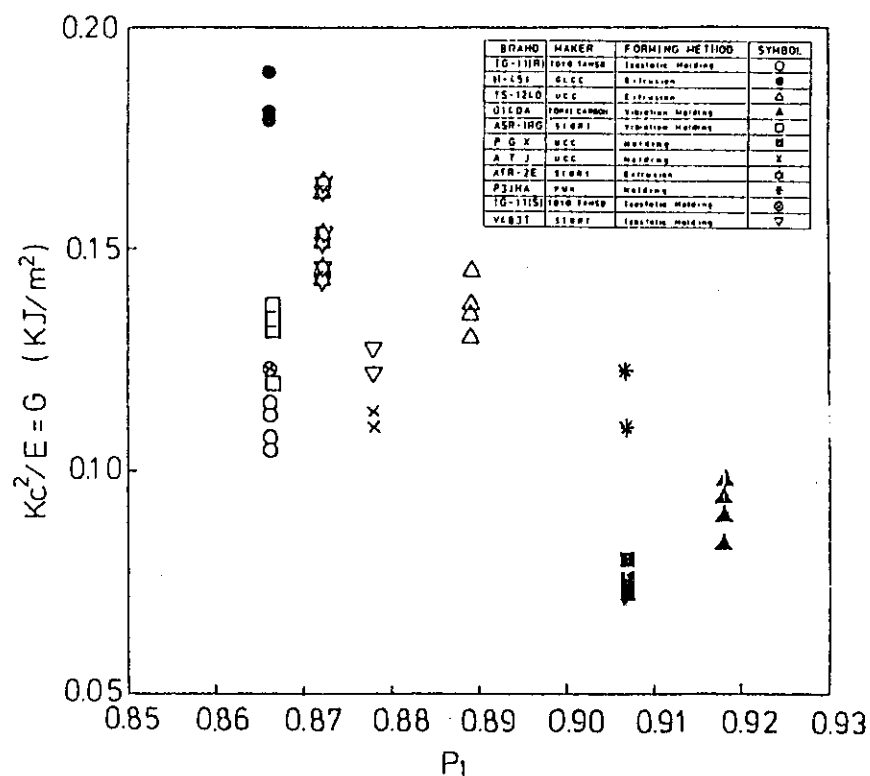| BRAND	MAKER	FORMING METHOD	SYMBOL
IG-11(R)	Toyo Tanso	Isostatic Molding	O
H-451	GLCC	Extrusion	◉
TS-1240	UCC	Extrusion	△
G140A	TOKAI CARBON	Vibration Molding	▲
ASR-1RG	SIGRI	Vibration Molding	□
P G X	UCC	Molding	◪
A T J	UCC	Molding	X
ATR-2E	SIGRI	Extrusion	✿
P3JHA	PUK	Molding	‡
IG-11(S)	Toyo Tanso	Isostatic Molding	⊗
V483T	SIGRI	Isostatic Molding	▽

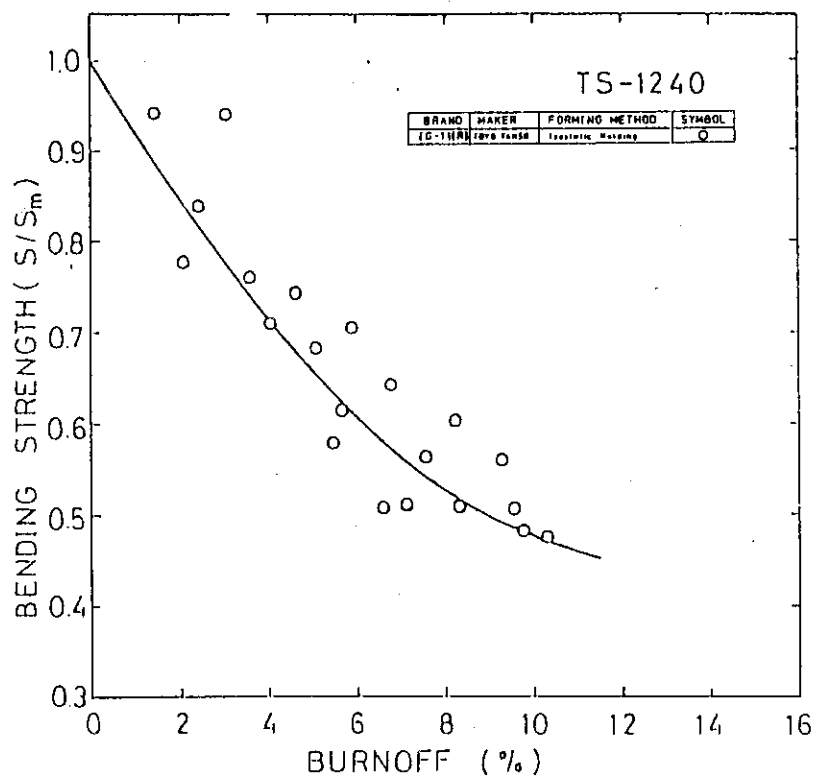Fig.4.6 Strain Energy Release Rate vs Graphitisation

Fig.4.7 Bending Strength of TS-1240 Graphite Oxidized in a 1.8 vol% H_2O/He Mixture at 1000°C
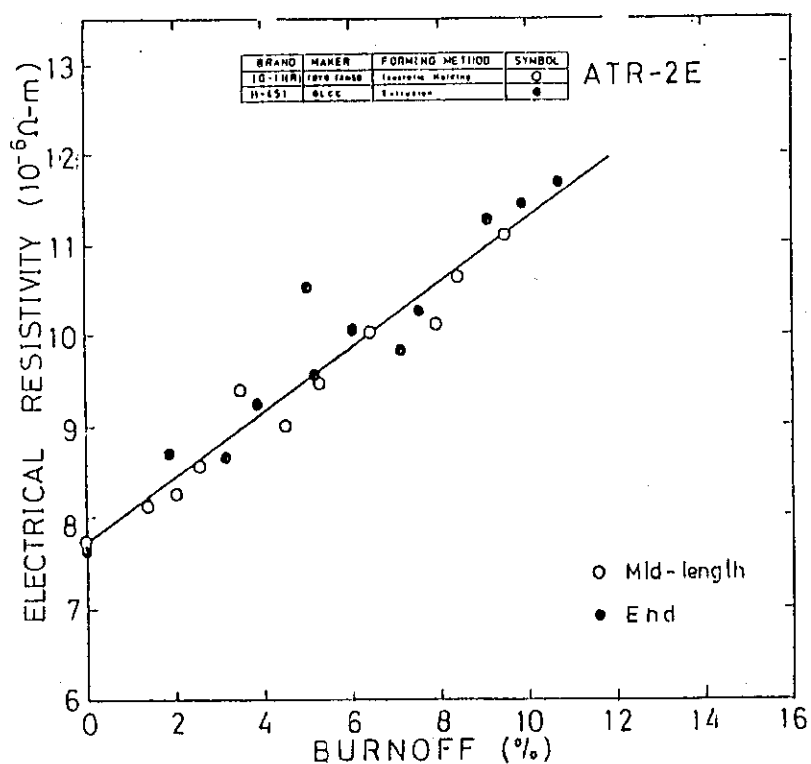

Fig.4.8 Resistivity Increase of ATR-2E Graphite Oxidized in a 1.8 vol% H_2O/He Mixture at 1000°C
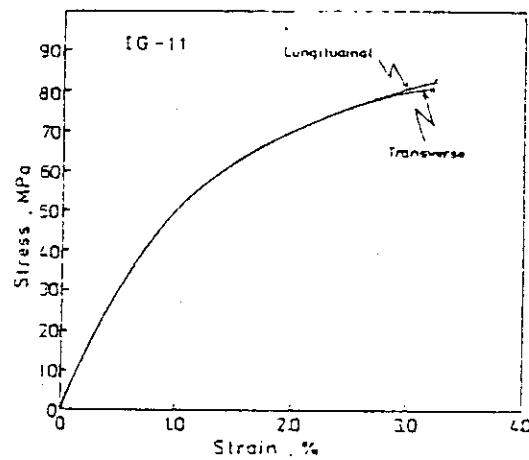
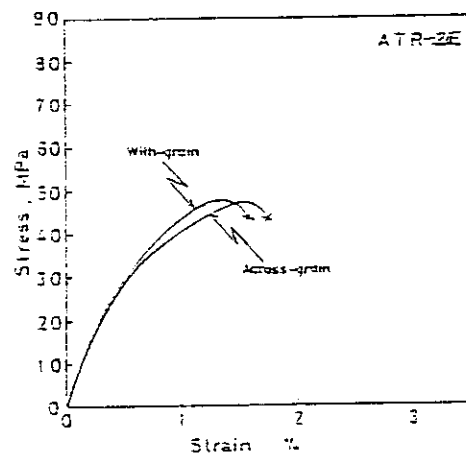Fig.4.9 Compressive Stress-Strain Curve for IG-11
Isotropic Graphite (Type 1)

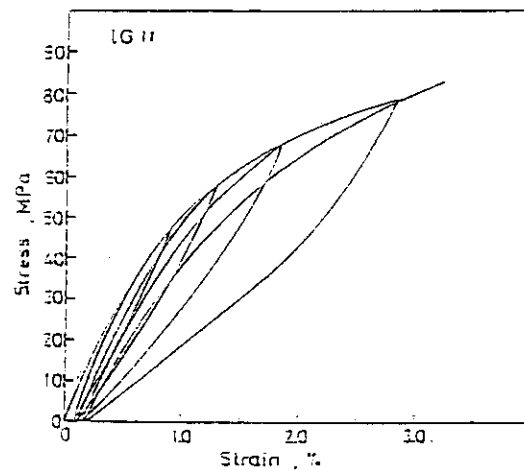Fig.4.10 Compressive Stress-Strain Curve for ATR-2E
Graphite (Type 2)

Fig.4.11 Loading/Unloading Response for IG-11
Isotropic Graphite

4.2 Effects of Mechanical Stressing on Young's Modulus of an Isotropic Graphite

S. Yoda, M. Eto, and T. Oku

Introduction

A large number of pores exist between grain boundaries, and within grains in artificial graphites in general. The exisistence of pores influences considerably mechanical properties of artificial graphites.

It is well-known that Young's modulus of artificial graphites are changed by mechanical prestresses[1),2)]. The causes for this phenomenon described above are generally considered as follows: an increase in mobile dislocation density on the basal plane of the grain when applied stresses are very small, and formation of cracks at large applied stresses.

In this present paper changes in Young's modulus of an isotropic graphite under compressive and tensile stresses are examined. We try to consider the cause of changes in Young's modulus under mechanical stresses.

Experimental Procedure

The graphite material used in the experiment was an isotropic polycrystalline graphite. Compressive and tensile tests were carried out using an Instron testing machine at a strain rate of 4.0×10^{-5} sec^{-1}. The sizes of specimens for tensile and compressive tests are respectively 10 mm in diameter and 40 mm in gage length, and 12 square mm and 25 mm long. Strain gages (2×5 mm) were adhered to both sides of the specimens to cansel the bending strains. Load-strain curves were recorded automatically on an X-Y recorder. Ultrasonic velocity traveling through a specimen was measured continuously during tensile or compressive tests using 5 MHz ultrasonic longitudinal wave. Young's modulus of the graphite was calculated using the equation: $E = \rho v^2$, where E, ρ, and v are respectively Young's modulus, bulk density and sound velocity.

Results and Discussion

Figure 4.12 (a) and (b) show changes in longitudinal Young's modulus of the graphite calculated from sound velocity under tensile and compressive stresses, where E_o is Young's modulus of graphite without applied stresses. It is clearly seen from the figures that the dynamic Young's modulus of graphite decreased continuously with increasing compressive or tensile stress. Correlation between the Young's

modulus and tensile stress-strain behavior is shown in Table 4.1.
The table shows that the correlation between stress-strain behavior upon
the reversal of loading, and the dynamic Young's modulus calculated from
sound velocities under tensile testing. It is evident here that the
stress-strain behavior is related closely to relative Young's modulus
calculated from sound velocities.

Fugure 4.13 shows a comparison of decrease in Young's modulus under
tensile stress with that under compressive stress. As is seen from
the figure, the decrease in Young's modulus under tensile stress is
larger than under compressive stress. It is not believed that only the
increase of mobile dislocation density results in the above feature.
The stress-strain curves under compressive and tensile tests fairly
coincide with each other, so that the dislocation density of the specimens
between tensile and compressive tests should be almost the same, leading
us to deduce that the decreases in Young's modulus of the two should be
also similar. However, it is not the case. We consider that the feature
is attributable to effects of changes in pore configuration caused by
applied stress on Young's modulus of the graphite. The results of mercury
porosimetry for the specimens after compressive and tensile tests show
that an increase in specimen volume after tensile tests, and a decrease
in specimen volume after compressive tests were observed. These results
described above suggest that the decrease in pore volume and the change
in pore configuration, and formation of cracks and transcrystalline
cleavage cracks on the basal plane seem to occur considerably.
We assumed that the pores in the graphite are inclusions whose Young's
modulus is zero. We predicted the effects of pore volume and change
in configuration of pores according to the above assumption[3],[4].
The predictions obtained from the calculations are shown in Figs. 4.14
and 4.15. Figure 4.14 shows that in the case of compressive tests Young's
modulus of the graphite decreases as the result of compressive loading-
originated changes of pore configuration into spheroidal shape perpen-
dicular to loading axis. Figure 4.15 shows the prediction for the case
of tensile tests. It is clearly seen from the figure that a small amount
of the transcrystalline cleavage cracks increasing with the applied
tensile stress decrease the Young's modulus of the graphite extremely.

It is concluded that the decrease in Young's modulus under
compressive and tensile stress is attributed to the volume fraction of
pores, and the transcrystalline cleavage cracks on the basal plane,
caused by mechanical stresses.

REFERENCES

1. Hart P.E.: Carbon 10, 233 (1971)
2. Oku T et al: Carbon 15, 3 (1977)
3. Price R.J.: Phil. Mag. 12, 561 (1965)
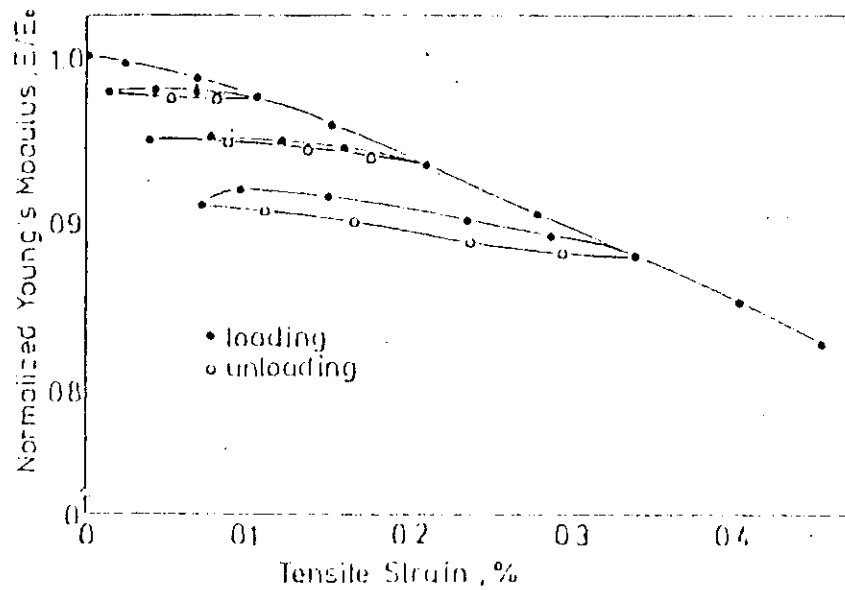4. Eshelby J.D.: Proc. Roy. Soc, 241A, 376 (1957)

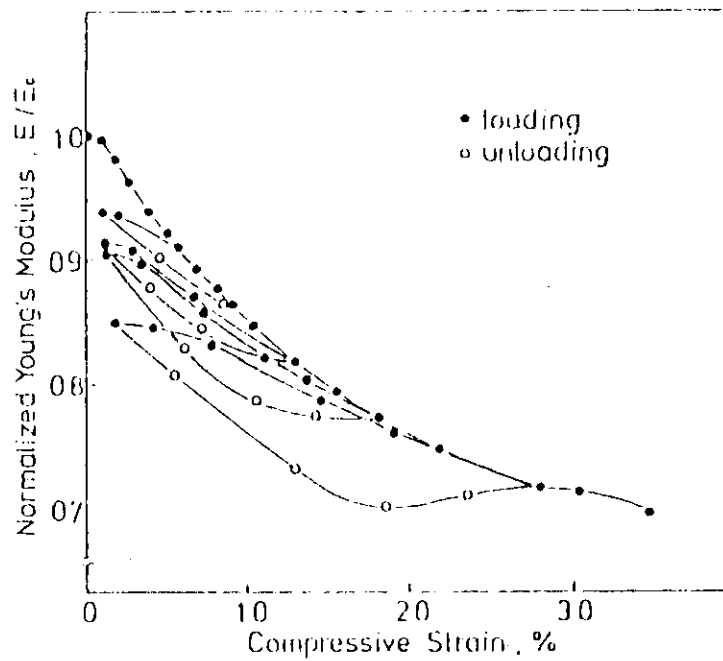Fig.4.12(a)   Normalized Young's Modulus   vs Tensile Strain
Diagram

Fig.4.12(b)   Normalized Young's Modulus vs Compressive
Strain Diagram
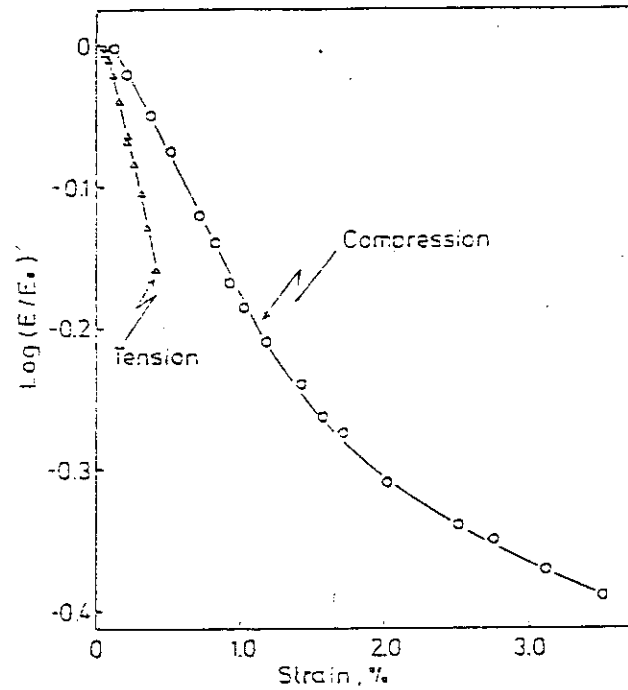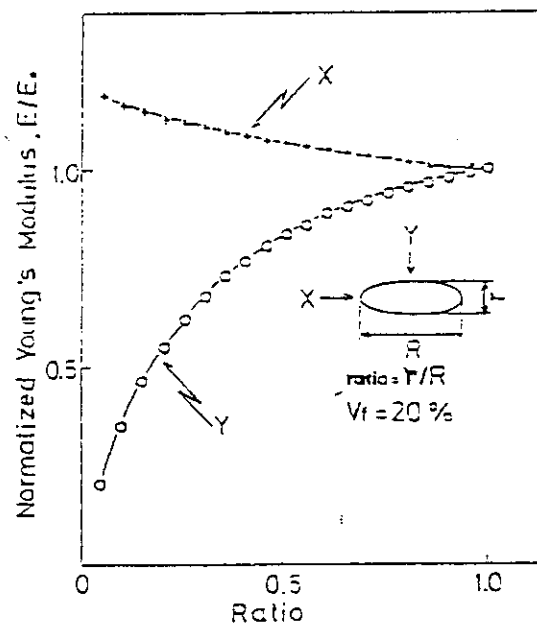
Fig. 4.13 Log(E/E$_O$) vs total strain diagram

Fig. 4.14 Normalized Young's modulus vs ratio of minor axis/major axis
of spheroidal pore diagram showing the effect of change in
pore configuration on Young's modulus of polycrystalline
graphite
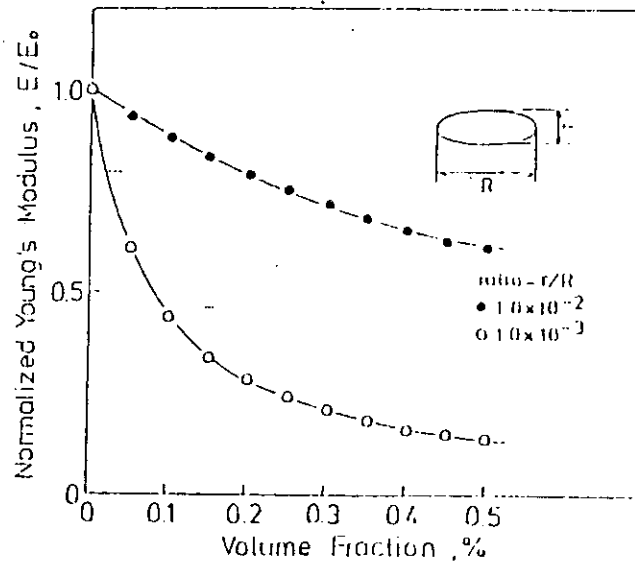
Fig. 4.15 Normalized Young's modulus vs volume fraction of spheroidal
pore having various ratio diagram showing the effect of
ratio on Young's modulus of polycrystalline graphite

Table 4.1 Normalized Young's modulus (E/E_o) obtained for stress-strain
relationship and normalized sound velocities at a given
strain for IG-11 graphite on tensile tests. The normalized
sound velocities correspond to the normalized Young's modulus
in accordance with the equation, $E=\rho v^2$.

	E (%)	E (GPa)	E/Eo	(V/Vo)²
L	0	9.42	1.000	1.000
L	.105	9.35	.993	.992
U	.011	9.17	.970	.974
L	.195	8.96	.950	.951
U	.035	9.16	.972	.972
L	.360	8.29	.880	.880
U	.070	8.66	.920	.920

4.3 Fatigue Properties

S. Ishiyama and T. Oku

Introduction

Cyclic fatigue life of graphite materials is required for the structural design and the safety evaluation for the core graphite structure of VHTR. Cyclic fatigue tests were performed with various ratios of the minimum applied stress to the maximum. Fatigue life data obtained here were arranged using a statistical procedure.

Experimental

Fatigue tests on isotropic graphite IG-11, which is one of the candidates for the core structures of VHTR, were performed using the servo-controlled hydraulic testing machines at a constant loading speed of 256 kg/s. Loading conditions were decided according to R-values (= $\sigma_{min}/\sigma_{max}$; ratio of the minimum applied stress to the maximum) of 0.5, 0, -1, -3.5, -∞, 1/0.3 and 1/0.7.

Results

Figure 4.16 shows a typical fatigue S-N curve for R = -1. The straight line was decided by assuming a statistical fatigue model in low cycle region:[1]

$$\log_{10} (\sigma_{max}/\bar{S}) = A + B \log_{10} N_f$$

where σ_{max} is a peak tensile stress, $\bar{S}$ is a mean tensile or compressive strength. The values of A and B were decided by assuming statistical normal distribution function for the fatigue life distribution at each applied stress. Results of the statistical analysis were shown in Table 4.2.

Figure 4.17 shows the Goodmann diagram which summarizes all the fatigue data. The curves in the diagram give relationships between the coordinate variables at equi-fatigue life cycles which are 10, 10^2, 10^3, 10^4 and 10^5 cycles. The first quadrant includes pull-pull fatigue mode (R= 0.5 and 0), the second quadrant includes push-pull fatigue mode (-1 and -3.5), and the third one is push-push fatigue mode (-∞, 1/0.3, 1/0.7). Each equi-fatigue life curve runs through three quadrants smoothly and distances between curves increases as R value decreases. The curves turn round drastically in the region between R=-3.5 and -∞.

Table 4.2   S-N Curves for Various R-Values Obtained by a
Statistical Method

Stress ratio, R ($\sigma_{min}/\sigma_{max}$)	Intercept of least squares line, A	Slope of least squares line, B	Homologous stress σ_H for survival to 10^3 cycles
0.5	0.0111	-0.020	0.894
0	0.0241	-0.031	0.853
-1	0.0306	-0.041	0.808
-3.5	-0.0531	-0.046	0.644
-∞	0.0111	-0.0216	0.884
1/0.3	0.0080	-0.0196	0.890
1/0.7	0.0048	-0.0115	0.934

Fig.4.16   An S-N Curve for R=-1

minimum stress, σmin, MPa

[IG-11 Goodman Diagram]

$\overline{\sigma}_t = 25.4$ MPa

$\overline{\sigma}_c = 84.7$ MPa
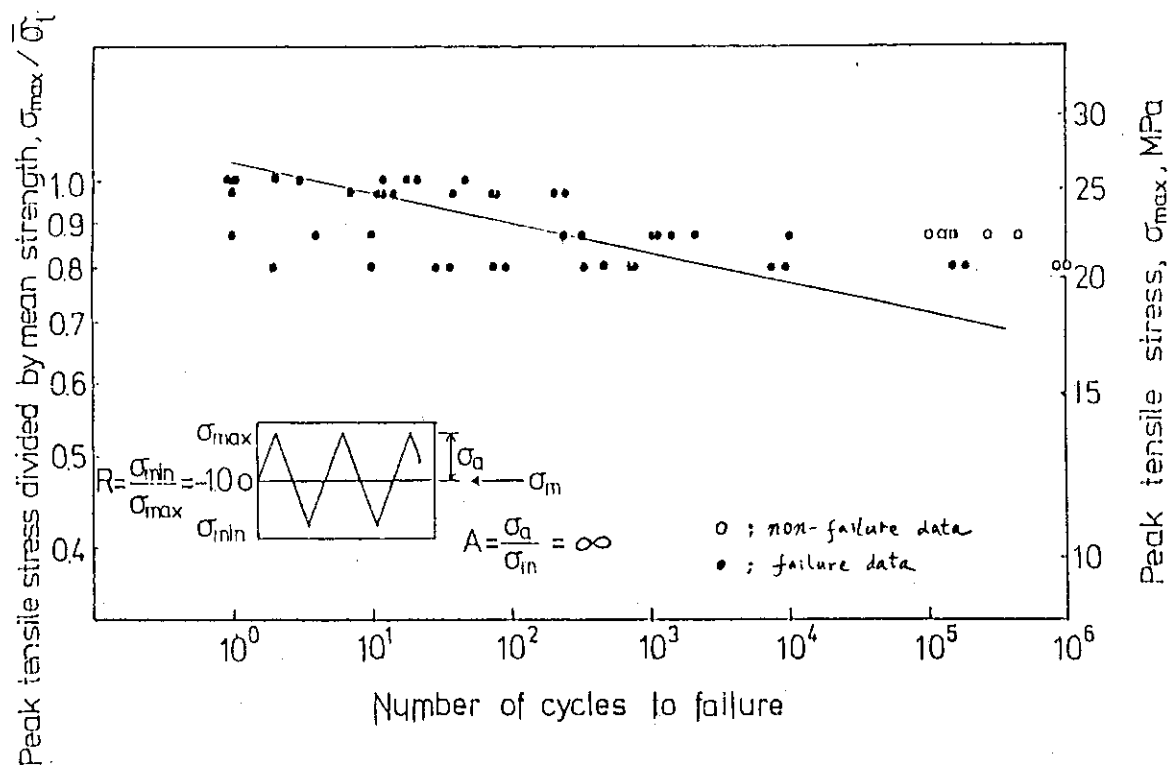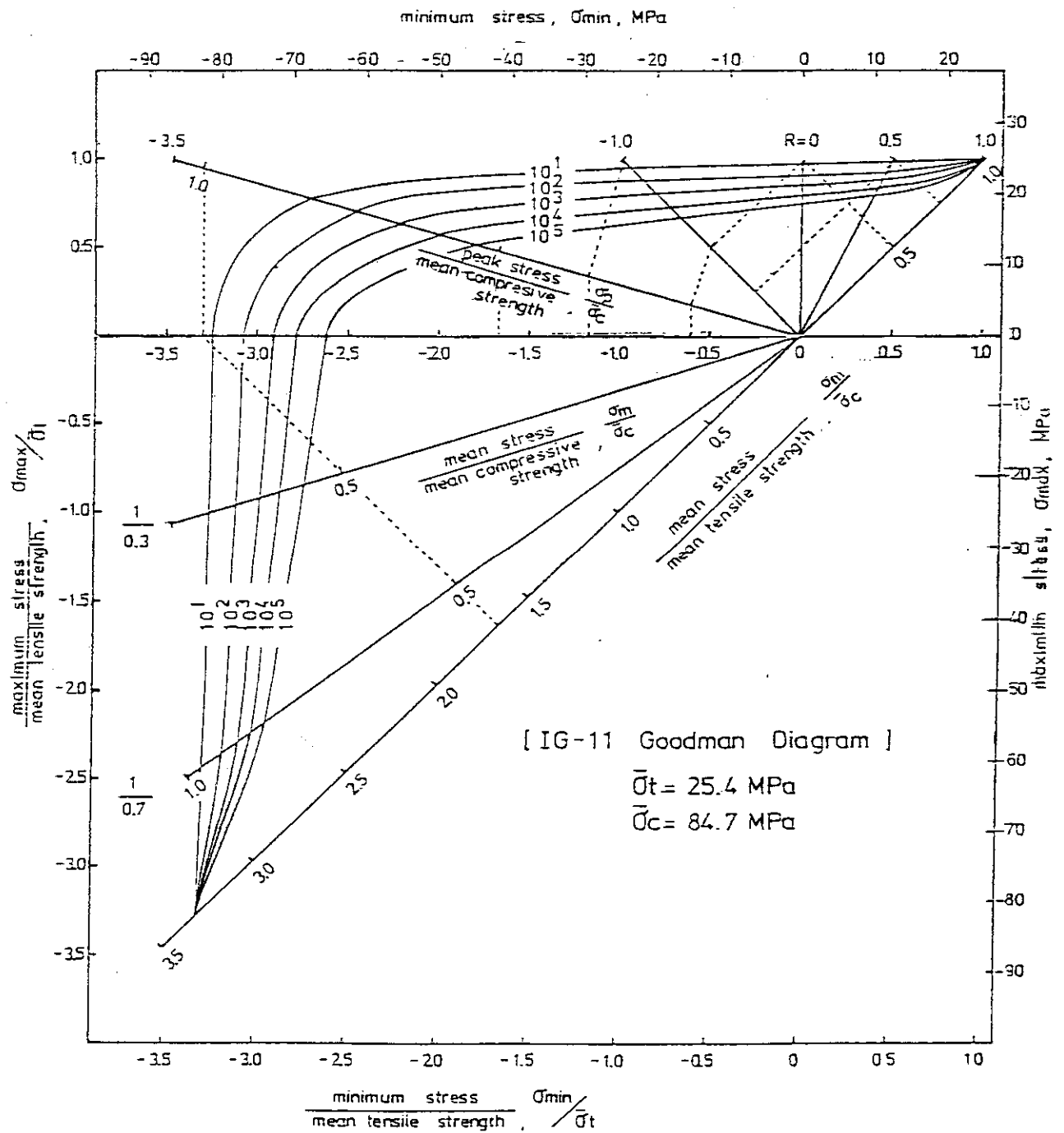
Fig.4.17   Goodman Diagram

4.4 Effect of Neutron-Irradiation on Static and Fatigue Strength of HTGR Graphite

M. Eto, K. Fujisaki, S. Yoda, S. Ishiyama and T. Oku

Current Status

Static strengths and the Young's modulus have been examined for various HTGR graphites irradiated at temperatures of 450∿1200°C, using JMTR and JRR-2 at JAERI and HFR at Petten, the Netherlands. Efforts are currently made to accumulate the data on an isotropic graphite manufactured by a domestic company. Study on irradiation effect on fatigue strength of HTGR graphites has also been under way. For this purpose, ring compression test specimens are used.

Result

Figure 4.18 summarizes the data on the bending, compressive and ring compressive strengths of IG-11 graphite irradiated at high temperature.

Here, the increases in strength are plotted as a function of irradiation temperature. The neutron fluence ranged from 1.54 to 2.94×10^{21} n/cm (E>0.18 MeV). It is apparent that the strength increase caused by irradiation depends strongly on irradiation temperature, indicating that regardless of the kind of strength it decreases at a rate of ca. 0.2 %/°C as temperature rises.
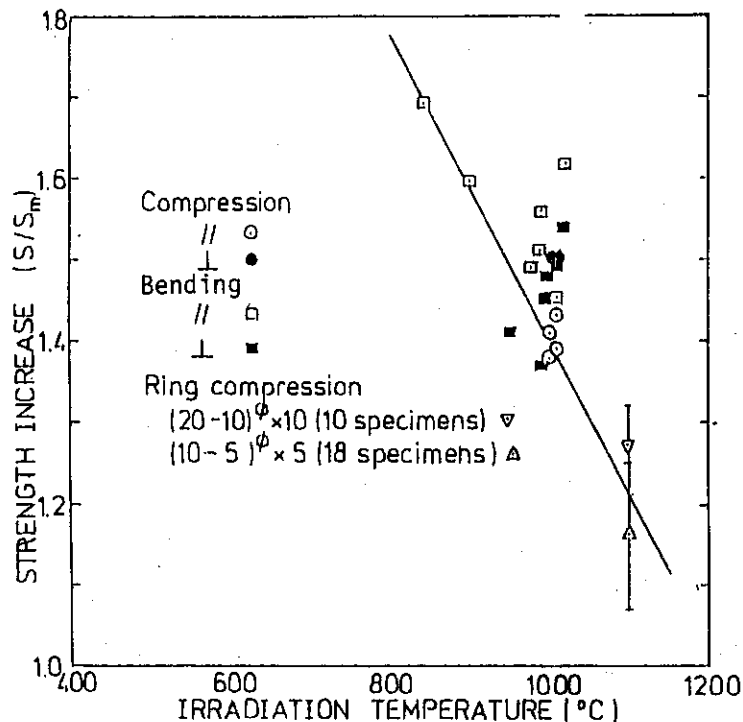

Fig.4.18 Strength increase of IG-11 graphite irradiated at various temperatures

4.5 Irradiation Creep Test of SM1-24 Graphite

T. Oku, K. Fujisaki and Eto

Introduction

The irradiation creep data of graphite are important indispensably to evaluate accurate stresses generated in graphite structures during operation. At present, however, the data have not yet been accumulated in a world-wide scale as the other property data, because of difficulties in experimental techniques and economical reason. In-pile irradiation creep test program was started in 1976, preliminary out-pile and in-pile experiments as well as two final tests were carried out. All the experiments were successfully completed, and the irradiation creep coefficient was obtained from the final tests. In addition to the irradiation creep coefficient, mercury porosimetry measurements were made on the specimens after irradiation under loading and unloading conditions.
And the effect of irradiation creep deformation on Young's Modulus was examined.

Experimental

Tensile creep specimens were used in the test, which were made of SM1-24 graphite. Figure 4.19 shows an outline of irradiation creep capsule. Seven creep specimens were used per capsule, and four specimens that were not loaded were arranged around the parallel section of each creep specimen. Tensile load is applied to creep specimens by means of applying external pressure to bellows. The temperature of the specimens is raised and controlled by gamma heat and an electric heater. Irradiation tests were performed at 850-920°C up to about $1.3 \times 10^{21} n/cm^2$ (E>0.18 MeV).

Results

In general the irradiation creep strain (ε_c) of graphite can be expressed by an equation:

$$\varepsilon_c = \frac{\sigma}{Eo} (1-e^{-a\Phi})+K\sigma\Phi \tag{1}$$

where σ is an applied stress, E Young's modulus of unirradiated specimen, Φ a neutron fluence, K an irradiation creep coefficient, α a constant. For the larger neutron fluence the exponential term in Eq. (1) can be neglected, and then rewritten approximately as:

$$\varepsilon_c = \frac{\sigma}{Eo} + K\sigma\Phi \qquad \qquad (2)$$

On the other hand, ε_c can be determined from dimensional change of an unloaded specimen (ε_d) and that of a loaded specimen (ε_{gp}), using Eq. (3).

$$\varepsilon_c = \varepsilon_{gp} - \varepsilon_d \qquad \qquad (3)$$

Therefore, an irradiation creep coefficient (K) is obtained from Eqs. (2) and (3).

An irradiation creep strain (ε_c) normalized by initial strain (σ/Eo) is expressed by Eq. (4), rearranging Eq. (2).

$$\frac{E_o}{\sigma} \varepsilon_c = 1 + KE_o\Phi \qquad \qquad (4)$$

The values of $Eo\varepsilon/\sigma$ are expressed as a function of fluence (Φ) as shown in Fig. 4.20.

The irradiation creep coefficient (K) is determined from the slope of Eq. (4), provided that it holds for the larger neutron fluence. The values of K obtained by two irradiation creep tests, as shown in Fig. 4.20, were the lowest among the data appeared so far.

SM1-24 (AXIAL)

CAPSULE	K. 10^{-20}(MPa n/m^2)$^{-1}$
76M-19A	3.05
77M-10A	3.20

$E\varepsilon_c/\sigma$

NEUTRON FLUENCE, $\overline{\Phi}$, 10^{24} n/m^2 (E > 0.18 MeV)
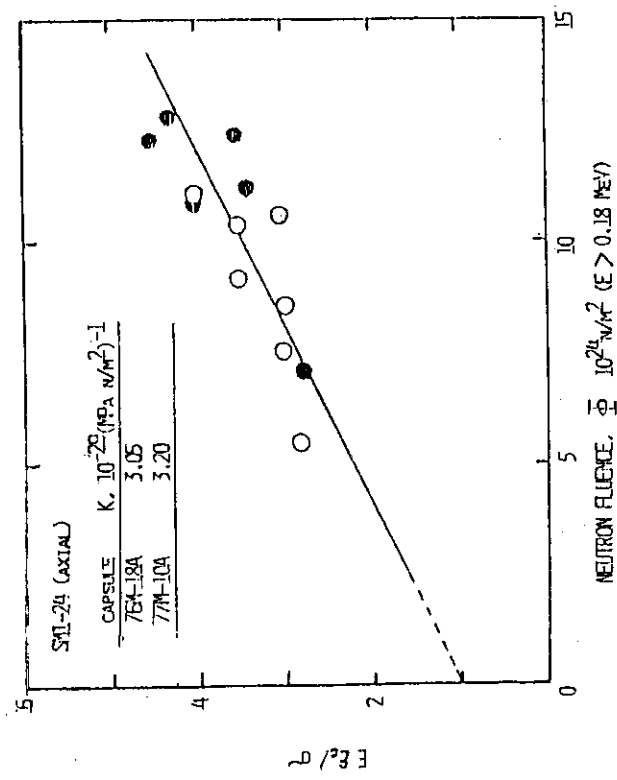
Fig.4.20 Relation between $E\varepsilon_c/\sigma$ and $\overline{\Phi}$.
The Slope of the Line Gives KE_0 Values.
Irradiation Temperature = 670$\sim$900°C

Loading section
Helium applied
Bellows
Joint
Guide tube
Stress free specimens
Stressed specimens
Electric heater
Outer tube
Fixing pin

Fig.4.19 Outline of Irradiation Creep Capsule

4.6 Bowing Characteristics of Graphite Sleeve for HTGR

M. Eto, K. Fujisaki, S. Yoda and T, Oku

Introduction

Even during normal operation of VHTR, it would be probable that fuel sleeves might bend because of temperature gradients along circumferential or longitudinal direction as well as dimensinal changes of graphite due to neutron irradiation. Moreover, if a sleeve is restrained by graphite blocks and other components, stresses would be generated within the sleeve. Efforts have been made to obtain out-pile data on the sleeve bowing caused by temperature gradients along the circumferential direction since such data would be necessary for the evaluation of in-pile sleeve bowing. For this purpose a special rig equipped with a graphite heater was set up.

Experimental

Simplified sleeve specimens were machined from IG-11 graphite. Schematic view of the apparatus and dimension of a specimen are shown in Fig. 4.21. Specimens were heated in vacuum by a graphite heater which was placed longitudinally at one side of a sleeve. The 24 CA thermocouples were attached to a specimen (6 points along the longitudinal axis and 4 points circumferentially at each longitudinal point) to measure the temperature gradient. The amount of bowing was measured with actuators placed near the upper and middle parts of a specimen and a micrometer set at the bottom part of a specimen.

Results

Non-uniform heating gave rise to the circumferential difference in temperature ranging from 100 to 300°C at unsteady state, and from 40 to 100°C at steady state. An example of the results obtained is shown in Fig. 4.22. By adding a term which expresses the strain caused by difference in thermal expansion to the equation for bowing of a hollow tube, the following equation is derived.

$$\frac{1}{\rho} \left[\frac{4I}{\pi e(r_2^2 - r_1^2)} + 2e \right] = \alpha \Delta T \qquad (1)$$

where, ρ: radius of curvature

$\quad\quad$ I: moment of inertia of area

$\quad\quad$ e: section modulus

$\quad\quad$ r_1: inner radius

$\quad\quad$ r_2: outer radius

$\quad\quad$ α: coefficient of thermal expansion

$\quad\quad$ ΔT: temperature difference

$\quad\quad$ For the example shown in Fig. 4.22, Eq. (1) gives a value 1.92 mm for the displacement at the upper part at 170°C. Thus, it is believed that the bowing of graphite sleeve caused by temperature difference can be expressed well by the above equation.
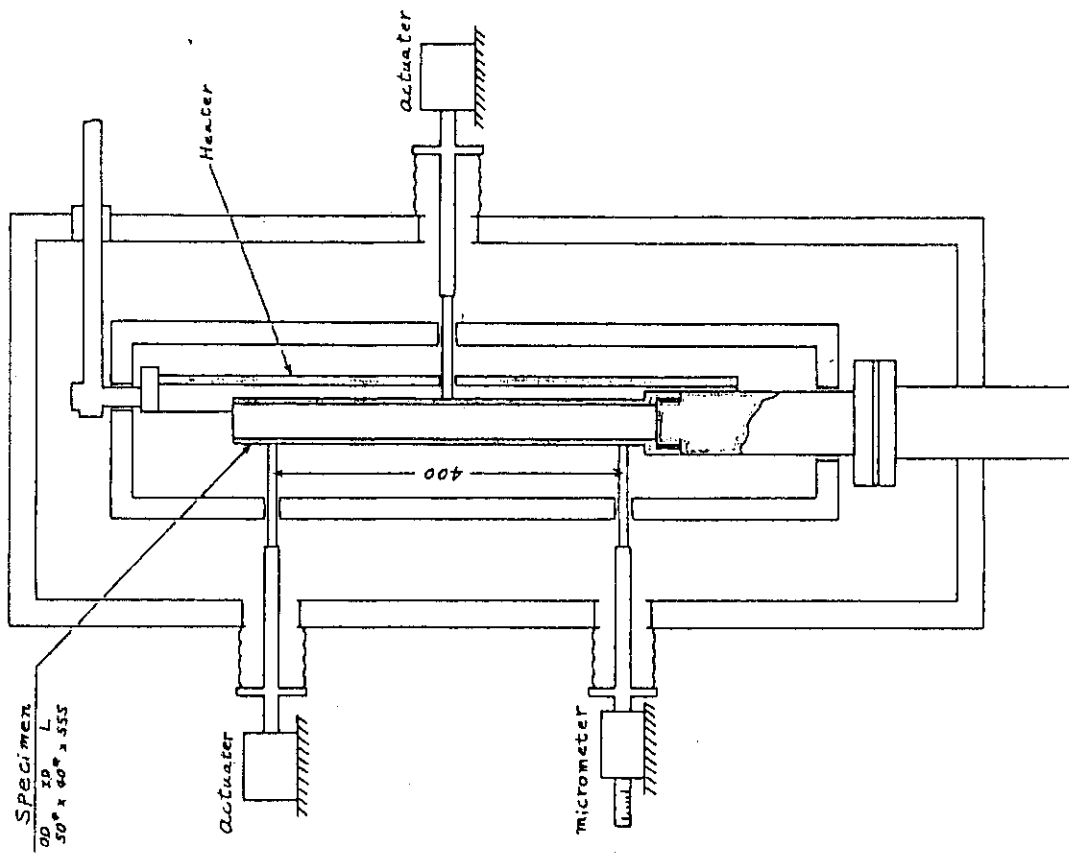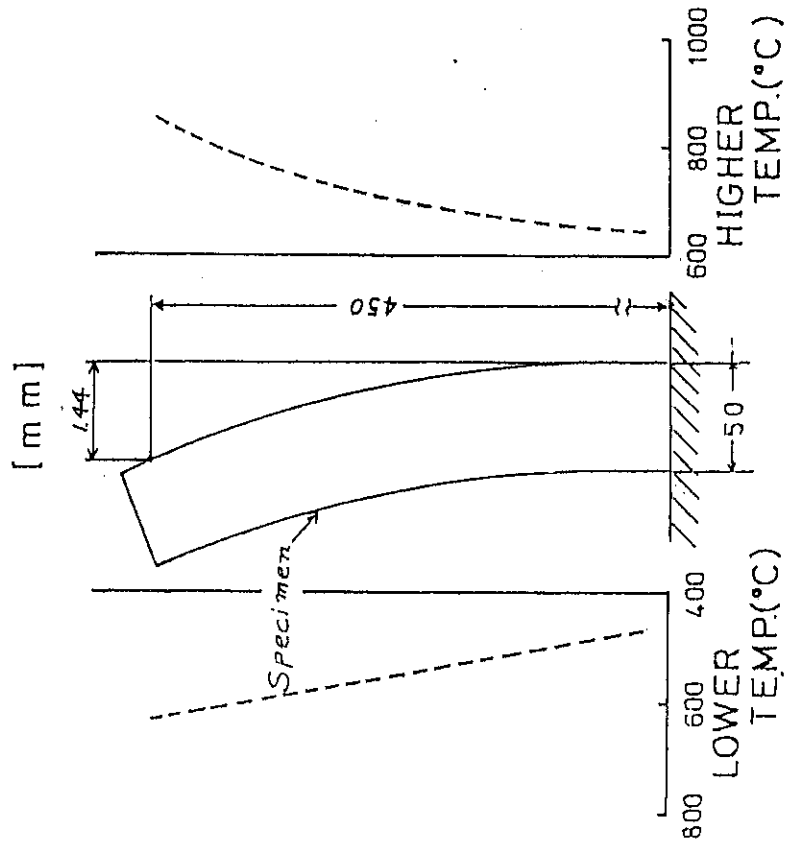
Fig.4.22   An Example of the Bowing Test

Fig.4.21   Schematic View of the Apparatus

4.7 Experiments on Neutron Irradiation Embrittlement

T. Oku, K. Fukaya, M. Suzuki and T. Kodaira

Introdution

There are very limited data on neutron irradiation embrittlement of $2^1/_4$Cr-1 Mo steel which is a candidate material of a VHTR pressure vessel. Since the operation temperature of the VHTR pressure vessel is around 400°C, it is important to clarify the effect of reutron irradiation on temper embrittlement for such pressure vessel steels. Neutron irradiation embrittlement tests are now in progress on $2^1/_4$Cr-1 Mo steels including welded joints as well as base metals.

Experimental Procedure

Neutron irradiation was carried out in JRR-2 and JMTR up to the order of 10^{19}n/cm^2(>1MeV) at around 400°C. The neutron irradiation embrittlement was mainly evaluated by the change of the transition temperature of Charpy impact tests before and after neutron irradiation.

Experimental Results

Figure 4.23 shows the change of the transition temperature as a function of neutron fluence derived from the data of several investigators and the present study as well. From these results, it can be pointed out that copper has a unfavorable effect on the elevation of transition temperature change due to neutron irradiation. Judging from the trends up to the order of the neutron fluence of 10^{19}n/cm^2, the shift of the transition temperature is not appreciable at the irradiation temperature around 400°C.

Future Plan

The following experiments will be conducted in the near future.
1) Effect of neutron irradiation on the iso thermal aged and stress aged steels, including on the base metals and also on the welded joints.
2) J_{Ic} and K_{Id} fracture toughness tests of irradiated steels.
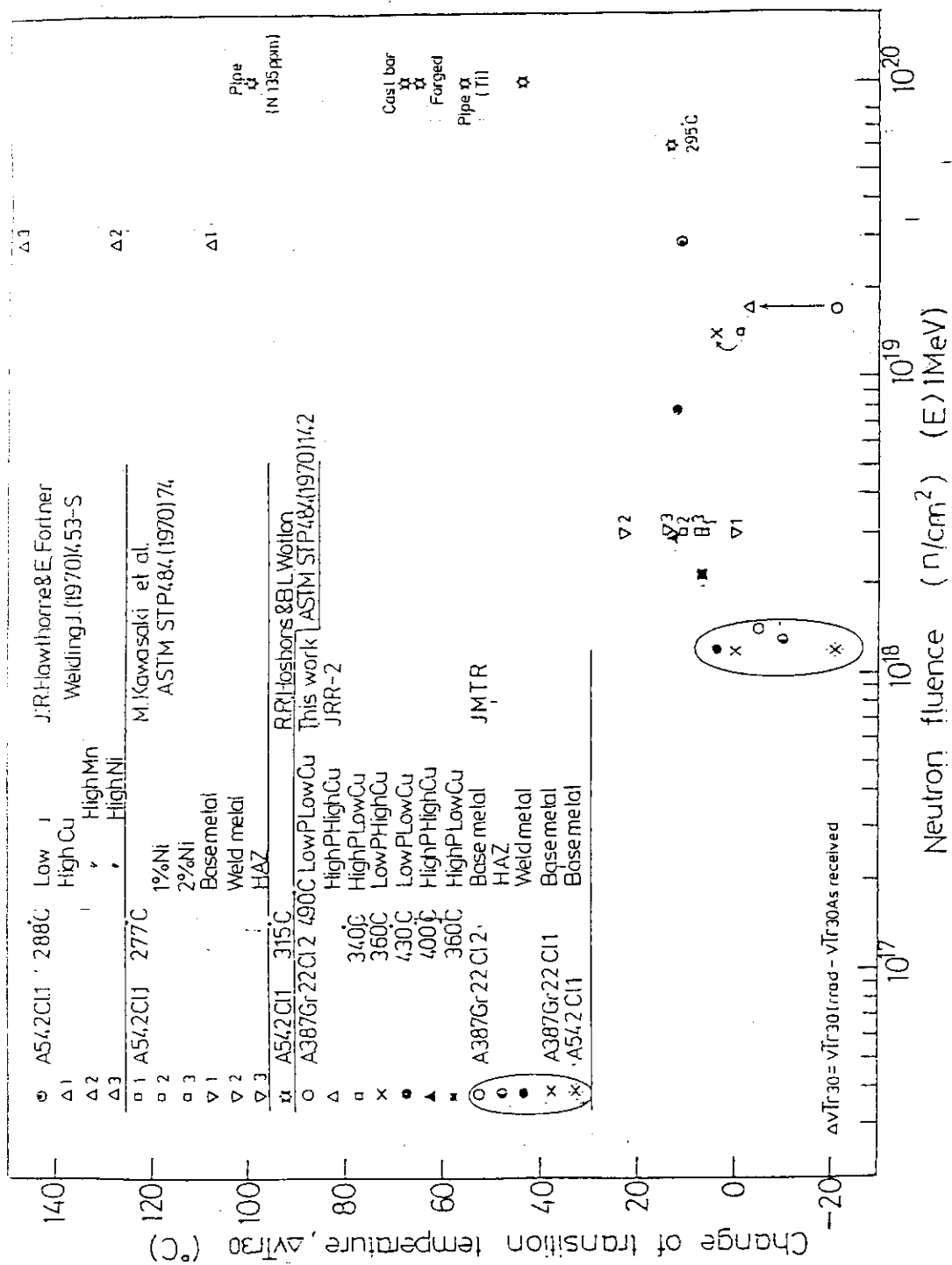3) Fatigue crack growth characteristics of irradiated steels and so on.

Fig.4.23   Neutron Irradiation Embrittlement of 2·1/4Cr—1Mo Steels

4.8　Embrittlement Caused by Stress Ageing Treatment

M. Suzuki, K. Fukaya and T. Oku

Introduction

A $2^1/_4$Cr-1Mo steel is expected to be used for a pressure vessel of VHTR. Temper brittleness, however, makes it brittle in the temperature range 375-550°C. Since the service temperature of the pressure vessel is expected to be around 400°C[1], we must take into consideration the embrittlement of the material caused by temper brittleness.
It is well known that segregation of impurity atoms to grain boundaries plays an important role in temper brittleness, and grain boundary strength is considered to be reduced accordingly. When material is used for structural component various kinds of surrounding factors may enhance embrittlement. We have already reported[2] that applied stress has an effect of enhancing embrittlement. (The treatment of ageing under applied stress was designated as stress ageing.)

In this experiment we have examined the degree of embrittlement caused by stress ageing to obtain the data which is applicable to the design and safety assessment of the reactor, particularly the data for much longer ageing time (3000 h) under comparatively low stress level (210 MPa) was obtained.

Experimental Procedure

Testing block with cross-sectional area of 60×12 mm^2 and gage length of 480 mm was prepared for stress ageing treatment and it was conducted with a 15 ton creep testing machine. The condition for the treatment was as follows: temperature: 450°C; stress: 210 MPa; ageing time: 3000 h. Chemical analysis for the used material is presented in Table. 4.3. The measure of the embrittlement employed here was the increase in the ductile-to-brittle transition temperature determined by Charpy impact tests. These Charpy specimens were machined from the block in the way illustrated in Fig. 4.24: one group of specimens were machined perpendicular to and the other group parallel to the direction of loading in order to examine the dependence of loading direction on the embrittlement. Tensile specimens were also machined in the same way to evaluate the tensile properties after stress ageing.

Results and Discussion

Absorbed energy transition curves for both stress–aged and isothermal–aged materials are shown in Fig. 4.25. There could be found two characteristic features for the type of the curves which clearly differ with treatments. Firstly, final rolling direction dependence on embrittlement is observed in isothermal–aged materials: the specimens machined parallel to the rolling direction (RW specimen) showed larger increase in transition temperature than those perpendicular to the direction (WR specimen). Secondly, there is loading direction dependence of the embrittlement in stress–aged materials. This effect can be observed by comparing the increase in transition temperature for stress–aged material with that for isothermal–aged material. That is, the increment caused by stress–ageing is almost the same as that by isothermal–ageing for WR specimen, while in the case of RW specimen stress–aged material showed larger increase than isothermal–aged material.

SEM (scanning electron microscopy) fractographic observation revealed that fraction of intergranular fracture increases as the transition temperature becomes larger. (This intergranular fracture surface probably corresponds to prior–austenite grain boundary.) On the other hand, as shown in Table 4.4, tensile property is independent on these treatments.

These experimental results indicate that increase in transition temperature after stress–ageing treatment was caused by reduction of grain boundary strength. The most important factor that affects the reduction of grain boundary strength is, as mentioned in the previous report[2], possibly intergranular segregation of phosphorus. Rolling direction and loading direction dependences of the embrittlement are considered to be related to the diffusion and segregation behavior of phosphorus atoms. The fact that embrittlement can be easily eliminated by heat treatment (575°C, 1 h) not only supports this interpretation but also gives useful information about the suppression of embrittlement for a practical use.

References

1) Aochi T., et al: "First Conceptural Design of the Experimental
   Multi-Purpose High-Temperature Gas-Cooled Reactor", JAERI-M 6845 (1977).
2) M. Suzuki et. al.: "Embrittlement of Normalized and Tempered
   $2^1/_4$Cr-1Mo Steel by the Temper Embrittlement under Stress" JAERI-M
   9150 (1980).

Table 4.3 Chemical Composition (wt %)

element specimen	P	Cu	C	Si	Mn	S	Ni	Cr	Mo	Al	As	Sn	Sb	Co	Ti	V	B
SPEC.	0.035 Max.	-	0.15 Max.	0.5 Max.	0.3 0.6	0.035 Max.	-	2.00 2.50	0.90 1.10	-	-	-	-	-	-	-	-
A	0.009	0.11	0.12	0.03	0.48	0.009	0.11	2.40	0.97	0.14	0.020	0.015	0.0030	0.012	0.005 Max.	0.01 Max.	0.0002 Max.
B	0.011	0.10	0.13	0.06	0.54	0.003	0.06	2.37	1.06	0.019	0.008	0.006	0.0028	0.012	0.005 Max.	-	-
C	0.005	0.10	0.13	0.04	0.53	0.004	0.09	2.32	1.17	0.006	0.0060	0.005	0.0026	0.019	0.005 Max.	-	-

Table 4.4 Results of tensile tests for 2¼Cr–1Mo steels heat A, embrittled by three embrittling treatments.

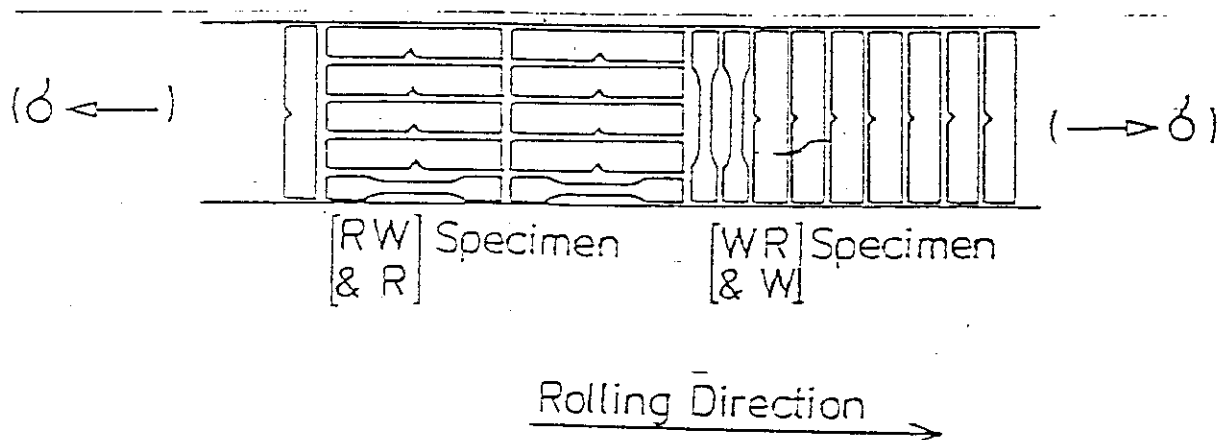| Embrittling treatments & specimen orientation		Yield stress (MPa)	U.T.S (MPa)	Elongation (%)	Reduction in area (%)	Vickers hardness No
As received	R	468	578	28.7	81.3	186.5±1.3
	V	479	582	30.2	81.0	183.8±1.8
450 °C, 3000h	R	442	561	29.5	81.0	179.6±2.7
	V	436	557	31.5	82.3	178.6±2.1
575 °C, 1h, de-embrittled	R	454	568	30.0	82.7	182.1±2.6
210 MPa, 450 °C, 3000h	R	484	596	30.8	81.4	182.7±2.4
	V	461	582	30.7	81.2	181.5±2.4
575 °C, 1h, de-embrittled	R	469	591	32.6	82.2	181.2±1.7
Step cooling	R	455	572	29.1	79.5	184.4±3.0
	V	450	566	29.5	81.1	183.9±3.0

Fig. 4.24 Charpy specimens and tensile specimens were cut from the materials in the way illustrated above. One which was paralell to the rolling direction was named RW (Charpy specimen) or R (tensile specimen) and perpendicular to the rolling direction was named WR or W respectively. Tensile stress axis was paralell to the rolling direction in the case of stress-ageing treatment.
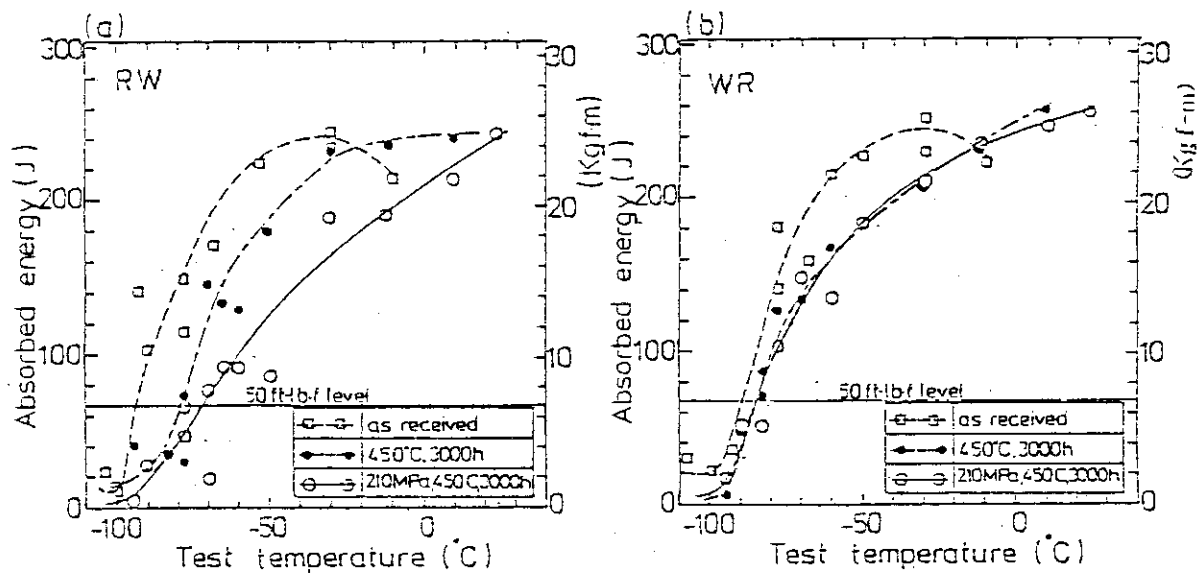

Fig. 4.25 Shifts in the absorbed energy transition curves due to embrittlement caused by isothermal-aging and stress-ageing treatment. (a),(b) each corresponds to the results for RW and WR Charpy specimens.

4.9 Low Cycle Fatigue Test

T. Kodaira, K. Fukaya, Y. Sato and T. Oku

Introduction

At the operation temperature of a VHTR pressure vessel, i.e. 400°C, it is necessary to evaluate sensitivity to temper embrittlement of $2^1/_4$Cr-1Mo steels. The temper embrittlement resulted from the segregation of phosphorus to the grain boundary and this phenomenon was accelerated by addition of stress. The present study was to clarify the effect of phosphorus on low cycle fatigue strength, i.e. the effect of dynamic stress on embrittlement.

Experimental Procedure

A 387 Grade 22 Class 2 steels with different amount of phosphours were tested. Tables 4.6 and 4.7 respectivly show the chemical composition and mechanical properties of tested materials. The low cycle fatigue test specimens are of a round bar type, as shown in Fig. 4.26, and are cut out parallel to the rolling direction. The low cycle fatigue test is conducted under the condition: deflection control, tension-compression, a strain rate of 10^{-3} sec^{-1} and triangle wave mode. This time tests were performed at room temperature, but the next is planned to be conducted at elevated temperatures.

Experimental Results

Figure 4.27 shows the relationship between total strain range and cycles to failure at room temperature. From this figure, it is clear that no appreciable difference of the low cycle fatigue strength is found among three tested steels with different amount of phosphorus. The fatigue design curve in Section III, Division 1 of ASME Code is also shown in the figure. It can be pointed out that the tested steels have a good low cycle fatigue property, judging from the comparison between the fatigue design curve and $1/2$ ε_t or $1/20$ N_f or the actural data, where ε_t and N_f respectively denote total strain range and cycle to failure.

Future Plan

The low cycle fatigue test of the steels mentioned above will be carried out at 450°C of the design temperature of the VHTR reactor vessel.

Table 4.5   Chemical Composition of Steels Tested

element	C	Si	Mn	P	S	Ni	Cr	Cu	Mo	Al	V	As	Sn	Sb	Co	B	Ti
spec. steels	0.15 max.	0.50 max.	0.30 ~0.60	0.035 max.	0.035 max.	—	2.00 ~2.50	—	0.90 ~1.10	—	—	—	—	—	—	—	—
BN 1	0.15	0.03	0.50	0.009	0.007	0.11	2.44	0.11	1.00	0,007	0.01 max.	0.019	0.016	0.0028	0.011	0.0002 max.	0.005 max.
BN 2	0.13	0.05	0.51	0.003	0.007	0.12	2.18	0.07	1.05	0.020	0.01 max.	—	—	—	—	—	—
BN 3	0.13	0.05	0.49	0.017	0.008	0.12	2.19	0.07	0.99	0.018	0.01 max.	—	—	—	—	—	—

Table 4.6   Mechanical Properties of Steels Tested

	0.2%YS (MPa)	UTS (MPa)	El (%)	RA (%)	H_V
spec.	310	517 ~690	22	45	
BN 1	431*	573*	25.4*	78.8*	185.8
	430.5	561	—	74.6	
BN 2	409.9	533.5	—	74.4	180.2
BN 3	419.7	539.4	—	72.8	181.8

0.2%YS:0.2% yield strength
UTS :ultimate tensile strength
El:elongation
RA:reduction of area
H_V : vickers hardness
*: mill sheet data

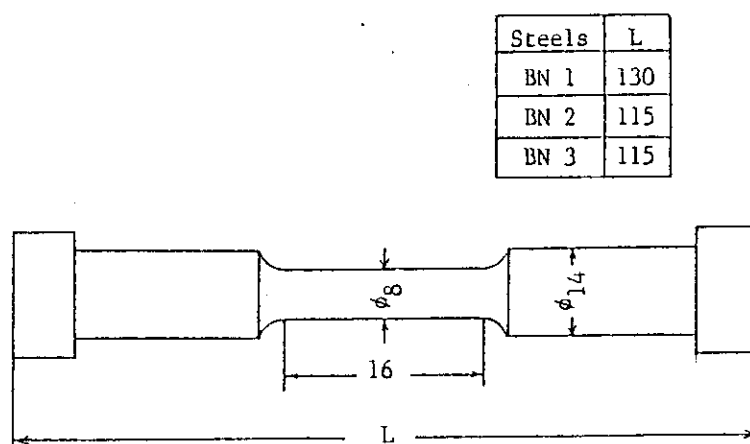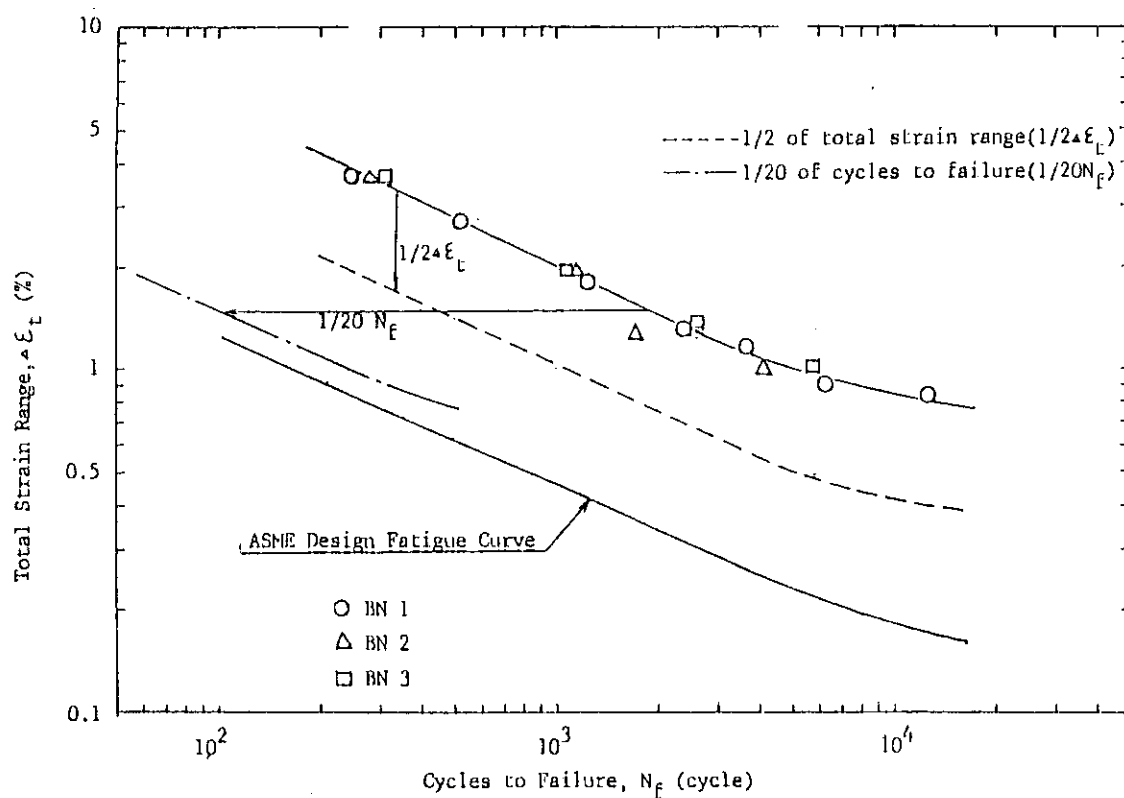| Steels	L
BN 1	130
BN 2	115
BN 3	115

Fig.4.26   Specimen Configuration

Fig.4.27   Low Cycle Fatigue Characteristics of 2·1/4Cr-1Mo Steels
at Room Temperature

4.10 Fracture Toughness Test

T. Kodaira, M. Matsumoto and K. Fukaya

Introdution

Collecting the fracture toughness data of irradiated and unirradiated steels is now required to evalute structural integrity of a VHTR pressure vessel. Consequently, fracture toughness tests with small specimens based on J-integral have been carried out to establish a surveillance test method.

Experimental Procedure

Three kinds of thick pressure vessel steels were used in this experiment. These are A 387 Grade 22 class 1, class 2 and A 542 class 1, and small three point bend specimens with the same dimension of a Charpy specimen ($10 \times 10 \times 56mm^2$) are taken perpendicularly to the rolling direction from the quarter thickness.

J_{IC} fracture toughness tests were conducted at several temperatures between -196°C and 200°C. The onset of crack initiation was detected by the d.c. electrical potential method, and J_i values were calculated by the following equation.

$$J_i = 2A/B \ (W-a)$$

where, A: area under load deflection curve up to onset of crack initiation

B: specimen thickness

W: specimen width

a: crack length

The critical K_i values ($K_i(J_i)$) are converted from J_i using the following formula.

$$K_i \ (J) = \sqrt{J_i E/(1-V)}$$

where, E: Young's Modulus

V: Poisson's ratio

Experimental Results

Figure 4.28 shows the results of fracture toughness test of three steels. The data of mill sheet are also shown in the figure, and these data are obtained by specimens with thickness of one inch. The result shows that the fracture toughness values are almost the same among three steels at the upper shelf region. On the other hand, A 387 Grade 22 class 1 steel has lower toughness than the other two at transition region. In Fig. 4.28, the comparisons are also made between the reference fracture

toughness, K_{IR}, in Appendix G of Section III of ASME Code and the measured values. From this figure it is seen that three tested steels have an excellent toughness, which is worthy to note.

Future Plan

The following experiments will be carried out to obtain the basic data for evaluation of structural integrity of the VHTR pressure vessel.

1) J_{IC} fracture toughness data of welded joints,
2) Dynamic fracture toughness (K_{Id}) data of base metals and welded joints,
3) Nil ductility transition temperature (NDT) data, and
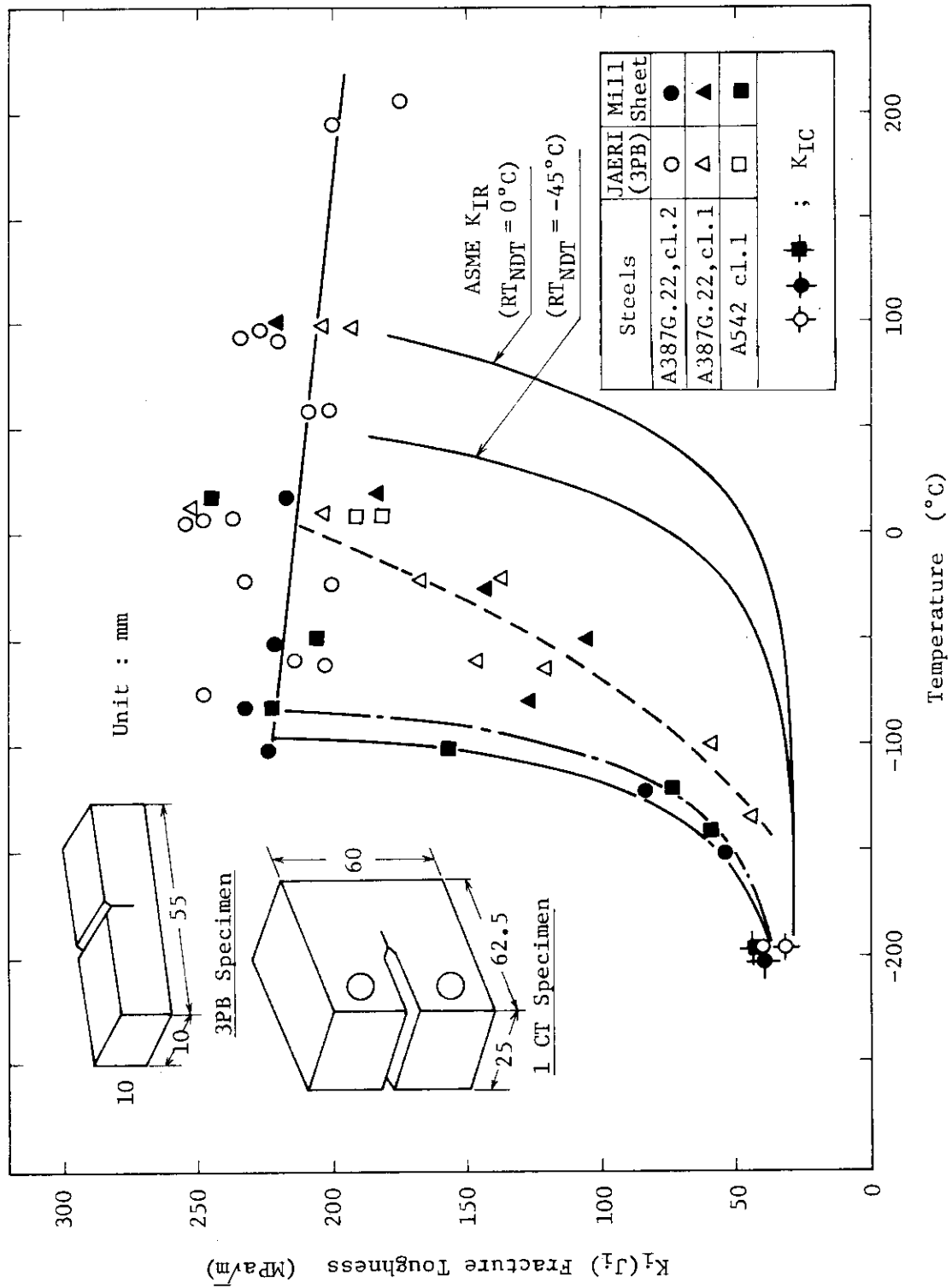4) Cycle crack growth rate data of base metals and welded joints.

Nomenclature

J_i : J value at the onset of ductile crack initiation
J_{IC} : J_i value in accordance with the valid specimen size requirements
$K_i(J_i)$: K value converted from J_i value
K_{IC} : Plane strain fracture toughness at linear elastic cleavage fracture

Fig. 4.28   Fracture toughness of $2\frac{1}{4}$Cr–1Mo steels.